ABSTRACT

Title of Dissertation: MODELING LASER PULSE EVOLUTION IN IONIZING GAS AND PLASMA WITH APPLICATION TO LASER WAKEFIELD ACCELERATION

James Hamilton Cooley, PhD. 2004

Dissertation Directed By: **Professor Thomas M. Antonsen, Jr., Department of Physics**

The interaction of high intensity laser pulses with matter is of current research interest not only for potential applications but also due to the interesting non-linear process that can occur with current experimental facilities. Understanding many of the non-linear processes requires significant modeling and simulation effort. We explore several aspects of laser pulse evolution and plasma response in simulations ranging from modeling laser wakefield accelerators to modeling basic ionization processes. First, we present a model that describes the onset and growth of axial modulation found experimentally during the formation of plasma channels formed using an axicon lens. We provide a systematic development that describes this new type of parametric instability and explains the pressure dependence and the mechanism for formation of these axial modulations in the channel. Next, we describe details of a new three-dimensional laser pulse evolution code that we have developed to model propagation in tenuous gas and plasma and we provide relevant information about the validation and testing of the code. We then use this new code

to examine the three-dimensional structure of the laser pulse evolving in the presence of ionizing gas. In particular we present results from the first three-dimensional study of the ionization scattering instability. Finally, we examine injecting electrons into laser wakefield accelerators. We examine in detail the injection and trapping characteristics for an electron beam with an initially broad energy distribution and look at the effect of beam loading on the trapping efficiency. We present estimates for the maximum charge that can be trapped from a low energy beam with a Boltzmann type energy distribution.

MODELING LASER PULSE EVOLUTION IN IONIZING GAS AND PLASMA WITH APPILCATION TO LASER WAKEFIELD ACCELERATION

By

James Hamilton Cooley

Dissertation submitted to the Faculty of the Graduate School of the
University of Maryland, College Park, in partial fulfillment
of the requirements for the degree of
Doctorate in Philosophy
2004

Advisory Committee:
Professor Thomas M. Antonsen, Jr., Chair
Professor Howard M. Milchberg
Professor James Drake
Dr. Parvez Guzdar
Professor Patrick O'Shea

Dedication

To my wife, Susan, and children, Rory, Taran, and Aidan, for their patience and support.

Acknowledgements

I am most grateful to my wife whose insistence that I go back to school and willingness to work full time while raising a family have made this effort possible.

I would like to acknowledge the help of the many researchers at the University of Maryland who seemed to always have an open door to discuss the many problems I encountered along the way. Without their willingness to guide my progress and their aid in solving these problems the road would be much longer and more difficult.

In particular my thanks goes to Prof. Antonsen who was always available and willing to discuss the most trivial problem with patience and understanding. Additionally, I appreciate Prof. Bill Dorland's help in the high-end computational effort and also his support as my advisor for my masters in Applied Math and Scientific Computing. Access to Prof. Milchberg and his laboratory were invaluable in gaining a physical understanding of the physics I was studying and in preventing me from becoming simply a numericist, for this I am grateful. I would also like to thanks Dr. Guzdar for his availability for my frequent questions on basic numerical techniques and in particular his aid in developing the code used in the second chapter of this book. Lastly, I am grateful to the researchers at the Naval Research Laboratories who guided me into the research presented in chapter five and also provided a stimulating environment for me to learn and work over the last year.

Finally, I would like to thank the US Department of Energy for the financial support I have received from them over the five years of my study.

Table of Contents

Chapter 1: Introduction

Background

Researchers have been interested in the application of high-power laser systems to various areas of plasma physics and non-linear optics for several decades [1-5]. Recent advances in pulse amplification and compression, specifically use of chirped pulse amplification (CPA) for laser pulses[6,7], have made high-power laser systems available for a wide range of applications. Current laser systems can achieve laser intensities in excess of 10^{19} W/cm^2, with peak laser pulse power in excess of 10×10^{12} W, 10 terra-watts (TW). This increase in availability has led to numerous theoretical and experimental investigations into the effects of high-intensity and of high-power laser pulses on matter. Applications for these high-power laser systems include laser wakefield accelerators (LWFA)[1,8-11], x-ray generation[3,12], harmonic generation[13] and spectral broadening[14].

In LWFA, a high-power laser pulse propagates through uniform plasma. The laser electric field expels the electrons due to the ponderomotive force. (The ponderomotive force will be discussed in the body of this thesis. Briefly, it is the average Lorenz force on an electron oscillating in a time-varying laser field and it is proportional to the gradient of the laser intensity.) The ions in the plasma remain stationary on the time scale of the laser pulse, ~100 fs, due to their large inertia. This process creates a charge separation resulting in an electro-static restoring force. This in turn gives rise to a plasma wave just behind the laser pulse. This plasma wave travels at the group velocity of the laser pulse and provides an electric field suitable for accelerating electrons.

For a resonant LWFA[1] to be effective the laser pulse intensity must be near 10^{18} W/cm^2 since the laser must drive a plasma wave with sufficient amplitude to accelerate electrons. The optimum laser pulse duration is determined by the plasma frequency such that $\tau_{laser}\omega_p \approx \pi$, where τ_{laser} is the laser pulse duration, $\omega_p^2 = 4\pi q^2 n_e / m_e$ is the normal plasma frequency and q, n_e and m_e are the charge, density and mass of the electrons respectively. For LWFA to be effective, extended interaction distances of the laser pulse with the plasma must exist since the laser pulse must propagate with little distortion for several centimeters to provide an accelerating field over a distance long enough to impart significant energy to the electrons. For a laser pulse propagating in vacuum the interaction length is limited to the Rayleigh length $Z_r = \pi r_0^2 / \lambda$, where r_0 represents the laser spot size at vacuum focus and λ is the laser wavelength. However, for reasonable spot sizes, $r_0 \sim 10 - 20\mu m$, the Rayleigh length is too short to accelerate particles to high energy. Thus, a means at overcoming diffraction must be found. Diffraction can be overcome by use of plasma channels[2,15-17], which are shaped plasma structures that have a local minimum electron density on the laser optical axis. This local density minimum will tend to focus the laser pulse on axis and thus guide the laser pulse, much as a dielectric fiber. Non-linear affects in ionized plasma may disrupt the pulse profile[18-20] and must be understood and suppressed.

When a laser pulse propagates in plasma, the oscillating laser pulse electric field forces each free electron to jitter along the laser electric field polarization direction. If the jitter velocity is high enough, this motion results in a change to the effective mass of each electron due to the relativistic Lorentz factor[21-24]. The

modification to the plasma dielectric response is

$\delta\varepsilon = -\left(k_p^2 / k_0^2\right) / \sqrt{1 + \left(q^2 |\mathbf{E}|^2 / 2m^2\omega^4\right)}$, where q and m are the charge and mass of an electron, k_0 is the laser wavenumber, $k_p = \omega_p / c$, and **E** is the laser electric field envelope.

Non-linear modifications of $\delta\varepsilon$ can lead to interesting processes. For instance, laser pulse self-focusing[23,24] occurs due to the laser electric field modification to the material dielectric response. The non-linear response of the material is proportional to the local laser intensity and the material dielectric response has a local maximum at the location of the peak laser pulse electric field. The phase fronts of the laser pulse will curve toward regions of higher dielectric. Therefore, the phase front will tend to curve toward the axis of the laser, where the intensity is highest. If the effect of the self-focusing on the laser pulse is larger then the pulse diffraction, the laser pulse will tend to focus on the optical axis[23,24]. This self-focusing can be characterized by a critical power given by $P_{cr}=2c(mc^2/q)^2(\omega/\omega_p)^2$ or approximately $P_{cr}=17.4(\lambda_p/\lambda)^2$[24].

Additional non-linear phenomena are present in Neutral gas. For instance, neutral gas atoms can be polarized due to the laser pulse. This polarization is dependent on the local laser intensity through both electronic polarizability (Kerr) [25] and rotational Raman polarizability [25] . Thus, the dielectric response of the material is related to the time evolution of the local laser intensity by the convolution, $\delta\varepsilon = 2n_2 \otimes I$, where $I = (c / 2\pi)|\mathbf{E}|^2$, and n_2 is a function that characterizes the second order material response to the laser pulse. This response contributes a term

that is non-linear, third-order in the laser field **E**. For the simplest model, presented in the following chapters, the material response will be considered instantaneous and the convolution reduces to simple multiplication by a material dependent coefficient n_2. This approximation accounts for the Kerr non-linear response but neglects rotational Raman effects. Again, we see the dielectric response is proportional to the local laser intensity and thus self-focusing may occur. In this case, the self-focusing is characterized by a critical power for self-focusing, which for a gaussian pulse is given by $P_{cr} = \lambda^2 / 2\pi n_0 n_2$ [26], where n_0 is the linear index of refraction.

Self-focusing in either neutral gas or plasma is unstable to transverse perturbations of the laser pulse. Therefore, the laser will undergo transverse filamentation if the relevant laser pulse power is much greater then the critical power for self-focusing. We will examine self-focusing and filamentation in the body of this thesis.

The interaction of high power laser pulses with neutral gas can also lead to ionization. The laser pulse will ionize the neutral gas predominately in regions of maximum electric field (along the optical axis) and eliminate the neutral gas in this region. This ionized gas produces plasma which, at powers below P_{cr} for a plasma discussed above, will contribute a term to the dielectric function that refractively defocuses the laser pulse, $\delta\varepsilon \simeq -k_p^2 / k_0^2$. The atomic polarization in neutral gas, responsible for self-focusing, will not be present in regions of high ionization. However, neutral gas persists outside the plasma region and the pulse will experience self-focusing in the outer regions. The net result of these competing effects is the laser pulse will be confined to a cylinder surrounding the plasma; that is, it is guided

off the optical axis guiding[27]. Off-axis guiding occurs due to a competition between refraction due to the plasma and self-focusing affects due to the neutral gas.

If the material through which a high-power laser pulse propagates is not uniform, additional processes can occur. For example, gases with a high cluster density can absorb the laser energy efficiently and have been used to generate x-rays [3,12] or high harmonics of the laser pulse[30-32]. These cluster gases are produced by Van der Waals interaction in a cooled gas as it expands into a vacuum. The ionization process can also result in an instability caused by the scattering of the laser pulse by small amplitude transverse density perturbations[28] in the free-electron density. Details of this process will be discussed in Chapter 4.

Coupling of the laser pulse to perturbations in the plasma density can lead to unstable growth of scattered waves, (i.e. Raman (electron) or Brillion (ion) scattering [18,24,33]). The growth of waves due to the scattering of the laser pulse from density perturbations is broadly known as parametric instability [33] and has been studied extensively[24,28,33-35]. This work presents a new type of parametric instability in the formation of plasma channels that results from a coupling between the incident laser pulse and a scattered wave that is a quasi-guided mode in the evolving channel. This coupling leads to growth of the density perturbations responsible for the initial scattered wave, and thus an increase in the scattered wave.

Purpose of Dissertation

This thesis presents a systematic analysis of three distinct physical phenomena that result from the interaction of high-intensity laser pulses with matter. These phenomena are 1) the modulation instability during the formation of plasma wave

guides, 2) non-linear pulse evolution in the presence of ionizing gas, and 3) trapping and acceleration of electrons in a resonant laser wakefield accelerator. First we examine the formation of a plasma channel.

One method to create a plasma channel is to use an axicon lens to focus a laser pulse [2,15,16,36]. This laser pulse produces a line focus into a gas and will lead to ionization of the gas. This plasma will expand due to thermal pressure and result in plasma with a minimum density on the optical axis. Such a plasma channel has potential application for guiding high intensity laser pulses over many Rayleigh lengths. However, the laser pulse duration used for channel formation is typically long compared to the plasma evolution time and thus the plasma channel can modify the formation pulse. Thus new and interesting phenomena can appear due to the coupling of the laser pulse to the evolving channel. For instance, at low gas pressures the plasma channel is axially uniform[16,36] but as the pressure of the background gas is increased there is an increase in the energy absorbed from the laser pulse. This increased absorption is understood in terms of the coupling of the laser pulse to a resonant mode of the evolving channel. As the plasma channel evolves for some pressures there will be a specific time when the incident laser pulse is resonant with the plasma channel. During this interval the plasma will absorb the laser energy more efficiently due to increased plasma heating[37,38]. However, as the gas pressure is increased further, axial modulations appear with a periodicity that is strongly dependent on the initial gas pressure.

In this thesis we present a model that explains the growth of modulations during channel formation. This model treats the axial modulations as linear

perturbations of an axially smooth plasma channel. These perturbations are shown to grow exponentially during the channel evolution and account for the formation of the axial modulations seen experimentally as well as accounting for their strong pressure dependence. An analytic assessment for the growth rate of this instability is presented as well as numerical calculations for the growth rate and scattered wavenumber. This analysis shows that at high pressure the instability is dominated by the ionization process of the gas at the outer edge of the plasma channel.

The next phenomenon we will present in this thesis involves the three-dimensional evolution of a laser pulse. Investigation of this phenomenon requires development of a new code. This code provides fully three-dimensional simulations of laser pulse evolution on massively parallel computers. The model equations for the laser pulse envelope are presented in Chapter 3. Details of the numerical implementation of this model as well as efforts performed to validate and benchmark this code are also presented.

The first application of this new code is to study the three-dimensional nature of laser pulse propagation in ionizing gas. We present results of simulations for laser pulse propagation in ionizing gas and in particular, we study the ionization scattering instability[28], which is due to a coupling between a laser pulse and small amplitude scattered waves. The laser pulse and scattered wave electric fields couple through the ionization rate $\nu\left(\left|\mathbf{E}_{laser}+\mathbf{E}_{scattered}\right|\right)$ which depends strongly on the local value of |**E**|. The model we use for the ionization process includes both multi-photon and tunneling ionization. The coupling of the laser pulse and the scattered waves can lead to transverse modulations in the resulting plasma density and thus further scatter the

laser pulse. The results provided here are the first three-dimensional simulations of this instability.

The focus of our investigation of the ionization scattering instability is two-fold. First, we examine the dependence of the growth of the scattered waves on transverse wavenumber. This transverse dependence in growth rate results in the filamentation of the laser pulse. These simulations show that the growth rate is small for low values of transverse wavenumber, as predicted by local analysis of the instability [28]. We also confirm that the instability is convective in the laser frame, consistent with previous results. We identify broken symmetry in the formation of the laser filaments and show that this symmetry breaking, that is only seen in three-dimensions, may provide better insight into experimental results[82]. Next, we examine the frequency shift of the scattered modes. We confirm that these scattered modes are blue shifted relative to the laser and we find agreement with results from both analytic and two-dimensional simulations [28]. This instability may lead to difficulties in diagnosing experiments with ionizing gases due to the plasma filamentation that affects not only the primary laser pulse but also any following probe pulse.

The final part of this thesis focuses on the injection of electrons into a resonant LWFA[1]. In particular we emphasize injection of electron bunches that have an initially low energy with a broad energy spread. This electron distribution is typical of many optical injection schemes that involve using a high-intensity laser to either ionize gas[80] or interact with a solid (e.g., wire target)[81] to produce electrons for use in a LWFA. We perform an analysis using a one-dimensional

Hamiltonian[72]. This Hamiltonian analysis is adjusted to include two-dimensional effects, due to de-focusing, by restricting the operating phase-space. We use this analysis to demonstrate that it is possible to trap a significant number of electrons and achieve significant energy gain while delivering a relatively small energy spread in the final bunch.

We have performed two-dimensional simulations using the code WAKE[39] using test particles to simulate the trapping and acceleration process. We show that the actual minimum energy needed for electron trapping in a plasma channel is lower then assumed for the Hamiltonian analysis, consistent with previous work[40]. We then investigate perform an analysis using the Hamiltonian theory with a modification to the wake field phase, consistent with the simulation results, and show that non-ideal electron bunches may be adequate for some LWFA applications.

Finally, we study the effect beam loading has for injecting electrons that have an initially low energy and a large energy spread are emphasized. We show that the effect of the large charge in the initial beam can disrupt the trapping and accelerating process and lead to a maximum acceptable charge that can be trapped.

Outline of Dissertation

The remainder of this thesis is outlined below. In chapter 2 we discuss the formation and application of plasma channels and we derive the model equations that give rise to the modulation instability in the formation of plasma channels. Detailed analytic calculations that show the relevant scales for the onset of this instability follow. Chapter 2 concludes with a presentation of numerical calculations that help

confirm the model and demonstrate good agreement with the experimental results both in the onset of this instability and in the axial modulation period.

In chapter 3 we present details of the code developed to examine three-dimensional effects in laser pulse propagation, beginning with a presentation of the relevant equations for the laser pulse and schemes to numerically solve this equations. We also present details of our efforts to benchmark and validate the code. Finally, we present one model for the plasma response given by a kinetic description of the plasma electrons solved using a particle-in-cell technique and provide results for the validation of this plasma response.

In chapter 4 we will present details of the application of this new code to laser pulse evolution in ionizing gas and in particular of the three-dimensional structure for the ionization scattering instability[28]. We begin by presenting comparisons with previous work [27] to examine laser pulse phenomena in different ranges of laser peak-power. We then examine the evolution of an initially planar pulse with intensities between $1x10^{15}$ and $2x10^{16}$ W/cm^2 in gas with pressures between a few torr and several hundred torr He to examine the ionization scattering instability[28]. The effect of this instability on the propagation of a gaussian pulse into a gas jet target will then be presented.

Finally, we will examine injection of electrons into a LWFA in chapter 5. We will present results of a Hamiltonian analysis and two-dimensional test-particle simulations for the case of initially low energy electron bunches with a broad energy spread. Then we will present results for an electron bunch with self-consistent fields

being injected into a guided LWFA. Finally, in chapter 6 we will provide conclusions and potential directions for future effort.

Chapter 2: Parametric Instability in the Formation of Plasma Waveguides

Introduction

Plasma waveguides for guiding intense laser pulses have applications in particle accelerators and x-ray generation schemes [43,44]. Waveguides can be formed using a variety of methods [45-48]. One method is to create a plasma channel by ionizing a gas with a moderate intensity laser pulse focused through an axicon. The axicon focuses the laser pulse to a line where gas is ionized and expands, creating a shock, and leaves an electron density profile with an off-axis maximum that defines the channel. Ideally, the plasma channel will be axially symmetric and allow for guiding of high intensity light over distances of many Rayleigh lengths, $Z_r = \pi w^2 / \lambda$, where w is the vacuum focal spot size and λ is the laser wavelength. Axially symmetric channels have been produced using axicon focusing of ~100 ps laser pulses in low-pressure gas, and their evolution is well understood [36,49,50]. However, as the gas pressure is raised, the plasma channel affects the propagation of the axicon pulse and new and interesting phenomena occur. For example, at specific values of initial gas pressure the axicon field couples strongly to guided modes in the resulting plasma channel and linear resonant absorption occurs [50]. This linear absorption still yields axially smooth channels. As pressure is increased further, axial modulations with definite periodicity begin to appear on a time scale comparable to the ~100 ps laser pulse. This is distinct from previous observations [51-53] of axial modulations at even higher pressures and at pulse durations significantly longer than a typical channel expansion timescale [45] of $w/c_s \sim 1$ ns, where w is the laser spot

size and c_s is the plasma sound speed. In those experiments, modulations appear due to interference between the incoming and outgoing rays of the heating pulse. In this chapter we present the first evidence of axial modulations that occur at intermediate pressures and on much faster timescales and argue that these modulations result from a distinct form of nonlinear resonant absorption that has the character of a parametric instability. Further, we present a model of this instability and describe the growth of the unstable perturbations.

In the experiment, a 100ps (FWHM) laser pulse of wavelength 1.064 μm was focused through an axicon lens into uniform ambient argon gas of variable pressure, with a peak vacuum intensity of 5×10^{13} W/cm^2. Axicons with base angles from 10° to 30° were used. However, the axial modulation results varied weakly with the axicon angle, and the results presented below are for the 25° base angle axicon. A delayed probe pulse, split from the main pulse, is incident perpendicular to the axis of the evolving channel and imaged into a Charge Coupled Device (CCD) camera. The probe pulse can be imaged directly into the camera generating a shadowgram, or it can be passed through a glass wedge generating an interferogram. When the channel is azimuthally symmetric the interferograms have been used to deduce time evolving radial profiles of electron density [36,49]. These profiles compare well with those predicted from a one-dimensional hydrodynamic code [50] that we will use in this work.

Figure 1 shows a set of shadowgrams taken for a series of background pressures of argon: a) 200 Torr, b) 280 Torr, c) 300 Torr, d) 340 Torr, e) 370 Torr, and f) 420 Torr taken at a pump-probe delay of 330 ps. The figure shows a 0.8 mm

axial section of the channels. The total length of the channel is about 15 mm. The channel is seen to be relatively axially uniform on the scale of the image for pressures 300 Torr and less. This is not the case for the channels formed in higher pressure, 340 Torr and greater. Here a distinct axial modulation of the channel is evident. The density variations in the highest-pressure case are of the order of 10% based on interferograms. The wavelength of the modulation, calculated by Fourier transforming the image intensity along the axis of the channel and finding the wavenumber peaks, is approximately .14 mm and .09 mm in the 340 and 370 Torr case respectively. Note that there is a relatively large change in wavelength that accompanies a relatively small increase in pressure. Our model of the modulations explains this observation.

According to our explanation, the modulations are the result of a nonlinear absorption process that involves a coupling between the incident axicon field, a guided mode of the channel, and the axial modulations of the channel parameters. Specifically, the axicon focuses the formation pulse rays at an angle θ to the axis of the axicon, which we take to be the z-axis ($\cos\theta = 0.967$ in the experiment). Thus, the axicon field has an axial wavenumber $k_a = k_0\sqrt{1+4\pi\chi}\cos\theta$, where $k_0 = \omega_0 / c$ is the laser vacuum wave number, and χ is the susceptibility of the gas. The axicon creates a plasma channel that after time can support guided modes with axial wavenumber k_g, which is a function of the channel density profile as well as the azimuthal and radial mode indices of the mode in question [49]. Linear resonance absorption [50] occurs when the axicon and guided mode wavenumbers match, $k_a = k_g$. In this case the axicon field can tunnel through the wall of the channel and excite

a quasi-guided mode. This occurs at specific values of initial gas density and time for a given mode. Nonlinear absorption occurs as the result of a parametric instability. If there is a small axial modulation of the channel parameters with wavenumber $k_m = k_g - k_a \neq 0$, then the axicon field will be scattered into the guided mode. The local heating rate in the channel, which is proportional to the laser intensity, will then have an axial modulation at k_m due to the beating of the axicon field and the guided mode. This modulated heating rate will reinforce the initially small modulation of channel parameters and result in exponential growth of the channel modulations and increased absorption of the axicon field. The insensitivity of the modulation wavenumber to axicon base angle follows from the fact that for small angles $\cos\theta \approx 1$.The organization of the remainder of this chapter is as follows. In Sec. II we develop a linear theory for the formation of modulations in an expanding channel based on fluid equations. This leads to an eigenvalue equation for the growth rate of perturbations with a specified axial wavenumber. We then give an approximate analytical solution to this eigenvalue problem in the case in which the channel is deep. We also discuss the space-time evolution of perturbations and show that the instability is absolute in the lab frame. In Sec. III we present numerical solutions for the growth rate of the modulations based on channel profiles that are predicted by the hydro-code. We then integrate the growth rate over time during the formation of a channel to arrive at a value of the cumulative growth of the instability as a function of modulation wavenumber. We then compare this prediction with the images in fig. 1. In Sec IV we discuss and summarize our results.

Linear theory of modulation growth

To lend support to our picture of the development of modulations we investigate the linear stability of the formation of an axially symmetric channel to perturbations with axial modulations. In our model, the electric field consists of a symmetric axicon pulse $\boldsymbol{E}_a$ and a small, scattered wave, $\tilde{\boldsymbol{E}}_s$,

$$\boldsymbol{E}(r,t) = \mathrm{Re}\{\boldsymbol{E}_a(r)\exp[i(k_a z - \omega_0 t)] + \tilde{\boldsymbol{E}}_s(r,z,t)\exp[i(k_s z + m\theta - \omega_0 t)]\}. \qquad (1)$$

Similarly, the electron density is written as the sum of a symmetric part and a small perturbation with modulations,

$$n_e(\boldsymbol{r},t) = n_0(r) + \mathrm{Re}\{\tilde{n}(r,t)\exp(ik_m z + im\theta)\}, \qquad (2)$$

where k_m=k_s-k_a. The axicon field amplitude, which we assume to be linearly polarized, satisfies a radial differential equation of the form,

$$(\nabla_\perp^2 + \kappa^2(r,\omega_0,k_a))E_a(r) = 0, \qquad (3)$$

where $\kappa^2 = k_0^2(1+4\pi\chi) - k_a^2 - 4\pi r_e n_0(r)(1+i\nu/\omega_0)^{-1}$ [50], ν is the electron-ion collision rate and r_e is the classical electron radius. The amplitude of the incoming axicon wave at $r \to \infty$ is specified. The electron density profile, $n_0(r)$, is determined self-consistently along with the amplitude of the axicon field, $\boldsymbol{E}_a$, by the previously mentioned one-dimensional hydrodynamic code [50] that includes the relevant

formation processes such as ionization, joule heating, and thermal conduction. The beating of the axicon field and the density modulations drives the scattered wave,

$$\left[\nabla_{\perp}^{2} + 2i\frac{\omega_0}{c^2}\frac{\partial}{\partial t} + \kappa^2(r,\omega_0,k_s)\right]\tilde{E}_s(r,t) = 4\pi r_e \tilde{n}_e(r,t)E_a\,, \tag{4}$$

where the scattered wave is polarized in the same direction as the axicon field.

The density perturbation is determined by the linearized equations of continuity, momentum balance, and energy balance,

$$\frac{\partial}{\partial t}\tilde{n} + \nabla\cdot\tilde{\mathbf{v}}n_0(r) = 2n_0\tilde{n}S(T_e) + n_0^2\tilde{T}_e\frac{\partial S}{\partial T_e} + n_0\left(\tilde{n}_s T_a^* + n_a^*\tilde{T}_s\right)\frac{\partial S}{\partial T_e}, \tag{5a}$$

$$m_i\, n_0(r)\frac{\partial}{\partial t}\tilde{\mathbf{v}}(r,t) = -\nabla_{\perp}\tilde{p} - \frac{1}{2}\frac{n_0 e^2}{m_e c^2}\nabla_{\perp}(\tilde{E}_s(r,t)E_a^*)\,, \tag{5b}$$

$$\frac{3}{2}\frac{\partial}{\partial t}\tilde{p} = \frac{n_0 e^2}{m_e}\frac{\nu}{\nu^2+\omega_0^2}\tilde{E}_s(r,t)E_a^*\,. \tag{5c}$$

Here we have neglected convective terms on the left hand side of the fluid equations under the simplifying assumption that the growth time is less than the channel evolution time. By the same reasoning, we neglect perturbations in the heating rate due to perturbations in density and temperature. The terms on the right hand side of Eq. (5a) represents the linearization of the collisional ionization rate, $n^2\, S(T_e)$ where $S = \sum_i S_i(T_e)\, n_i\, / n$ and $nn_i S_i(T_e)$ is the rate of collisional ionization of the i$^{\text{th}}$ ionized stage of the working gas and $S_i(T_e)$ is given by

$S_i(T_e) = 9\times10^{-6}\sqrt{T_e/U_i}\exp(-U_i/T_e)/U_i^{3/2}(T_e/U_i + 4.88)$[54], where U_i is the ionization potential for the i$^{\text{th}}$ electron, in eV. The first two terms represent

modifications to the ionization rate due to low frequency perturbations in electron density and temperature. In the linearization of these terms we have assumed for simplicity that the ratios n_i / n remain fixed for low frequency perturbations. This eliminates the need to follow the perturbations in the individual ionization stage densities. The last term represents the modification of the ionization rate due to the beating of high frequency perturbation of the electron density and temperature. These perturbations arise if the electron quiver motion in the axicon field and the scattered field carries the electrons across temperature and density gradients. Specifically,

$$\frac{\tilde{n}_{a,s}}{n_0} = \frac{q\tilde{\boldsymbol{E}}_{a,s} \cdot \nabla n_0}{\omega(\omega + i\nu)mn_0},$$

and

$$\frac{\tilde{T}_{a,s}}{T_0} = \frac{q\tilde{\boldsymbol{E}}_{a,s} \cdot \nabla T_0}{\omega(\omega + i\nu)mT_0}.$$

Finally, we have neglected motion in the z-direction under the assumption that the channel radius is much less than the axial wavelength of the modulations. This is well satisfied for pressures below 370 Torr, but marginally satisfied at higher pressures.

On the right hand side of Eqs. (5a)-(5c) we have three nonlinear terms allowing coupling of the scattered mode field to the density perturbation in the presence of the axicon field. These are the nonlinearly modified ionization rate in Eq. (5a), the ponderomotive force in Eq. (5b), and the Joule heating rate in (5c).

We assume perturbations grow exponentially in time with a complex growth rate γ. Thus, each of the perturbed quantities in Eqs. (5) is expressed in terms of a complex amplitude and a time dependent exponential factor, viz. $\tilde{n} = \hat{n}\exp[\gamma t]$. We also assume the pressure satisfies the ideal gas law, $\hat{p} = n_0\hat{T} + \hat{n}T_0$. With these assumptions we can combine Eqs. (5) to obtain an expression for the complex amplitude of the density modulation,

$$\frac{\hat{n}}{n_0} = \frac{c^2}{\omega_p^2\Delta}\left[\nabla_\perp^2\left(\frac{\gamma_0^3}{\gamma^3}u_s u_a^*\right) + \nabla_\perp\cdot\left(\frac{\gamma_p^2}{\gamma^2}\nabla_\perp u_s u_a^*\right) + \frac{\omega_p^2}{c^2}\left(\frac{\gamma_I^2}{\gamma^2} + \frac{\gamma_s}{\gamma}\right)u_s u_a^*\right], \tag{6}$$

where we have introduced the following notation. The quantity Δ in the denominator of (6) is given by

$$\Delta = 1 + \frac{\nu_I(\eta - 2)}{\gamma}, \tag{7}$$

where $\nu_I = n_0 S$ is the radially varying ionization rate, and $\eta = d\ln S / d\ln T_e$. Other quantities in Eq. (6) are the growth rates

$$\gamma_0^3 = (2/3)k_p^2(m_e/m_i)\nu V_{osc}^2,$$

$$\gamma_p^2 = \gamma_0^3/(3\nu),$$

$$\gamma_I^2 = (2/3)\nu_I\eta(m_e/T_e)\nu V_{osc}^2,$$

and

$$\gamma_s = \nu_I\eta V_{osc}^2/(\omega^2 r_n r_T),$$

where $V_{osc}^2 = (e/m_e)^2 |E_{a0}|^2 / (\omega_0^2 + \nu^2)$ is the oscillation velocity based on the axicon field amplitude E_{a0} and $u_a(r) = E_a(r)/E_{a0}$ and $u_S(r) = E_S(r)/E_{a0}$ are the normalized axicon and scattered field profiles and $r_{n,T}^{-1} = d\log(n,T)/dr$ are the inverse scale length for density or temperature. Terms involving γ_0 originate from the nonlinear perturbation of the heating rate in (5c). Terms involving γ_p originate from the ponderomotive force in (5b), and terms involving ν_I, γ_I, or γ_s originate from the perturbations of the ionization rate in (5a).

Equations (4) and (6) can be combined into an eigenvalue equation for the scattered field profile and growth rate,

$$\left[\nabla_\perp^2 + 2i\frac{\omega_0}{c^2}\gamma + \kappa^2(r,\omega_0,k_s)\right] u_s =$$

$$\frac{u_a}{\Delta}\left[\nabla_\perp^2\left(\frac{\gamma_0^3}{\gamma^3}u_s u_a^*\right) + \nabla_\perp\cdot\left(\frac{\gamma_p^2}{\gamma^2}\nabla_\perp u_s u_a^*\right) + \frac{\omega_p^2}{c^2}\left(\frac{\gamma_I^2}{\gamma^2} + \frac{\gamma_s}{\gamma}\right)u_s u_a^*\right] \qquad (8)$$

This equation can in turn be put in the form of a second order ordinary differential equation for the radial profile $\hat{u}_s(r)$, where $u_s(\mathbf{r}) = \hat{u}_s(r)\exp(im\theta)$,

$$M(r)\frac{d^2}{dr^2}\hat{u}_s + N(r)\frac{d}{rdr}\hat{u}_s + Q(r)\hat{u}_s = 0. \qquad (9)$$

The coefficients in (9) are defined as,

$$M(r) = 1 + \nu_I \frac{\eta - 2}{\gamma} - \frac{\omega_0 |u_a(r)|^2}{2(\omega_0 + i\nu)} \left[\frac{\gamma_0^3}{\gamma^3} + \frac{\gamma_p^2}{\gamma^2} \right], \tag{10a}$$

$$N(r) = 1 + \nu_I \frac{\eta - 2}{\gamma} - \frac{\omega_0 u_a}{2(\omega_0 + i\nu)} \left[\frac{rd}{dr}\left(\frac{\gamma_0^3}{\gamma^3} u_a^* \right) + \frac{d}{dr}\left(\frac{r\gamma_0^3}{\gamma^3} u_a^* \right) + \frac{d}{dr}\left(\frac{r\gamma_p^2}{\gamma^2} u_a^* \right) + \frac{r\gamma_p^2}{\gamma^2} \frac{d}{dr} u_a^* \right], \tag{10b}$$

and

$$Q(r) = \left(1 + \nu_I \frac{2 - \eta}{\gamma} \right) \left(\kappa^2 - \frac{m^2}{r^2} \right) + \frac{\omega_0 |u_a|^2}{2(\omega_0 + i\nu)} \frac{\omega_p^2}{c^2} \frac{\gamma_I^2}{\gamma^2}$$

$$- \frac{\omega_0 u_a}{2(\omega_0 + i\nu)} \left[\frac{d}{rdr} \frac{rd}{dr}\left(\frac{\gamma_0^3}{\gamma^3} u_a^* \right) - \frac{m^2}{r^2}\left(\frac{\gamma_0^3}{\gamma^3} u_a^* \right) + \frac{d}{rdr}\left(r \frac{\gamma_p^2}{\gamma^2} \frac{d}{dr} u_a^* \right) - \frac{m^2}{r^2}\left(\frac{\gamma_p^2}{\gamma^2} u_a^* \right) \right]. \tag{10c}$$

Equation (9) is to be solved for the eigenvalue $\gamma\ (k_s,\ t)$ (the growth rate) subject to the conditions that $\hat{u}_s$ is regular at the origin and corresponds to outgoing waves as r$\rightarrow\infty$. The eigenvalue γ depends parametrically on time and scattered wavenumber k_s. We will be interested in the cumulative growth $\Gamma(k_s) = \int dt\, \gamma(k_s, t)$ which determines the growth in perturbations with different modulation wavenumbers $k_m = k_s - k_a$. The observed modulations are presumably the ones that correspond to the largest value of Γ. Numerical solutions of Eq. (9) will be presented in the next section. Here we will discuss qualitatively the types of solutions that can be found. First it is necessary to describe the physics of the channel formation. Figure 2 shows radial profiles of electron density, electron temperature and ionization

rate at three different times t= 88, 138, and 188 ps, during the formation of the channel. These are obtained from our one-dimensional hydro-code [50] and correspond to the illumination of 380 torr of argon by a 100 ps, $5x10^{13}$ W/cm^2 vacuum intensity 1.064 μm wavelength laser pulse. The basic process of channel formation is evidenced in Fig. 2a where the density profiles are shown. Initially the gas is broken down and the electron density peaks on axis. The electrons are collisionally heated to a temperature in the range of 70 eV as shown in Fig 2b, and thermal expansion begins to drive an outward propagating shock wave. By 90 ps the electron density profile has become inverted. At later times the channel broadens further and the temperature drops as electron thermal energy is used to drive the shock wave. The shock front is visible in Fig. 2c where the local ionization rate peaks. The example shown in Fig. 2 corresponds to a relatively high pressure for which the channel electron density is high enough to modify the axicon field profile. This is shown in Fig. 3 where the magnitude of the axicon field is plotted at the first two times shown in fig. 2. As can be seen, early in the pulse the axicon field reaches the axis, while as the channel forms and expands the axicon field is excluded from the central region of the channel.

We now discuss the general features of the modes that are described by Eq. (9). The first type of mode is associated with the singular points of the equation where the coefficient of the second derivative term vanishes, $M = 0$. At any given radial point the condition M=0 defines a local dispersion relation that is cubic in growth rate. Two of the modes can be associated with the nonlinear beating of the scattered and axicon fields that act through the heating and ponderomotive force to

produce density modulations. The third mode exists even in the absence of this beating and is given by $\gamma = \nu_I(2-\eta)$. This mode, which we will refer to as the ionization mode, arises because of the strong dependence of the collisional ionization rate on electron density. Regions of space with elevated electron density have elevated ionization rates and in these regions the electron density grows even faster. The stabilizing term involving the logarithmic derivative with respect to temperature of the ionization rate results from the fact that at fixed pressure, as the density goes up the temperature drops. During the course of the formation of the channel the local instantaneous ionization rate varies considerably as shown in Fig. 2c. Initially the ionization rate is large on axis, but as the central region of the channel becomes ionized the local rate eventually drops. However, as the channel expands outward there is a region of ionization at the edge of the channel. We will find that there is usually an ionization mode that can be found somewhere in the channel.

The other two modes associated with the singular points *M = 0*, are driven by the beating of the axicon and scattered fields. If we neglect the ionization rate, and consider these modes to act separately they would have growth rates given by

$$\gamma^3 = \frac{\omega_0 |u_a(r)|^2}{2(\omega_0 + i\nu)} \gamma_0^3 \tag{11a}$$

and

$$\gamma^2 = \frac{\omega_0 |u_a(r)|^2}{2(\omega_0 + i\nu)} \gamma_p^2 \tag{11b}$$

Comparing these expressions, along with the definitions of γ_0 and γ_p, we see $\gamma_p^2 \approx \gamma_0^3/(3\nu)$. Thus, $\gamma_p < \gamma_0$ as long as $\gamma_0 < \nu$, which turns out to be the case. Thus, the dominant nonlinearity is the modulated heating that results from the beating of the axicon and scattered wave fields.

A second basic type of mode is associated with the global solution of Eq. (9) rather than the local solution $M=0$. This mode is best understood as a weakly damped, quasi-bound mode of the channel that is coupled to the density perturbation through the axicon field. To analyze this mode we imagine that the scattered field profile is close to that of the guided mode, which satisfies:

$$\left[\nabla_\perp^2 + 2i\frac{\omega_0}{c^2}(-\gamma_d) + \kappa^2(r,\omega_0,k_g)\right]u_g = 0, \tag{12}$$

where k_g is the axial wavenumber of the guided mode and γ_d is the temporal damping rate of the guided mode due to the combination of energy leakage through the wall of the channel and collisional dissipation in the channel. The guided mode will have an axial wavenumber that is close to, but different from the scattered wavenumber k_s, which at this point is a parameter to be specified. We obtain an approximate dispersion relation by inserting $\hat{u}_s \approx \hat{u}_g$ in Eq. (8), multiplying by $\hat{u}_g^*$ and integrating over radius,

$$2\frac{\omega_0}{c}\left[\frac{i}{c}(\gamma+\gamma_d)-(k_s-k_g)\right]\int 2\pi r dr\left|u_g\right|^2 =$$

$$\int 2\pi r dr\,\frac{u_a u_g^*}{\Delta}\left[\nabla_\perp^2\left(\frac{\gamma_0^3}{\gamma^3}u_g u_a^*\right)+\nabla_\perp\cdot\left(\frac{\gamma_p^2}{\gamma^2}\nabla_\perp u_g u_a^*\right)+\frac{\omega_p^2}{c^2}\left(\frac{\gamma_I^2}{\gamma^2}+\frac{\gamma_s}{\gamma}\right)u_g u_a^*\right] \tag{13}$$

If we assume the growth rate is larger than the ionization rate such that $\Delta \approx 1$, we may rewrite Eq. (13) as a fourth order polynomial in γ,

$$\frac{2}{k_0}\left[\frac{i}{c}\left(\gamma+\gamma_d\right)-\left(k_s-k_g\right)\right]=\frac{A}{\gamma^3}+\frac{B}{\gamma^2}+\frac{C}{\gamma}, \tag{14}$$

where

$$A=k_0^{-2}\int 2\pi r dr u_a u_g^* \nabla_\perp^2\left(\gamma_0^3 u_g u_a^*\right)/\int 2\pi r dr\left|u_g\right|^2 \tag{15a}$$

$$B=k_0^{-2}\int 2\pi r dr u_a u_g^*\left[\nabla_\perp\cdot\left(\gamma_p^2\nabla_\perp u_g u_a^*\right)+\frac{\omega_p^2}{c^2}\gamma_I^2 u_g u_a^*\right]/\int 2\pi r dr\left|u_g\right|^2 \tag{15b}$$

and

$$C=k_0^{-2}\int 2\pi r dr\frac{\omega_p^2}{c^2}\gamma_s\left|u_g u_a^*\right|^2/\int 2\pi r dr\left|u_g\right|^2. \tag{15c}$$

This dispersion relation (with A=C=0) is closely related to that for the resonant instability of laser filaments in a plasma [55]. In the case of Ref. 34, a strong, self-guided, lowest-order mode of a ponderomotively created channel becomes unstable to the excitation of higher-order modes. In our case the axicon field replaces the strong, lowest-order mode and the unstable perturbation is the lowest order mode of the thermally created channel.

We anticipate that unstable modes will grow on the hydrodynamic time scale with wavenumber shifts on the order of the mode damping rate, $\delta k = k_s - k_g \approx k_d = \gamma_d/c$. This growth rate is much smaller than the temporal damping rate of a guided mode. Consequently we assume $\gamma << \gamma_d$ and drop γ on the left side of Eq. (14). Equation

(14) is then a cubic polynomial. The most unstable growth rate will depend on the sizes of the coefficients A, B, and C. Roughly, we can say that the most unstable mode will satisfy,

$$\gamma = Max\left\{\mathrm{Re}\left[\left(\frac{k_0 A}{2(ik_d - \delta k)}\right)^{1/3}\right],\quad \mathrm{Re}\left[\left(\frac{k_0 B}{2(ik_d - \delta k)}\right)^{1/2}\right],\quad \mathrm{Re}\left[\left(\frac{k_0 C}{2(ik_d - \delta k)}\right)\right]\right\}.$$

Since the coefficients *A*, *B*, and *C* are all proportional to the axicon pulse intensity, as intensity is increased from zero the mode depending on *A* will have the largest growth rate. We thus set $B = C = 0$ and focus on this mode. In this case Eq. (14) can be recast,

$$D(\gamma, \delta k) = \gamma^3 + i\, sign(A)\Gamma_0^3 / [1 + i\delta k / k_d] = 0\,, \tag{16}$$

where $\Gamma_0^3 = \left[|A| k_0 / (2k_d)\right]$ is the nominal growth rate. Instability occurs for either sign of *A*. We estimate the magnitude of *A* from (15a) as,

$$|A| \approx \frac{\gamma_0^2}{k_0^2 r_{ch}^2} = \frac{2}{3}\frac{\omega_p^2}{\omega_0^2}\tau_{heat}^{-1}\tau_{hydro}^{-2},$$

where $\tau_{heat}^{-1} = m_e \nu |V_{osc}|^2 / T_e$ is the local heating rate and $\tau_{hydro}^{-2} = p_0 / (n_0 m_i r_{ch}^2)$ is the hydrodynamic expansion rate where p_0 is the equilibrium pressure and r_{ch} is the channel radius. Based on this estimate, the nominal growth rate scales as $\Gamma_0 = \left[Q\omega_p^2 \tau_{heat}^{-1}\tau_{hydro}^{-2} / \left(3\omega_0^2\right)\right]^{1/3}$ where $Q = k_0/k_d$ represents the waveguide quality factor. Growth can occur on a time scale faster than the hydrodynamic time scale if the quality factor is large enough.

Using the dispersion relation (16) we can evaluate the space-time evolution of disturbances initiated at z=0 at t=0. This is done following the procedure outlined in ref. 56. Specifically we simultaneously solve $D(\gamma - i\delta kz/t, \delta k)=0$, and $\partial D(\gamma - i\delta kz/t, \delta k)/\partial \delta k=0$ to find γ and δk as functions of z/t. We then estimate the growth of the disturbance by evaluating $\mathrm{Re}[\gamma t+i\delta kz]$. We find the density perturbation grows as

$$|\hat{n}| \approx \exp[-k_d z + 2\cos(\pi/8)(\Gamma_0 t)^{3/4}(k_d z)^{1/4}]$$

Thus, for fixed axial location disturbances grow slower than exponentially. The rate of growth increases with axial distance. However, there is exponential damping with distance due to losses of the guided mode. If we maximize the growth over axial position we find the peak of the disturbance moves with constant speed,

$$k_d z_{peak} = \left(\frac{\cos(\pi/8)}{2}\right)^{4/3} \Gamma_0 t .$$

The amount of growth at this moving location is proportional to time,

$$|\hat{n}|_{peak} \approx \exp[3\left(\frac{\cos(\pi/8)}{2}\right)^{4/3} \Gamma_0 t].$$

Thus, the growth rate Γ_0 characterizes the instability. The main conclusion is that the instability is absolute in the lab frame, and the rate of growth can be estimated to be that which maximizes $\gamma(k_s)$.

Numerical solutions to mode equations

Now we turn our attention to numerical solutions of Eq. (9). As was pointed out previously, we must solve Eq. (9) for the eigenvalue $\gamma(k_s)$, with requirements on

the solution that it is regular at the origin and correspond to outward propagating waves for larger radius. The coefficients, M, N, and Q defined in (10), each depend on the unperturbed channel density and temperature distributions and the axicon field profile either directly or through differential operators. These distributions can be obtained using the 1D hydrodynamic code [50]. This hydrodynamic code provides self-consistent plasma densities and temperatures as well as the axicon fields at each 2.5 ps time interval during the formation of the plasma channel. The results of this code have been well characterized [50] and agree with experiment. Sample profiles are illustrated in Figs. (2) and (3) for three different times during the formation of a channel.

To begin, we examine the eigenvalue and mode structure at one particular time, 88 ps, for a high-pressure case of 380 torr of argon to determine which type of mode discussed previously is dominant. Figure 4 shows the real and imaginary parts of the complex eigenvalue for the case of 380 torr of argon. Shown are normalized growth rates, γdt, where dt = 2.5 ps., for three different azimuthal mode numbers m= 0, 1, and 2, and for each m-value there are several modes that are distinguished by their radial profile. In this figure, and subsequent figures, the scattered wave number k_s was chosen to correspond to the wave number that maximized total (time integrated) growth for the parameters under consideration, and this will be discussed subsequently. The eigenvalues and scattered mode solutions were determined using a shooting method to integrate Eq (9) by starting from r_{max} where the solution matched an outward propagating wave; $H_m^1(\kappa r_{max})$, where H_m^1 is an m^{th} order Hankel function of first kind. Here r_{max} is taken to be well outside the plasma region. We then

searched for an eigenvalue such that the solution was regular at the origin, *r=0*, e.g., $du_s/dr = 0$ for m=0 or $u_s = 0$ for $m \neq 0$. Several different modes were identified, depending on the initial guess for the eigenvalue in the search routine. We have also included as open symbols solutions for the case where the ionization effects in Eq (9) have been removed, specifically, $\nu_I = 0$. These solutions, with no ionization effects, have lower growth rate, and all contain nonzero frequency shifts. The importance of this last point will be emphasized later.

Notice that the largest growth rate occurs for an m=1 mode with virtually zero frequency shift. There is also an m=1 mode with slightly lower growth rate and a larger real frequency, as well as what appears to be a marginally stable m=1 mode. Figure 5 shows radial profiles for each of the growing modes as well as the real part of the equivalent potential, *Q(r)/M(r)* in Eq. (9). In the case of the highest growth mode, Fig. 5(a), we see a pole of the potential is near the real-r axis at approximately *r*= 3 μm. This pole is associated with a singular point, *M=0*, in Eq. (9) and is primarily determined by the ionization, $\gamma \approx (2-\eta)\nu_I(r)$. The derivative of the scattered field changes abruptly near the pole as is expected for the solution near the singular point. The mode profile and equivalent potential for the lower growth rate m=1 mode of Fig. 4 is shown in Fig. 5b. This mode has a greater radial extent than the highest growth mode. There appears to be a slight well in the effective potential near 2 μm that contains the mode. In contrast to the high growth rate mode, this mode is not associated with a singularity in Eq (9).

Figure 6 shows the incremental growth γdt, where dt=2.5 ps, as a function of time during the channel development for two different pressures, 200 torr and 380 torr of argon. The fastest growing mode for 200 torr argon has m=0 while for 380 torr the fastest growing mode has with m=1. The maximum growth rates appear to occasionally jump with time. We believe that this is a consequence of our numerical solutions of Eq. (9) and our procedure for finding roots. The modes that we seek have singularities close to the real-r axis, making them sensitive to gridding. Further, we generate new profiles only every 2.5 ps, and sometimes it is difficult to follow a root from one time step to the next.

It is apparent from this figure that for the high-pressure case the majority of the growth occurs early in the channel evolution. This is in contrast to the low-pressure case in which most growth occurs toward the end of the simulation. This timing can be understood in terms of the dominant mechanism for the unstable growth. In the high-pressure case, the early growth is dominated by ionization physics and modes are of the type shown in Fig. 5a. To confirm this hypothesis we examined the mode for the fastest growing period. Figure 7a shows the field $|E_s|^2$ and the potential Q(r)/M(r) for the fastest growing mode during the pulse in the 380 torr case. This mode occurs at 75 ps, as seen in figure 6, prior to the plasma channel formation at approximately 90 ps. This mode is clearly centered on the pole in the effective potential. This mode is due to the singular point in Eq. (9) and is dominated by the ionization rate. For the 380 torr case the singular point in Eq (9) continues to dominate the dynamics until approximately 150 ps. After this time the growth associated with this ionization mode is less then the growth associated with the global

solution within the channel region. This change in behavior is apparent from the kink in the growth curve at 150 ps.

The ionization mechanism is also active at very early times for the low-pressure case e.g., before the channel forms and a well-defined resonant mode exists, prior to 100 ps. However, as the channel evolves for the low-pressure case the growth associated with the singular point due to ionization decreases and the coupling to quasi-guided modes begins to dominate. This situation can be seen in figure 7b, which presents results from the lower pressure calculation, 200 torr argon at 175 ps. Notice that $|E_s|^2$ is localized on axis in the potential well formed by the plasma channel. For this type of mode the analysis leading to Eq. (14) is expected to be valid. Here there is an enhancement at the scattered mode wave number $k_s > k_a$. This mode is a global mode, which depends on the solution to Eq. (9) rather then a local ionization mode at a singular point of the equation. This type of mode is not found in the high-pressure case, where the axicon field is excluded from the axis as shown in Fig. 3.

We have repeated this numerical calculation for a wide range of pressures and scattered modes wavenumbers. Figure 8 presents a comparison of the total growth of the most unstable mode for the case of 380 torr argon with m=0, 1, and 2 and 200 torr argon m=0 for many values of scattered wave number. Notice that for the 200 torr case, the growth has a sharp peak at the resonant wave number $k_s = k_g$. For the 380 torr case the growth is less localized in scattered wave number. This observation is consistent with the discussion presented above since the low pressure is dominated by a global mode, i.e., quasi-guided, while the high pressure is dominated by local

ionization modes. However, there is still a scattered mode that maximizes growth even in the high-pressure case.

Figure 9 shows the experimental modulation wave number versus gas pressure for several pressures. Also on figure 9 are the modulation wavenumbers corresponding to the largest total growth. The calculated modulation wave numbers agree well with experiment including the rapid change as a function of pressure. Figure 10 compares the cumulative growth for the most unstable mode for 380 and 200 torr. The 380 torr case has 6 more exponentiations then the 200 torr case. Thus the high-pressure case is more unstable to this modulation instability then the low-pressure case. Further, the high-pressure case has significant growth by the middle of the simulation, 15 exponentiations by 120 ps. The 200 torr case has approximately six exponentiations by the middle of the simulation. Thus, we would expect enhanced coupling of the scattered mode to the plasma channel in the 380 torr case compared to the values obtained. Where as for the 200 torr case, the model calculation is likely valid over the duration of the simulation since significant mode growth e.g., 15 exponentiations, does not occur until near the end of the simulation, 200 ps.

Conclusions

We have presented the first experimental evidence of an instability in the generation of plasma channels using axicon field breakdown at moderate gas pressures and pulse duration. We have described a model to describe this instability, and shown that the instability is parametric in nature. This instability is associated with the non-linear coupling of a scattered mode to the incident axicon field through

ionization, heating, and ponderomotive physics. We show that this model accurately predicts the unstable scattered wave number and accounts for the strong pressure dependence of the instability.

It is also interesting to notice that the most unstable mode at moderate pressures e.g., 380 torr, has m=1 azimuthal mode not m=0. Therefore, this instability may also explain the finding by Fan et. al. [50] that at pressures above resonant coupling, 300 torr for this axicon base angle, the time integrated mode structure at the end of the plasma channel had m>0. This observation and the onset of this instability may preclude use of axicon formed plasma channels for pressures above the resonant coupling pressure. However, it might be possible to design plasma channels to provide efficient coupling to either high harmonics or predetermined wave number by allowing tight control of axially periodic structures in plasma channels.

Figures

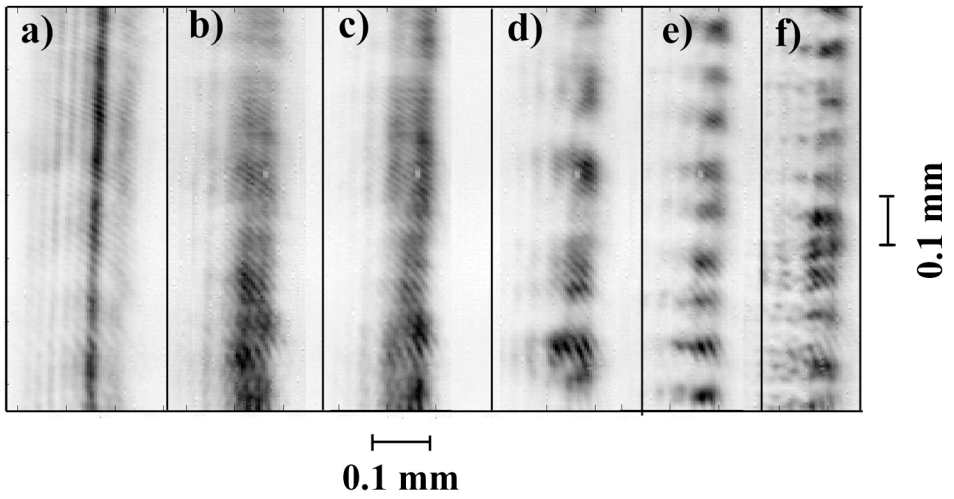

Figure 1. Shadowgrams of channels formed in argon for different pressures: a) 200 Torr, b) 280 Torr, c) 300 Torr, d) 340 Torr, e) 370 Torr ands f) 420 Torr. Laser pulse: 100 ps FWHM, λ=1064nm, and peak intensity $5 \times 10^{13} W/cm^2$; axicon base angle 25°.

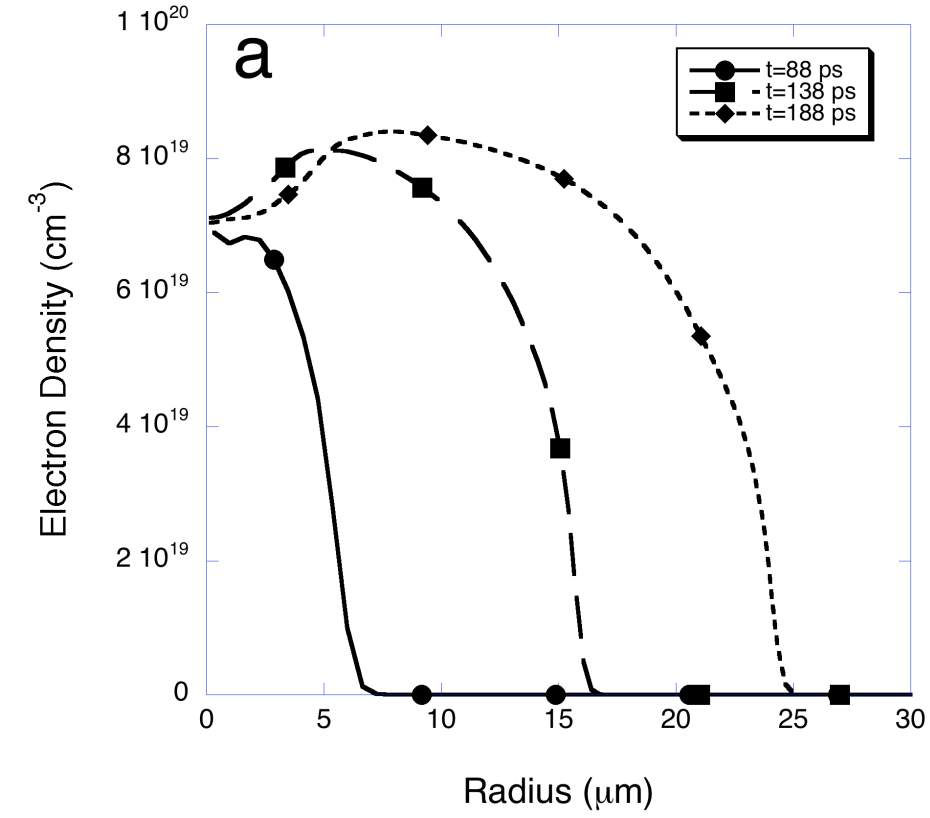
a
t=88 ps
t=138 ps
t=188 ps
Electron Density (cm-3)
1 10^20
8 10^19
6 10^19
4 10^19
2 10^19
0
0
5
10
15
20
25
30
Radius (μm)

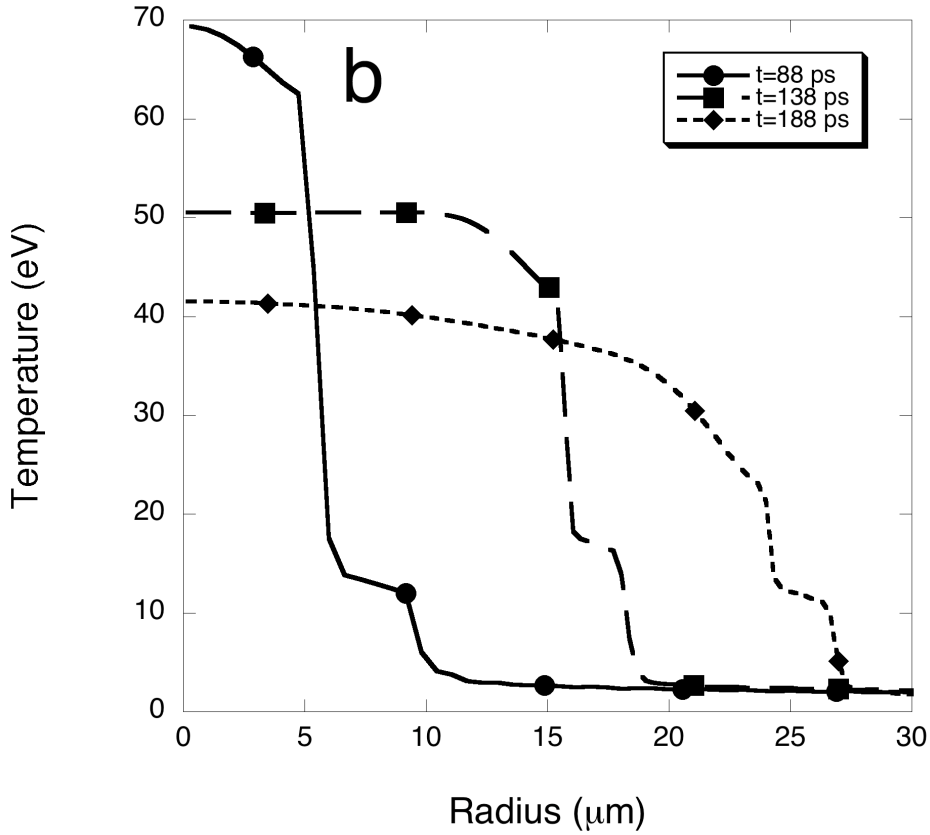
b
t=88 ps
t=138 ps
t=188 ps
Temperature (eV)
70
60
50
40
30
20
10
0
0
5
10
15
20
25
30
Radius (μm)

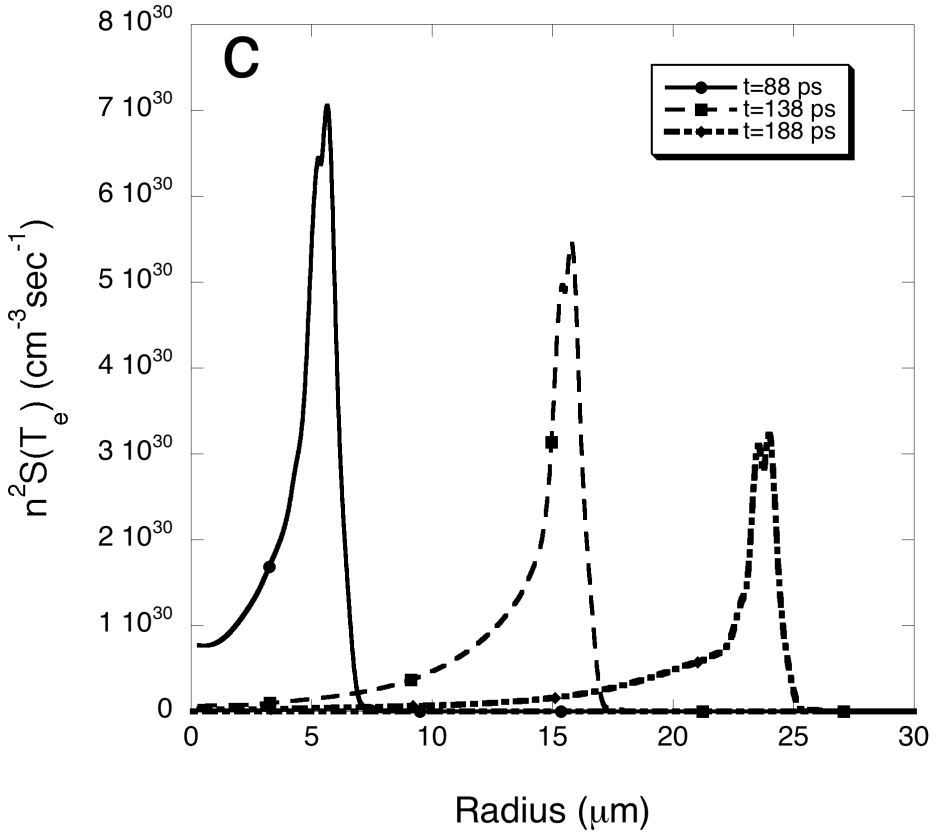

Figure 2 simulation results at three different times during the evolution from the 1D hydrodynamic code [50] for a simulation pressure of 380 torr argon and a laser pulse with peak intensity $5x10^{13}$ W/cm^2. The figures present the (a) electron plasma density (b) electron temperature in electron volts, (c) ionization rate given by $n^2S(T_e)$. Notice that the channel is just starting to appear at 88 ps and that the interior parameters of this channel are relatively stable once formed. Also notice that the ionization front moves radially out as the channel expands.

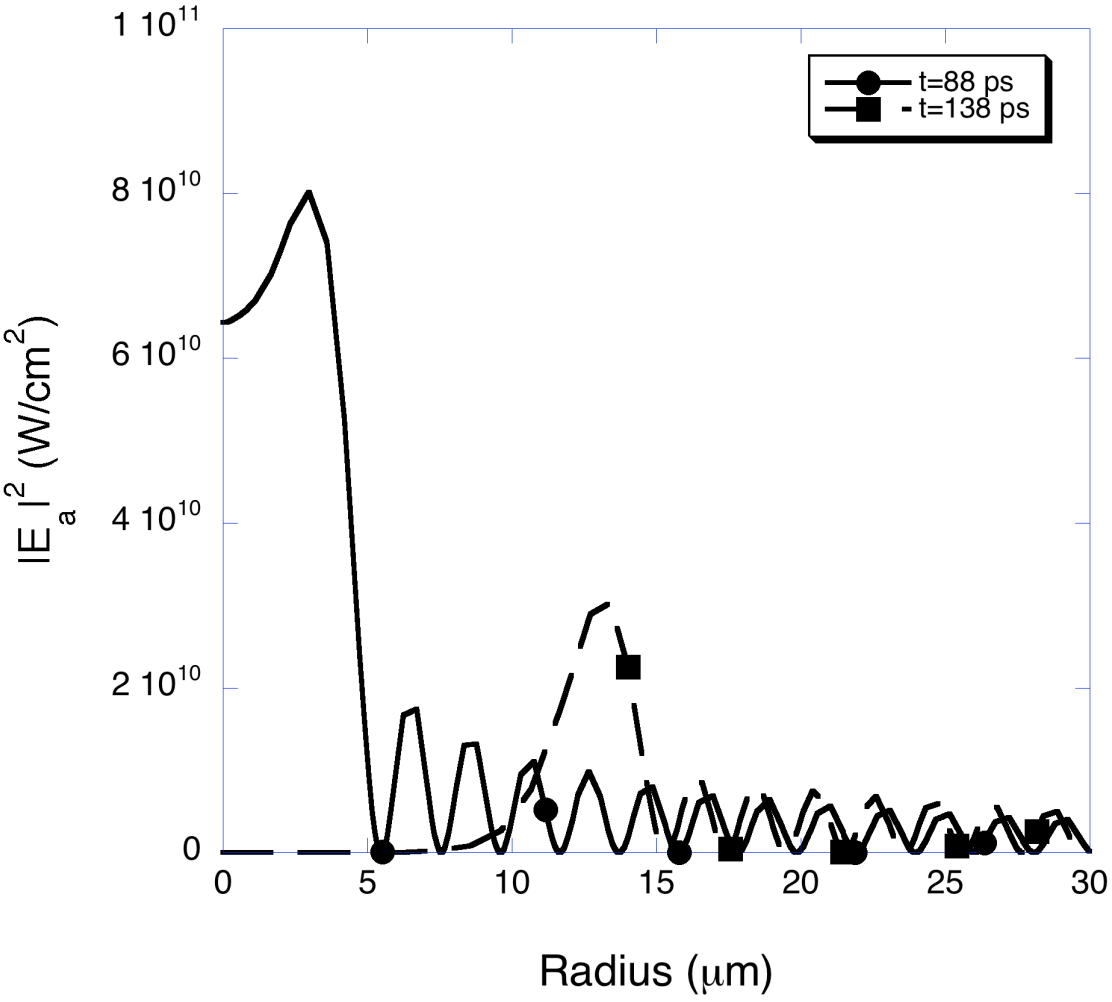

Figure 3, Results of the self-consistent axicon field evolution as calculated with the 1D hydrodynamic code [50]. Notice that even by 88 ps when the channel has just started to form, the axicon field is beginning to be suppressed on the channel axis. This suppression is complete by 138 ps.

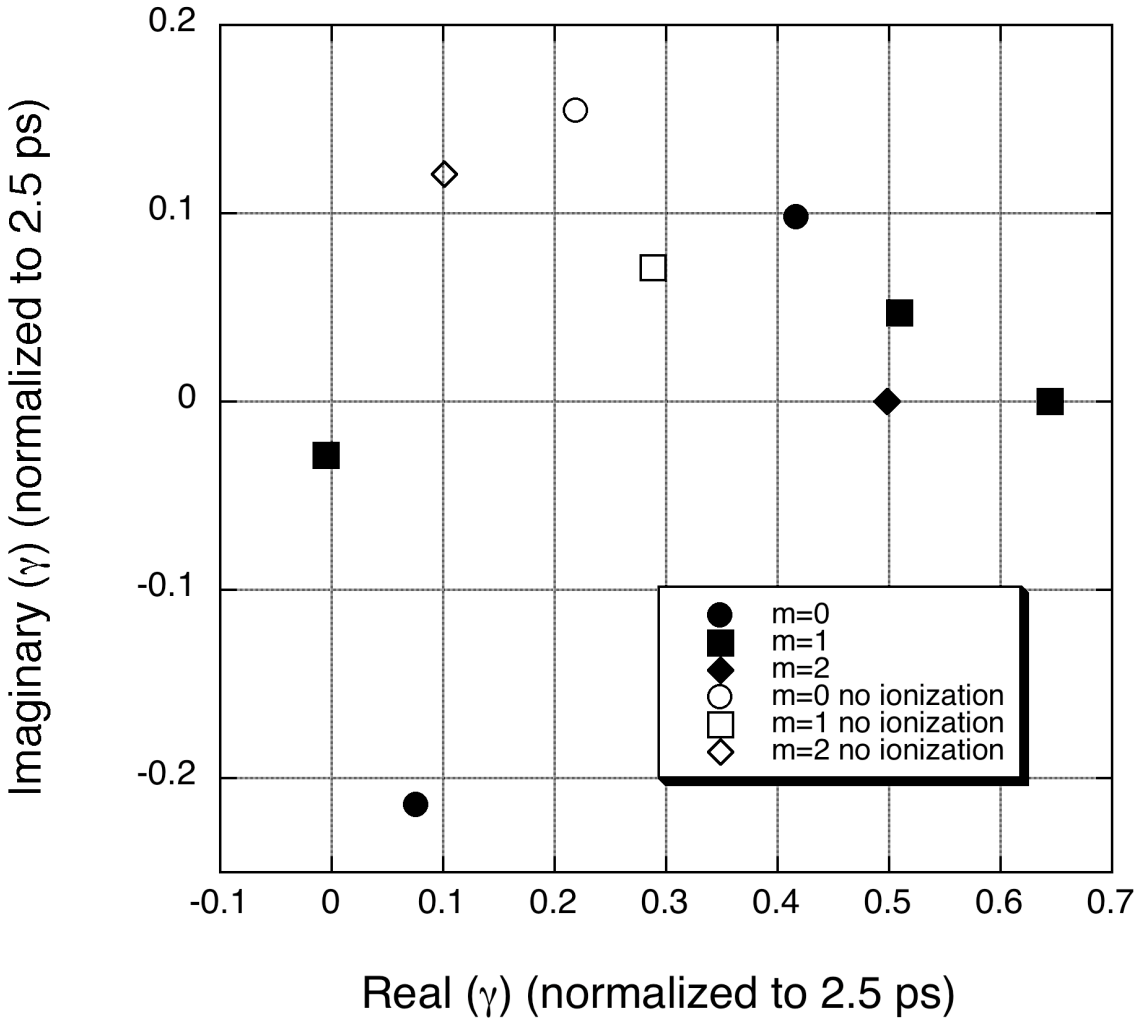

Figure 4, location of the complex growth, γ, during a 2.5 ps interval, obtained by solving Eq. 9 at one particular time, 88 ps. Solutions to Eq 9 without ionization effects are included to emphasis the importance of the ionization process on the modes with no frequency shift $\mathrm{Im}(\gamma) \cong 0$. Several modes have been identified depending on the azimuthal mode number, m, and on the initial search parameters.

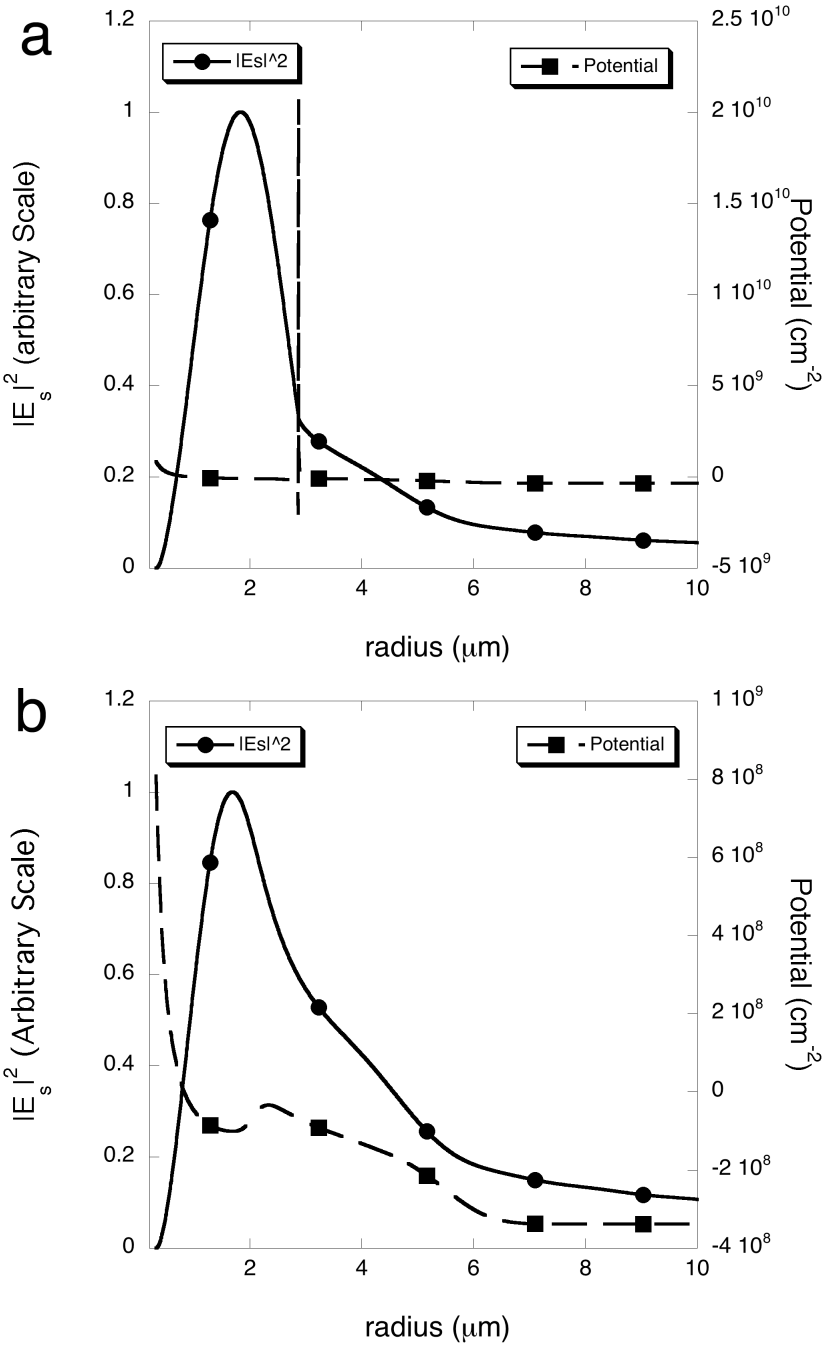

Figure 5, solution functions for Eq (9) for two of the m=1 modes depicted in figure 4. Both the scattered mode $|E_s|^2$ and the real part of the potential function, Q/M, are shown. Figure (a) corresponds to the mode that has negligible frequency shift and a growth of approximately 0.65. Figure (b) corresponds to the mode with positive frequency shift and a growth of approximately 0.5. Notice in (a) that the potential function has a complex pole near the real axis. This pole corresponds to a singular point in Eq. (9) when M(r) = 0. This local singular point appears to dominate the dynamics when this singular point can be found.

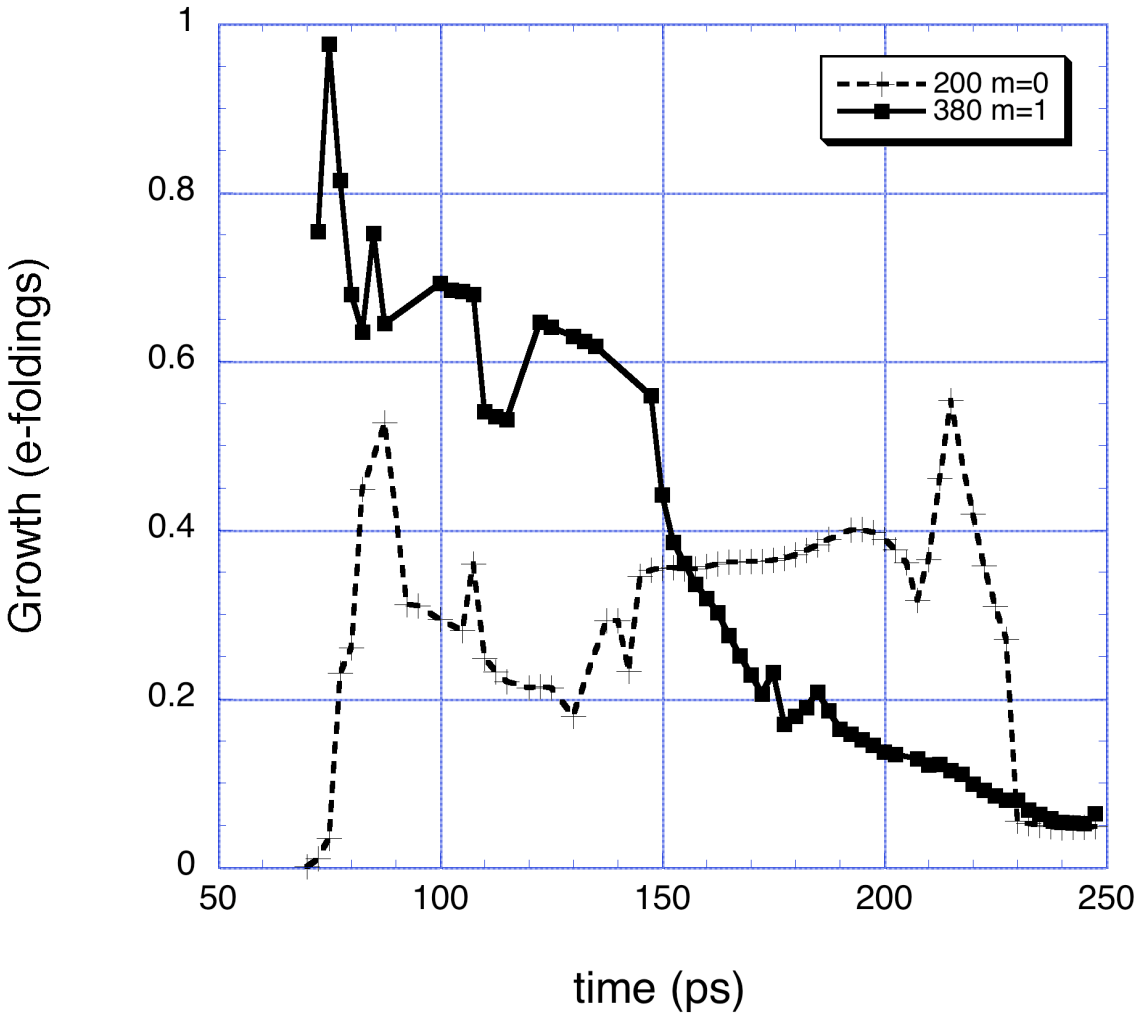

Figure 6 Instantaneous growth verse time during pulse for both the 200 torr case and the 380 torr m=1mode. Notice the 380 torr case has significant growth in the early part of the pulse, while the 200 torr case has most of the growth after the center of the pulse has passed, at 120 ps. This timing can be understood in terms of the dominant mechanism, ionization in the high-pressure case and mode coupling in the low-pressure case.

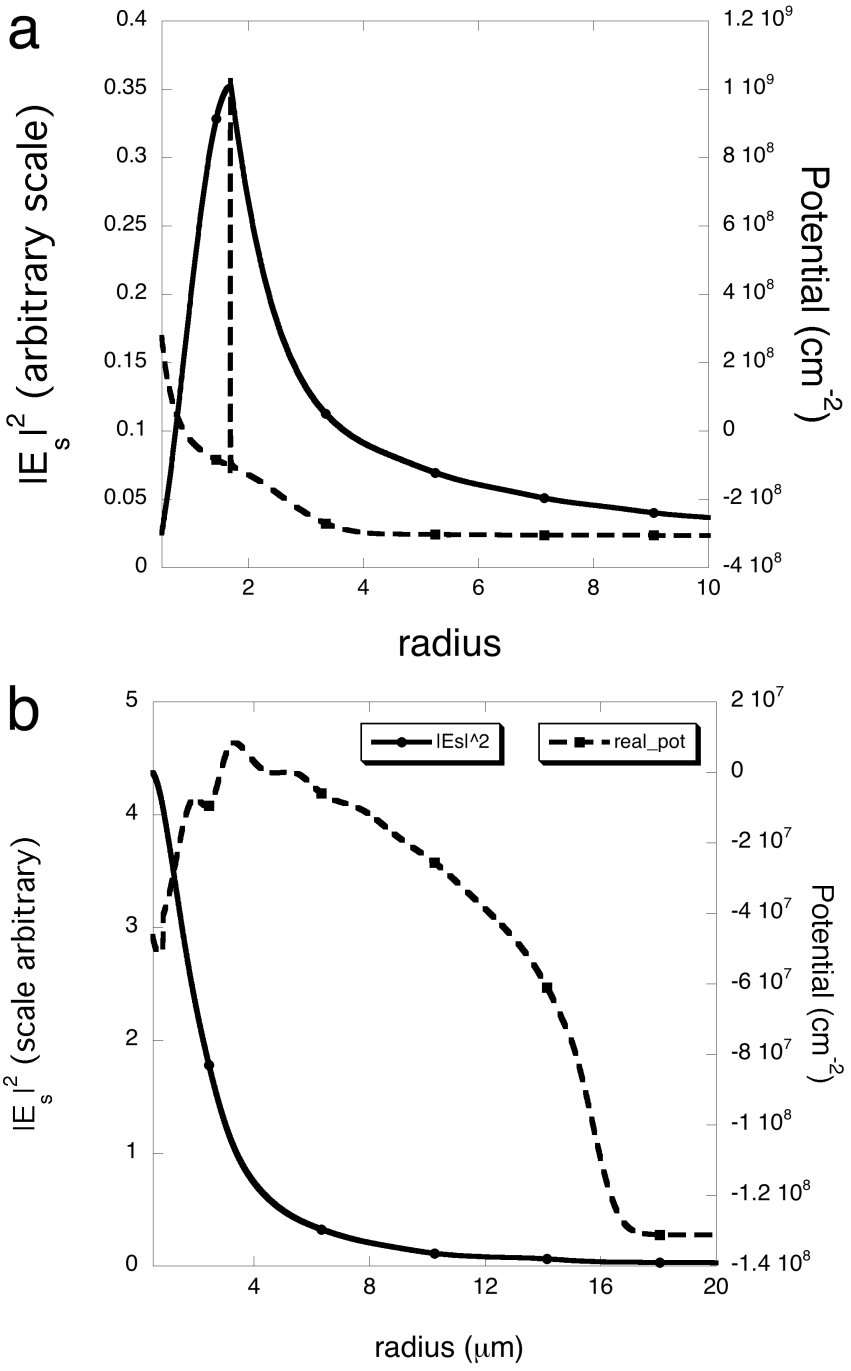

Fig 7. (a) Scattered field $|E_S|^2$ and potential function Q/M at the fastest growing point during the calculation. This mode occurs before the plasma channel has been formed due to electron density inversion, which happens at approximately 90 ps. This mode is clearly centered on the local singular point of the equation. This singular point is driven by the ionization rate and corresponds to an ionization mode. (b) Scattered wave $|E_s|^2$ and potential function Q/M for low-pressure case, 200 torr. The scattered field is localized in the plasma channel with significant enhancement relative to the outward propagating field in the outer radius.

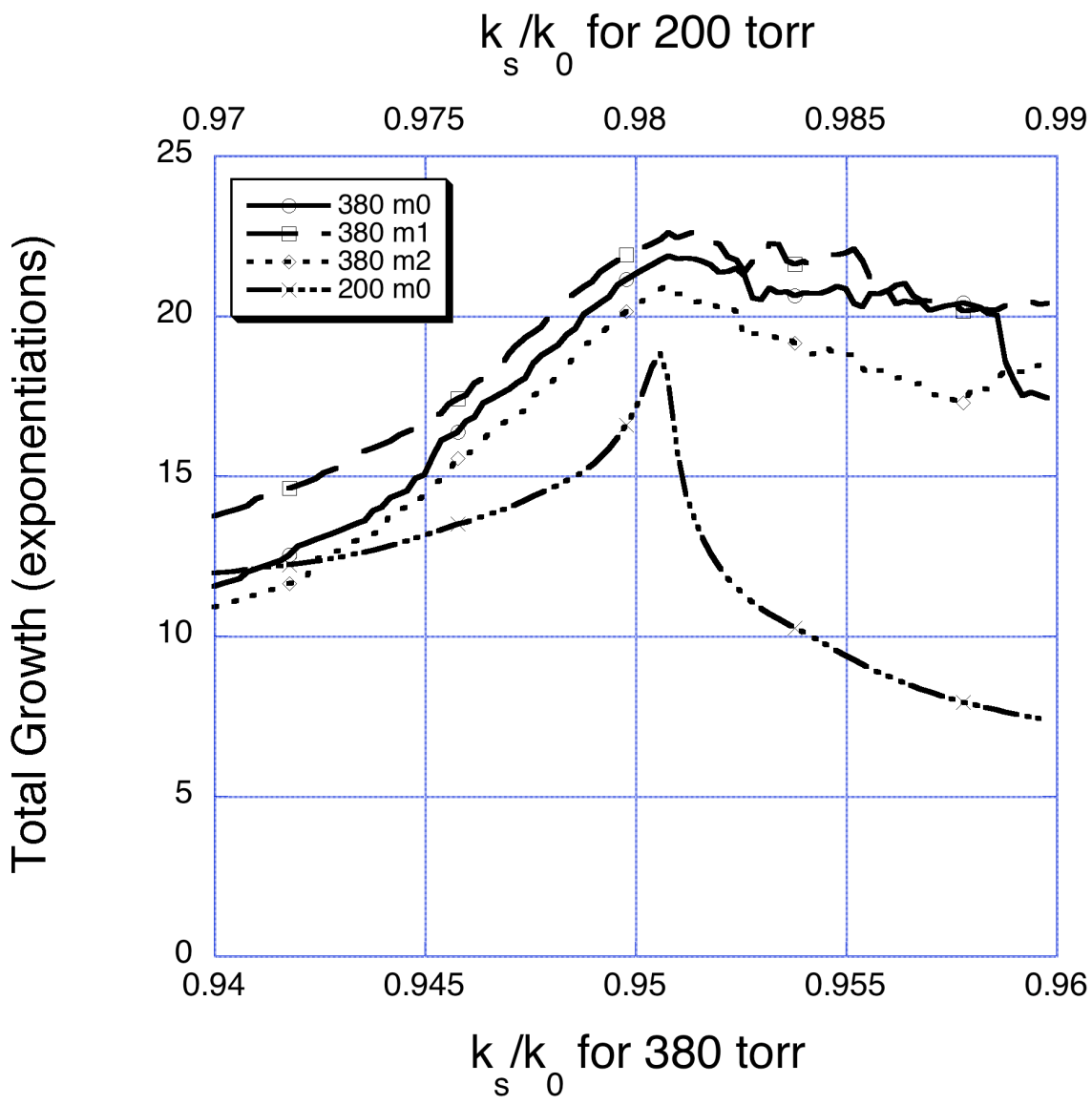

Figure 8, Total instability growth for m=0,1,2 for 380 torr argon and m=0 for 200 torr argon. The 380 torr cases are referenced to the lower axis and the 200 torr case refers to the upper x-axis. The location of the maximum growth corresponds roughly to the scattered wave number predicted using the linear theory. However, for the high pressure case there is little resonance since the local dispersion created by the ionization process dominates. For the low pressure case there is more resonant behavior; however the growth in this mode is less pronounced.

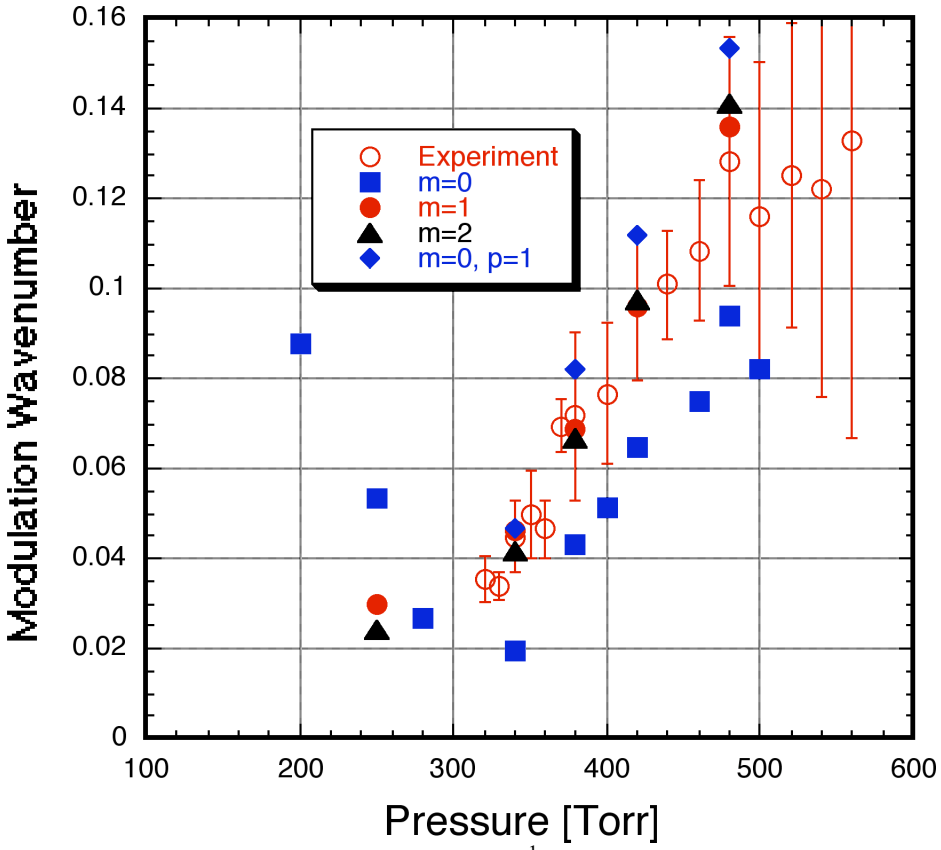

Figure 9. Modulation wavenumber [μm^{-1}] versus pressure [torr]: the open circles are the measured data along with error bars, the solid symbols and the calculated vales for different modes of the channel.

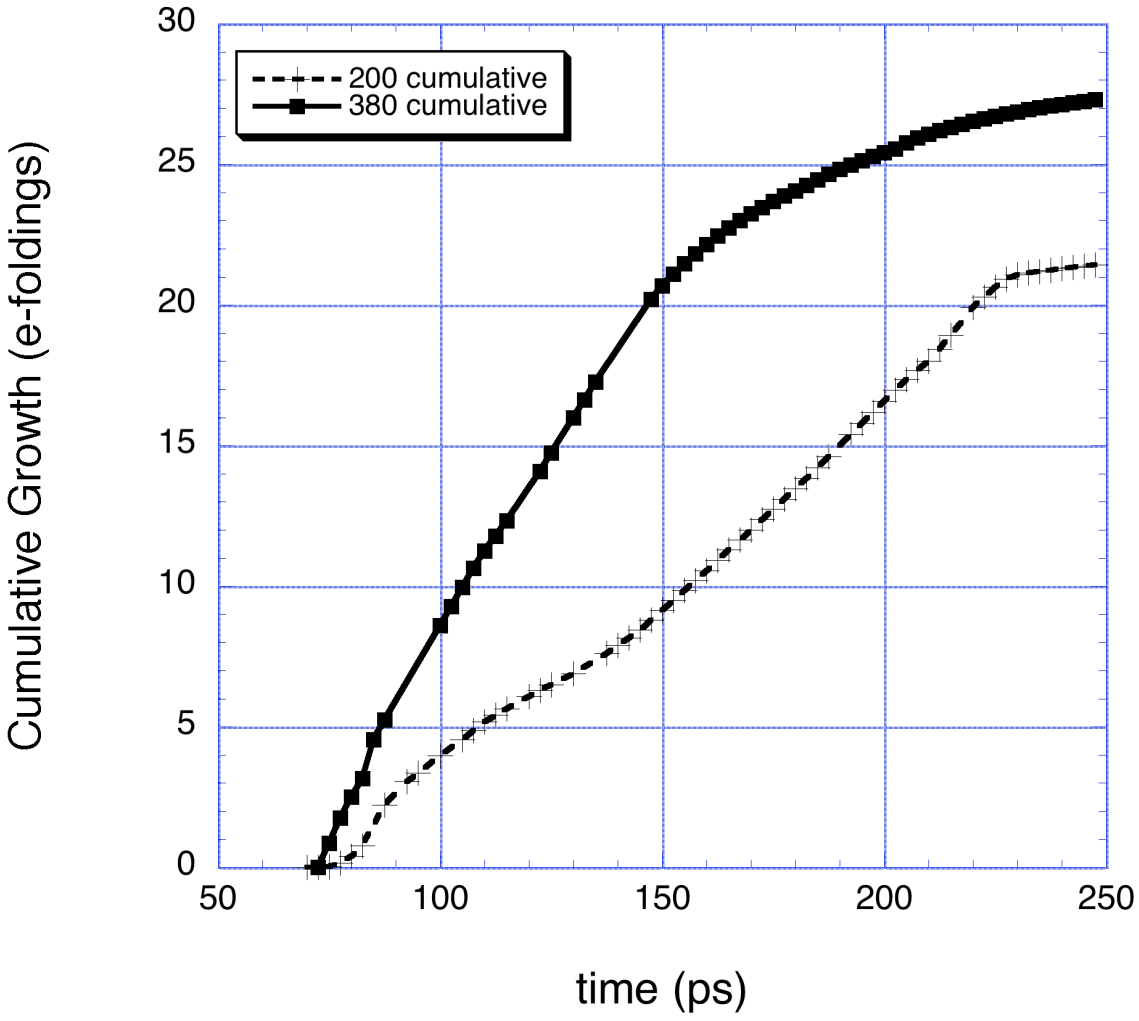

Figure 10 Cumulative growth of the unstable mode for both the 200 torr m=0 mode and the 380 torr m=1 mode. Notice that by the middle of the laser pulse, 120 ps, the high 380 torr mode has nearly 15 exponentiations while the 200 torr mode does not achieve this milestone until nearly 200 ps, near the end of the pulse.

Chapter 3: Three-dimensional modeling of laser pulse propagation in tenuous gas and plasma

Introduction

Advances in laser amplification (Chirped Pulse Amplification) have enabled low cost laser systems with peak intensities $\geq 1\times10^{18}$ W/cm^2 to be developed [57]. These systems have increased interest in the interaction of high intensity lasers with tenuous gas or plasma. Some potential applications of these systems include laser wake-field acceleration (LWFA) [1], x-ray generation [58], high harmonic generation [59]and non-linear optics [60]. Due to the complex, non-linear behavior of both the plasma and the laser, theoretical investigations of these interactions require simulations.

Several levels of simulation sophistication have been applied to understand these complex interactions. The simulations range from one-dimensional self-consistent laser field evolution with a fluid plasma response [61] to three-dimensional, fully electromagnetic laser evolution with a kinetic plasma response [62]. In these kinetic plasma models the particle plasma response is treated using a particle-in-cell (PIC) technique [63], which evolves many finite-sized quasi-particles according to Newton's equations of motion, each of which represents a large number of real particles. After each evolution step, the particle plasma quantities, such as charge density, are projected onto a simulation grid. These projected quantities are then used to evolve the laser field. These electromagnetic PIC simulations are used to examine the highly non-linear response of plasmas to very high laser intensities [62].

However, long interaction time simulations using fully electromagnetic PIC codes have been restricted due to the computational cost. This cost can be appreciated in the following manner. Fully electromagnetic simulations must have time steps that resolve the laser oscillation frequency, $\omega_0 \approx 1\times10^{-15}$ sec^{-1}. While simulations of current interest involve lasers propagating from 1 cm to 10 m, $t \approx 3.33\times10^{-11} - 3.33\times10^{-8}$ sec. Therefore, these simulations require $\geq 3.33\times10^{4} - 3.33\times10^{7}$ time steps. Due to these computational considerations, there is a need for a more efficient model.

In this chapter, we present a model for the laser based on an envelope approximation [22,27]. In this approximation, we treat the laser as a plane wave at frequency ω_0 and wave number $k_0 = \omega_0 / c$, where c is the speed of light in vacuum, modified by a complex envelope, which varies slowly compared to the laser oscillations. We treat the effect of the plasma on the laser by including an effective dielectric, $\delta\varepsilon$, that includes the relevant physics. Further, we describe how the effect of the laser can be included in the material response and thus provide $\delta\varepsilon$.

The remainder of this chapter is arranged as follows. In section 2, we present a detailed description of the system of equations describing the evolution of the laser pulse envelope and develop the model we intend to implement. We present the numerical realization of this model in section 3. Validation for the laser pulse evolution is presented in section 4. Section 5 presents an overview of the plasma equations and relevant approximations. In section 6 we conclude and outline future efforts for this code.

Model Equations for the Laser Pulse

We begin the development of our laser pulse propagation model assuming that the laser pulse can propagate in both ionizing gas and plasma. Development of the model equations for the laser envelope will follow that of Wu and Antonsen [27]. The laser field is determined by Maxwell's equations, which in the Lorenz gauge become

$$\left(\frac{1}{c^2}\frac{\partial^2}{\partial t^2}-\nabla^2\right)\mathbf{A}_{laser}=\frac{4\pi}{c}\mathbf{J}+\frac{4\pi}{c}\frac{\partial \mathbf{P}}{\partial t}, \tag{1}$$

where $\mathbf{A}_{laser}$ is the vector potential for the laser field, **J** is the current density of the free charge of the plasma, and **P** is the polarization for the neutral gas. We introduce the envelope approximation $\mathbf{A}_{laser}=\hat{\mathbf{A}}_{laser}(t,\boldsymbol{x}_\perp,z)\exp(ik_0z-i\omega_0t)+c.c.$, where $\hat{\mathbf{A}}_{laser}$ is a complex amplitude that varies slowly in time compared with the laser oscillation period and slowly in space compared with the laser wavelength. The quantities ω_0 and k_0 are the central frequency and wave number of the laser pulse. These are assumed to satisfy the plane wave dispersion relation for light propagating in gas with a dielectric constant, $\varepsilon = 1+\delta\varepsilon_0(\omega_0)$. We also introduce the normalized vector potential $\hat{\mathbf{a}}=q\hat{\mathbf{A}}_{laser}/mc^2$, which is convenient for analysis of the relativistic motion of free electrons in the laser field. Finally, we transform to independent variables $(t, \xi = v_f t - z)$, such that pulses traveling at the speed v_f, the laser frame speed, are independent of time, t.

With these assumptions, we obtain an equation for the envelope $\hat{\mathbf{a}}$ that follows from Eq. (12) of Ref. 27,

$$\frac{2}{c}\frac{\partial}{\partial t}\left(ik_0 - \frac{\partial}{\partial \xi}\right)\hat{\mathbf{a}} + ik_0\left(\beta_1 - \delta\varepsilon_0\right)\frac{\partial}{\partial \xi}\hat{\mathbf{a}} - \beta_2\frac{\partial^2}{\partial \xi^2}\hat{\mathbf{a}} + \nabla_\perp^2\hat{\mathbf{a}} = -k_0^2\delta\varepsilon\hat{\mathbf{a}} \tag{2}$$

In Eq. (2), $\beta_1 - \delta\varepsilon_0 = 2(v_f - v_g)/c$, which accounts for group velocity in the presence of background gas, where $\delta\varepsilon_0$ is the linear dielectric response at ω_0, v_f is the simulation frame velocity and $v_g = \partial\omega/\partial k$ is the laser pulse group velocity. The coefficient $\beta_2 = v_f^2/c^2 - 1 + \delta\varepsilon_0 + 2\omega_0\partial\delta\varepsilon_0/\partial\omega\big|_{\omega=\omega_0} - (1/2)\omega_0^2\partial^2\delta\varepsilon_0/\partial\omega^2\big|_{\omega=\omega_0}$ describes the group velocity dispersion due to the background gas. We use $-k_0^2\delta\varepsilon = \left(\left(4\pi q^2/mc^2\right)n_e/\gamma - 2k_0{}^2 n_2 I\right)$, $\gamma = 1/\sqrt{1 - v_e^2/c^2}$ is the relativistic factor for free electrons, which may be different for each free electron, q is the electron charge, $n_2 I$ represents the second order non-linear polarization of the neutral gas, and $I = (\omega^2/2\pi c)(mc^2/q)^2\left|\hat{\mathbf{a}}\right|^2$ is the laser field intensity. Here we have also assumed the neutral gas polarization responds promptly to the laser field. Additionally, we have assumed v_g, β_2, and $\delta\varepsilon_0$ are constant in space. It is also clear from Eq. (2) that if we choose $v_f = v_g$ then the equation will simplify. Thus, we will choose to work in the frame moving at the linear group velocity for the laser pulse.

The model in Eq. (2) describes a number of physical effects. For instance, the mixed derivative along with the plasma contribution on the right hand side of Eq. (2) allows one to model the reduced group velocity due to the presence of plasma, or due to propagation at an angle to the axis, and depletion of the laser pulse energy due to excitation of plasma wakes. This term also enables modeling of pure forward Raman

scattering, which is neglected in the simple paraxial envelope approximation. The dielectric response on the right hand side includes self-focusing due to neutral gas and relativistic effects as well as excitation of plasma waves.

Numerical Realization

We wish to find a stable numerical approach to solve Eq. (2) in a fully three-dimensional simulation. In addition to the computational cost associated with solving a three-dimensional non-linear partial differential equation, we have the added complication of performing this calculation on a parallel computer system. To this end, we include the constraint that our computational algorithms have an efficient parallel implementation. We start by examining how to evolve Eq. (2) stably, given that it couples second order derivatives in both ξ and $\mathbf{x}_\perp$. We choose to apply a split step algorithm [65] in which a general, partial differential operator is separated into two operators, L_0 and L_1, such that the evolution equation is written,

$$\left(\frac{d}{dt} + \tilde{L}_0 + \tilde{L}_1\right)\hat{\mathbf{a}} = 0\,, \tag{3}$$

where $d/dt \equiv \partial/\partial t - (1/ik_o)\partial^2/\partial t \partial \xi$. Equation (3) is then solved approximately by alternately solving the discrete time equations

$$\frac{\tilde{\mathbf{a}}^{t+dt} - \hat{\mathbf{a}}^t}{dt} + \tilde{L}_0\left(\frac{\tilde{\mathbf{a}}^{t+dt} + \hat{\mathbf{a}}^t}{2}\right) = 0 \tag{4a}$$

and

$$\frac{\hat{\mathbf{a}}^{t+dt} - \tilde{\mathbf{a}}^{t+dt}}{dt} + \tilde{L}_1\left(\frac{\hat{\mathbf{a}}^{t+dt} + \tilde{\mathbf{a}}^{t+dt}}{2}\right) = 0\,. \tag{4b}$$

We introduce the two operators L_0 and L_1, which include the term involving the mixed derivative, and advance the equation in time with $\partial / \partial t$. They are given by

$$L_0 = \frac{ic\beta_2}{4k_0}\frac{\partial^2}{\partial \xi^2} - \frac{ick_0}{2}\delta\varepsilon$$

$$L_1 = \frac{ic\beta_2}{4k_0}\frac{\partial^2}{\partial \xi^2} - \frac{ic}{2k_0}\nabla_\perp^2 .$$

Thus, we see that Eq. (4a) involves derivatives in ξ with transverse coordinate $\mathbf{x}_\perp$ being a parameter and includes the effects of the dielectric while Eq. (4b) involves differentiation in $\mathbf{x}_\perp$ and ξ with no dielectric response. Further more, notice that both of Eqs. (4) have the same form and can be solved implicitly on a grid in ξ.

To solve Eq. (4a), we use a finite difference scheme in ξ in real space. Each of the four terms can be expanded and centered at ξ and $t + dt/2$ as follows

$$\left.\frac{\partial}{\partial t}\hat{\mathbf{a}}\right|_{\xi,t+dt/2} \Rightarrow \frac{\hat{\mathbf{a}}_\xi^{t+dt} - \hat{\mathbf{a}}_\xi^{t}}{dt} \quad , \tag{5a}$$

$$\left.\frac{i}{k_0}\frac{\partial^2 \hat{\mathbf{a}}}{\partial t \partial \xi}\right|_{\xi,t+dt/2} \Rightarrow \frac{i}{k_0}\frac{1}{2dtd\xi}\left[\hat{\mathbf{a}}_{\xi+d\xi}^{t+dt} - \hat{\mathbf{a}}_{\xi-d\xi}^{t+dt} - \hat{\mathbf{a}}_{\xi+d\xi}^{t} + \hat{\mathbf{a}}_{\xi-d\xi}^{t}\right], \tag{5b}$$

$$\left.\frac{ic\beta_2}{4k_0}\frac{\partial^2 \hat{\mathbf{a}}}{\partial \xi^2}\right|_{\xi,t+dt/2} \Rightarrow \frac{ic\beta_2}{4k_0}\frac{1}{d\xi^2}\left\{\left[\hat{\mathbf{a}}_{\xi+d\xi}^{t+dt} + \hat{\mathbf{a}}_{\xi-d\xi}^{t+dt} - 2\hat{\mathbf{a}}_{\xi}^{t+dt}\right] + \left[\hat{\mathbf{a}}_{\xi+d\xi}^{t} + \hat{\mathbf{a}}_{\xi-d\xi}^{t} - 2\hat{\mathbf{a}}_{\xi}^{t}\right]\right\}, \tag{5c}$$

$$\left.\frac{ick_0}{2}\delta\varepsilon\hat{\mathbf{a}}\right|_{\xi,t+dt/2} \Rightarrow \frac{ick_0}{2}\left[\delta\varepsilon_\xi^{t+dt}\hat{\mathbf{a}}_\xi^{t+dt} + \delta\varepsilon_\xi^{t}\hat{\mathbf{a}}_\xi^{t}\right]. \tag{5d}$$

Notice that in this scheme $\hat{\mathbf{a}}$ is known for all ξ and we advance $\hat{\mathbf{a}}$ from t to $t + dt$. Using the difference scheme of Eqs. (5) in Eq. (4a) results in a tri-diagonal system on the ξ-grid. Thus Eq. (4a) can be inverted implicitly using a standard, dual-sweep recursion algorithm [65]. Since our model equation is in general second order in ξ we must have two boundary conditions. At the front of the simulation box we require the laser pulse field to be zero. This is adequate provided that there is limited redistribution of energy in ξ due to group velocity dispersion. The second condition we impose is that the laser pulse smoothly exits the simulation domain at the rear of the simulation. To this end, we calculate the field value just behind the domain by extrapolating the field based on a cubic spline. The field should vary smoothly in ξ and thus we expect the extrapolation to be accurate. One subtlety in Eq. (5d) is the fact that we know the material dielectric response at the current time but Eq. (5d) includes the response at the future time step. We currently assume the susceptibility will vary slowly on the time scale involved and assume the susceptibility is constant. If substantial error is introduced we will modify this assumption and implement a predictor-corrector algorithm [66].

Equation (4b) can be solved efficiently in Fourier space. We obtain a modified version of Eqs. (5) with $\bar{\mathbf{a}}_{\mathbf{k}}$ replacing $\hat{\mathbf{a}}$ and $k_{\perp}^2$ replacing $-k_0^2 \delta\varepsilon$ where $\bar{\mathbf{a}}_{\mathbf{k}}$ is the Fourier coefficient conjugate to $\hat{\mathbf{a}}$.

This numerical scheme is second order accurate in time evolution. Additionally, since Eqs. (4) are solved implicitly there is in general no numerical instability with the difference equation as described by Eqs. (4) and (5). However, there is a requirement on the time step size for this approximate equation to be

accurate. This requirement is $dt < \omega_0 / \omega_p^2$, which is due to the fact that the phase of the laser field should change only slightly during a time step. This requirement places a constraint on the maximum plasma density that can be simulated efficiently.

Equations (4) involve only finite differencing in the axial grid, thus each transverse location can be evolved independently. This separation motivates the parallel implementation used to solve this system. The normal layout of the field involves each node having all axial data and all the data for one transverse coordinate. The second transverse coordinate is divided among the different processors. This layout allows the evolution of Eqs. (4) to be local to a processor. Unfortunately this layout requires two large communications to perform the transverse FFT necessary to evolve Eq. (4b). We take an FFT in the coordinate that is local to the processors then redistribute the data so the other transverse coordinate is local. We can then perform the second FFT in this direction and then solve Eq. (4b). Finally we reverse the process leaving the data in the original layout.

This numerical scheme assumes the laser pulse evolution and dielectric evolution are staggered in time. This means that the laser pulse advances from t to t+dt using the dielectric response at an advanced time, dt/2. Therefore, we must have a method for accurately computing the dielectric response at the advanced time with only knowledge of\the current laser pulse. We extrapolate the laser pulse to the advanced time by solving Eq. (4a) with a time step dt/2. This process approximates the laser pulse at the advanced time and allows calculation of the dielectric response. This process should be accurate provided the effect of the transverse derivative is small.

Validation of Laser Code

Finally, we must validate the numerical algorithms and implementations employed in this code. We start by focusing on the laser benchmarks and demonstrate that the evolution agrees with analytic solutions where applicable. Further comparison with proven codes WAKE[39] and OSIRIS[62] will be presented in the following chapters.

We begin by examining the evolution of the phase for the numerical implementation of Eq. (4a). Solving the finite difference Eqs. (4a) and (5) assuming the amplitude $\hat{\mathbf{a}} \propto \exp\left(ik_\xi \xi - i\omega t\right)$ we obtain the relation between wave number and frequency shift

$$\frac{\tan\left(\omega dt/2\right)}{dt/2} = -\frac{ck_0^2 \delta\varepsilon d\xi}{2\left(k_0 d\xi - \sin\left(k_\xi d\xi\right)\right)} \tag{6}$$

For $k_0 d\xi >> 1$, Eq. (6) can be solved approximately by neglecting the second term in the denominator. We set the plasma response to a uniform density n_e=1x10^{18}, which gives $k_0^2 \delta\varepsilon = 3.536217 \times 10^6 \, cm^{-2}$ and apply only the operator L_0. We can calculate what the change in phase of the envelope, ωdt, should be from Eq. (6), with $k_0 d\xi \cong 7.0686x10^6 >> 1$, $\omega dt = -6.753587168 \times 10^{-10}$ and compare this analytic phase change with the phase change in the numerical evolution $\omega dt = -6.7536578921 \times 10^{-10}$. The difference between these two values is $\delta\varphi = -7.28814 \times 10^{-15}$, which is the same magnitude that the $\sin(k_\xi d\xi)$ term in the denominator becomes relevant compared to $k_0 d\xi$ e.g., $\Delta \equiv 1/k_0 d\xi - 1/(k_0 d\xi - 1) = 2.00140635 \times 10^{-14}$ is the difference with and without

neglecting the second term in the denominator. For $k_0 d\xi \cong 7.0686x10^2 >> 1$ we get $\omega dt = -6.753725 \times 10^{-6}$ from the simulation and $\omega dt = -6.7535872 \times 10^{-6}$ from the analytic formula. In this case the difference is $\delta\varphi = -1.3783885 \times 10^{-10}$ which compares to $\Delta = 2.0042415 \times 10^{-6}$ for the maximum relevance of the neglected term. Based on these results we conclude the numerical implementation is accurate since the difference in phase advance is less then the effect of the neglected term in Eq. (6).

Next we examine the evolution of the laser amplitude over several Rayleigh lengths, $Z_r = \pi r_0^2 / \lambda$. Here r_0 is the laser focal spot size and λ is the wavelength of the carrier wave. We examine the average radius of the laser, $\bar{r}$ where $\bar{r}^2 = \int \left(x^2 + y^2\right)\left|\hat{\mathbf{a}}\right|^2 dxdyd\xi / U_{total}$, U_{total} is the total energy in the laser pulse and $\hat{\mathbf{a}} = a_0 \exp\left(-r^2 / 2r_0^2\right)$. We can compare this average to analytic results, for low laser power. For low laser power, if we assume a gaussian transverse laser profile, we find the average radius depends on the propagation distance according to $\bar{r}^2 = r_0^2\left(1 + \left(z / Z_r\right)^2\right)$. Figure 1 presents a comparison between the simulation results and the analytic results for several Rayleigh lengths. We see that the code accurately accounts for laser diffraction.

Last, we evaluate the laser pulse propagation velocity in the simulation for a laser pulse with a definite transverse wave number. In particular we examine the difference in laser propagation velocity for a plane wave propagating in the z-direction compared to a laser pulse that is propagating at a slight angle to the z-axis. We expect that with no ionization or plasma the laser pulse with no angle relative to the z-axis will propagate at velocity c. For laser pulses with non-zero angle, the

velocity of the pulse in the z-direction will be less then c and will be given by $v_g \simeq c(1-k_\perp^2/2k_0^2)$. We define the slippage distance by $\Delta\xi = (c-v_g)\Delta t$, which is shown in Figure 2. Figure 2 also shows, for several values of angle relative to the z-axis, e.g., $k_\perp$, the distance that the peak of a laser pulse, which propagates undistorted, has moved in the laser frame compared to a laser pulse peak with no angle relative to the z-axis.

Modeling of the Plasma Response: QuickPIC

We now wish to discuss one model for the material response. We will discuss the coupling of the laser model discussed above and kinetic description of fully ionized plasma using a particle-in-cell method. This code will be coupled to a code developed with UCLA that includes relativistic electron dynamics as well as a kinetic treatment for the plasma electron response. The equation for the laser propagating in fully ionized plasma in the frame moving at c can be written as,

$$\frac{2}{c}\frac{\partial}{\partial t}\left(ik_0 - \frac{\partial}{\partial \xi}\right)\hat{\mathbf{a}} + \nabla_\perp^2 \hat{\mathbf{a}} = -k_0^2 \delta\varepsilon_p \hat{\mathbf{a}}, \tag{7}$$

where $k_0^2\delta\varepsilon_p = \left(4\pi q^2/mc^2\right)\langle n_e/\gamma\rangle$, where we have introduced the brackets to represent cycle averaged quantities.

We will not describe in detail the kinetic model of the plasma used. Rather, we will present only the background necessary to provide details for how the laser is coupled to the plasma simulation within the appropriate approximation. Further details for the plasma model and numerical realization can be found in Mora and Antonsen [39] and Huang et. al. [77].

The model for the plasma is based on two approximations. First, the effect of the laser on the plasma electrons is treated with the ponderomotive approximation. In this approximation, the effect of the high-frequency laser pulse is averaged over one cycle and only the gradient of the pulse envelope is needed to evolve the plasma particles. This approximation is valid provided the transverse displacement of a plasma electron is small compared to the transverse length scale of the laser pulse. The validity of this approximation has been established for high laser amplitudes, provided the focal spot size of the laser is large compared to the laser wavelength [78].

The second approximation is to treat the plasma electrons quasi-statically. This approximation requires the time scale for laser envelope evolution be much greater then the time required for a plasma electron to transit past the laser pulse, in the speed of light frame. The essential consequence of this approximation is that plasma electrons must have an axial velocity much smaller then the speed of light. Therefore, no treatment for acceleration of background plasma electrons is possible. However, one benefit of the plasma code we are using is that a relativistic beam of electrons for which the quasi-static approximation does not apply can be present and is treated separately from the plasma electrons. This additional beam will allow investigation of acceleration mechanisms for electron bunches which are injected into the plasma, thus removing a significant limitation of the quasi-static approximation.

Now we must evaluate the equations of motion for an electron under the influence of both the laser field and any plasma waves that exist in the perturbed plasma. Details of the derivation of these equations are presented by Mora and

Antonsen [39] and will not be duplicated here. We note that in the ponderomotive approximation we can separate the electron motion into a high frequency response, which follows the laser frequency ω_0, and a low frequency response, which describes the plasma wave. Then the low frequency equation of motion for the plasma electron is

$$\frac{d\overline{\mathbf{p}}}{dt} = q\left(\overline{\mathbf{E}} + \frac{\overline{\mathbf{v}}}{c} \times \overline{\mathbf{B}}\right) - \frac{q^2}{2\bar{\gamma}mc^2}\overline{\nabla\left|\mathbf{A}_{laser}\right|^2} \tag{8}$$

where $\overline{\mathbf{E}}$ and $\overline{\mathbf{B}}$ are the fields associated with the plasma wave and a relativistic electron beam, if present, and $\bar{\gamma}^2 = 1 + \left[\overline{\mathbf{p}}^2 + 2\overline{\left|q\mathbf{A}_{laser}/c\right|^2}\right]/m^2c^2$. We have also introduced the over-bar to represent the low frequency response or the cycled averaged response in the case to the laser field. Within the quasi-static approximation only the transverse components of Eq. (8) need to be evolved, while the axial motion can be evaluated using the constancy of a combination of the low frequency Hamiltonian for the system and the axial canonical momentum, $\overline{H} - c\overline{P}_z = \bar{\gamma}mc^2 - c\bar{p}_z + q\bar{\phi} - q\overline{A}_z = mc^2$, see ref [39] Eqs. (8) and (9). Here $\overline{A}_z$ is the axial component of the vector potential and $\bar{\phi}$ is the scalar potential of the plasma wake associated with $\overline{\mathbf{E}}$ and $\overline{\mathbf{B}}$ in Eq. (8) above and $\overline{P}_z = \bar{p}_z + q\overline{A}_z / c$. Introducing the auxiliary field $\overline{\psi} = \bar{\phi} - \overline{A}_z$ we can update the transverse position and momentum of the particles by

$$\frac{d\mathbf{x}_\perp}{d\xi} = \frac{\overline{\mathbf{p}}_\perp}{mc(1 - q\overline{\psi}/mc^2)}, \tag{9a}$$

$$\frac{d\overline{\mathbf{p}}_\perp}{d\xi} = \frac{1}{c(1 - q\overline{\psi}/mc^2)}\left[q\bar{\gamma}\left(\overline{\mathbf{E}} + \frac{\overline{\mathbf{v}}}{c} \times \overline{\mathbf{B}}\right)_\perp - \frac{q^2}{mc^2}\nabla_\perp\left|\overline{\mathbf{A}}_{laser}\right|_\perp^2\right]. \tag{9b}$$

To capture the relativistic effects on the dielectric susceptibility of the plasma it is necessary that the plasma density be modified by the appropriate weight. The dielectric of the plasma is given by the oscillating component of the current density, which in turn is related to the oscillating component of the individual electron momentum. Therefore, the dielectric response of the plasma appropriate for including relativistic effects is $k_0^2 \delta\varepsilon_p = -k_p^2 \sum_i \langle n_{ei} / \gamma_i n_0 \rangle$, where i ranges over each particle and the appropriate density and relativistic factor are included.

Now we examine the plasma behavior in the presence of the ponderomotive potential. For the case of a one-dimensional laser field, an analytic expression for the amplitude of the resulting plasma wake electric field can be derived [23]. The wake amplitude is given by $\bar{\phi}(\xi) = \int_0^{\xi} |\hat{\mathbf{a}}|^2 \sin(\xi - \xi') d\xi'$, where we have assumed $\hat{\mathbf{a}}$ has a polynomial profile in ξ. This expression is valid for pseudo one-dimensional simulations and for moderately non-linear response. Figure 3 shows the axial electric field, $\partial\bar{\phi}/\partial\xi$, for a plasma response to a laser field with $\hat{\mathbf{a}}_{\max} = 1.0$. Results of simulations both from this code and OSIRIS[62] are presented. The results from the analytic calculations are also presented in figure 7. These benchmarks and tests demonstrate that both the model and the numerical implementation we have presented are accurate for the plasma response to the ponderomotive potential.

Conclusions and Future Work

We have presented a new numerical scheme for solving Eq. (2) accurately and efficiently in parallel. This realization can either be coupled to an existing kinetic plasma model using the ponderomotive approximation to the equations of motion or a

neutral gas model with ionization. We have presented results of benchmarks, which confirm the accuracy and validity of the model and implementation.

We have also presented results of modeling of fully ionized plasma response using a kinetic electron description. This model for the plasma utilizes a particle-in-cell scheme for advancing the plasma electrons; however, the quasi-static approximation for the plasma response is also used. This model for the kinetic plasma also includes a relativistic electron bunch, which will be used to model injection of electrons into a LWFA.

This code represents an improvement in the capability to model long-term evolution of laser pulses with high intensity and short duration. This improvement is due to the much longer time steps allowed by the approximations applied. Future effort will be expended in performing modeling of advanced accelerator concepts and extending this code to include effects of ionizing gas.

Figures

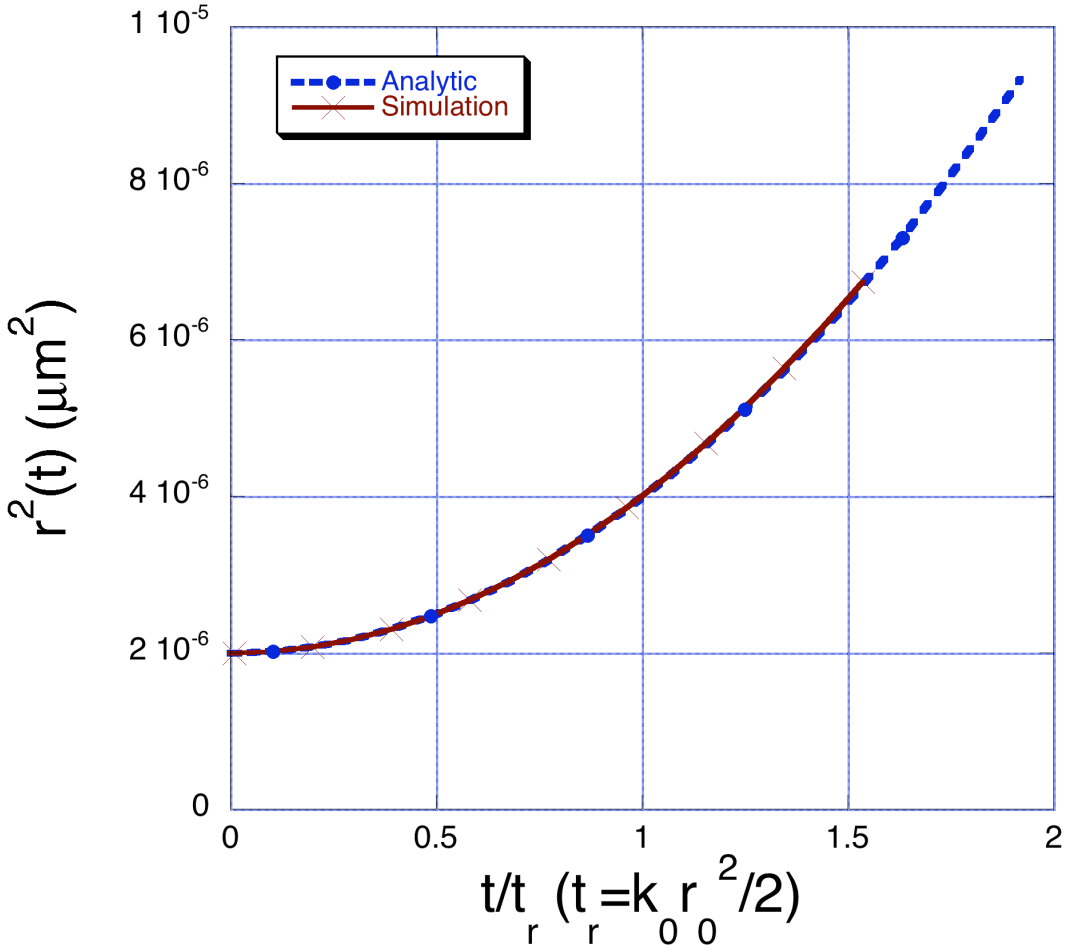

Figure 1. Plot of the average radius squared, $r^2 = \int \left(x^2 + y^2\right) |\hat{\mathbf{a}}|^2 \, dxdyd\xi / U_{total}$, where $\hat{\mathbf{a}} = a_0 \exp\left(-r^2 / 2r_0^2\right)$, for both the simulation result at low power and the analytic value $r^2 = r_0^2 \left(1 + \left(z / Z_r\right)^2\right)$ as a function of normalized propagation distance z / Z_r where $Z_r = k_0 r_0^2 / 2$. Here, U_{total} is the total energy in the laser pulse and $|\hat{\mathbf{a}}|^2$ is the normalized envelope of the laser vector potential.

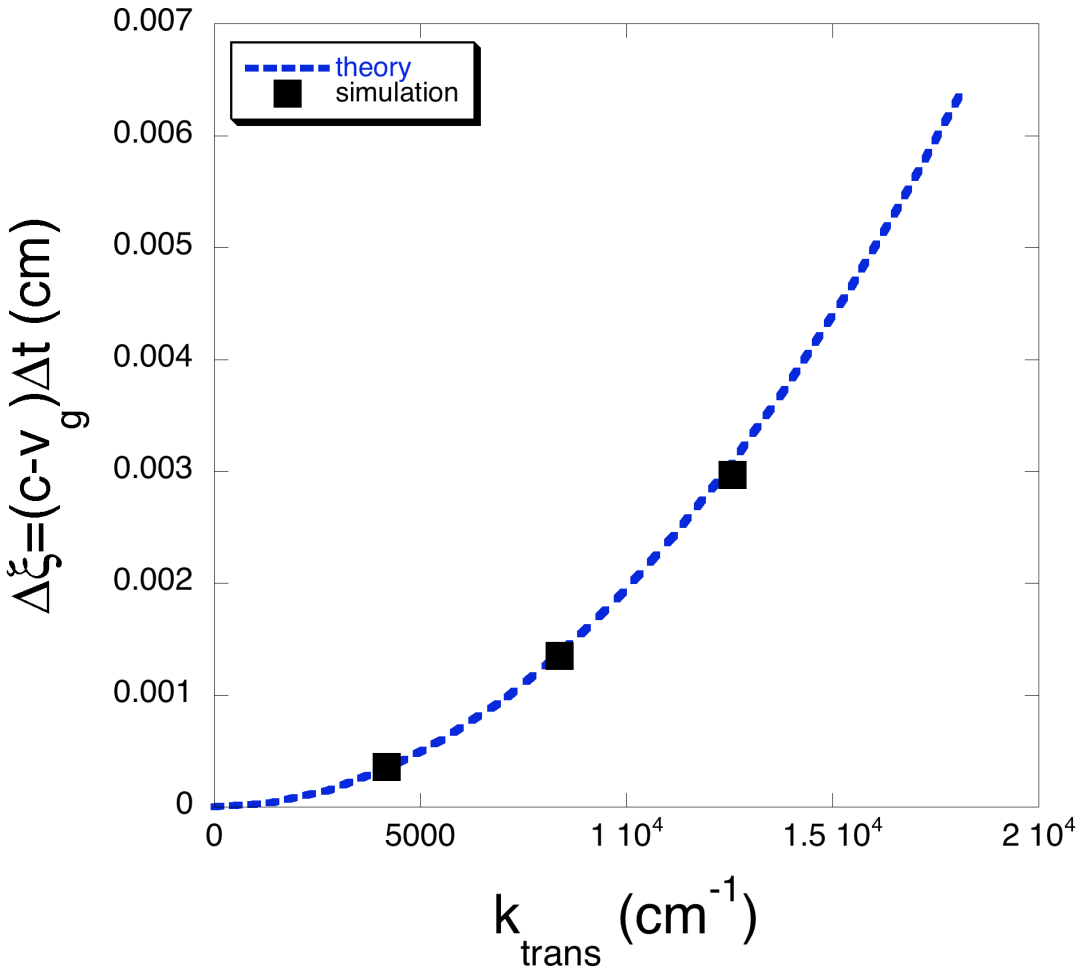

Figure 2. Effects of transverse wavenumber on laser pulse propagation velocity in the z-direction. Laser group velocity in vacuum is given by $v_g \simeq c(1-k_\perp^2/2k_0^2)$. The dashed line represents the analytic estimate for the distance the laser pulse with transverse mode $k_\perp$ will slip in $\Delta t=8\text{x}10^{-12}$ sec of pulse propagation. The squares are the values calculated based on simulations for several different transverse modes.

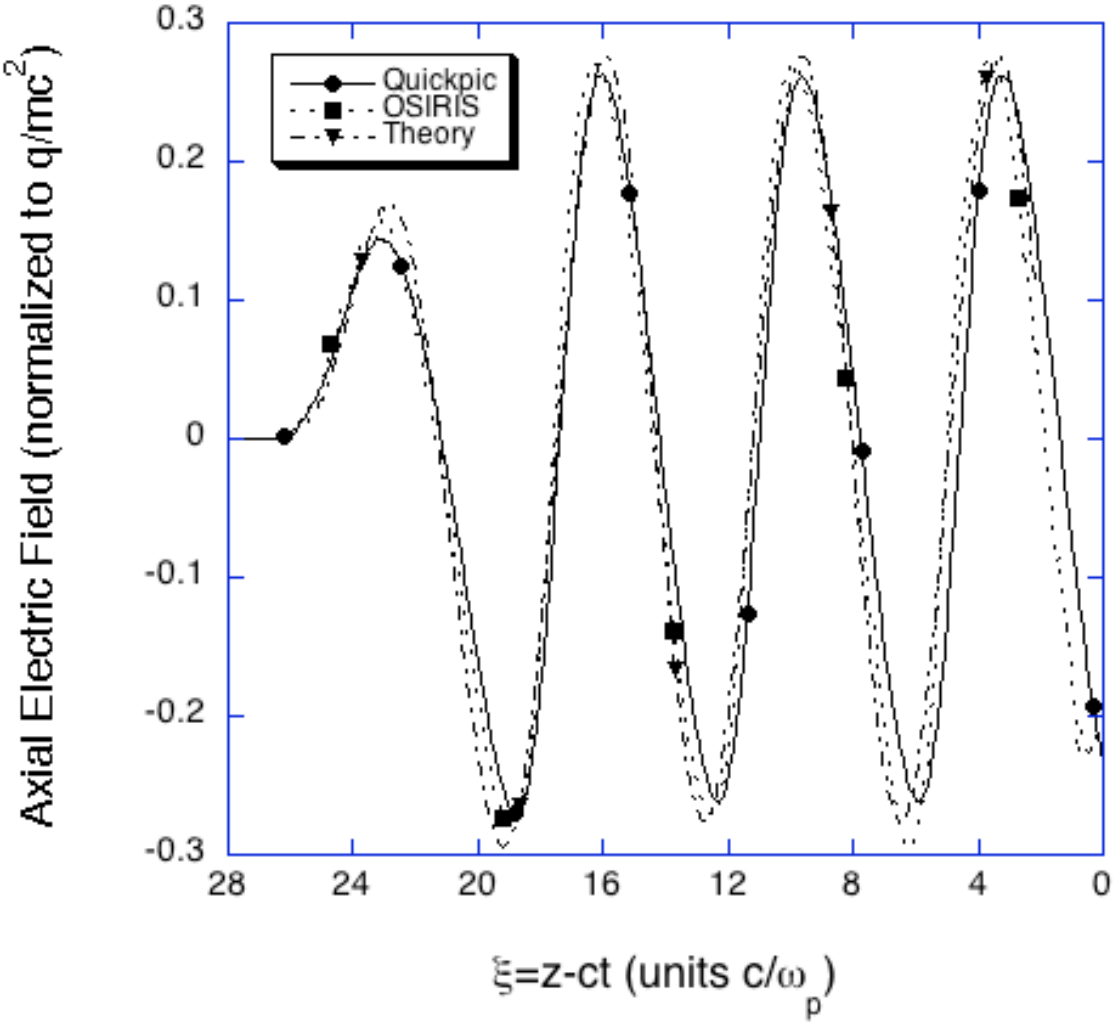

Figure 7. Plotted is the axial electric field in the plasma wave due to interaction with a high intensity laser. This simulation has $\hat{\mathbf{a}}_{\max} = 1.0$, laser wavelength $\lambda = 0.8\mu m$, laser pulse duration $\tau_l = 100\, fs$, and $r_0 = 100\mu m$. The solid line is from the kinetic plasma response to the laser ponderomotive potential discussed in this chapter. The dotted line is from a comparable run using the code OSIRIS. Also included is the one-dimensional analytic response [23].

Chapter 4: Modeling and Simulations of Laser Pulse Evolution in Ionizing Gas

Background

Advances in laser technology over the past decade, in particular chirped-pulse amplification (CPA)[6], have made experimental systems with high peak-power laser pulses inexpensive and thus widely available. These laser systems typically have laser wavelengths of approximately 1 μm and pulse durations of tens to hundreds of femto-seconds (fs), 10^{-15} sec. Although the peak laser power can be several terra-watts (TW), e.g., 10^{12} W, with peak intensities of 10^{19} W/cm^2 the total energy of the laser pulse may be limited to a few hundred milli-joules (mJ). However, laser pulses with these intensities and peak-powers exhibit new and interesting phenomena. For instance, at a laser pulse power of a few giga-watts (GW), 10^9 W, a laser pulse propagating through neutral gas will undergo self-focusing due to the polarizability of the neutral atoms and molecules[25,27]. This effect occurs due to the increase in the local index of refraction of the gas in the region of high field intensity, near the optical axis, which then leads to a local decrease in the phase-velocity of the laser pulse. This results in the laser pulse focusing onto the optical axis due to a self-induced modification to the gas index of refraction; self-focusing.

At local laser intensities of around 10^{14} W/cm^2, the neutral gas can undergo ionization, which results in a contribution to the local index of refraction due to the free-electron density. This plasma will lead to refraction of the laser pulse. However, in the presence of neutral gas self-focusing, the laser pulse may still have regions outside the plasma that induce self-focusing. This competition between neutral gas

induced self-focusing and free-electron induced refraction may lead to a regime of pulse propagation known as off-axis guiding[27]. In this regime, the local index of refraction has a maximum at some radial location that is not on the optical axis. Thus the laser pulse is essentially guided in this region, prevented from further focusing on the optical axis by the local plasma density and prevented from diffracting due to the neutral gas polarizability.

As the rate and degree of ionization increase an additional phenomena occurs due to the coupling of the main laser pulse with scattered waves that have small transverse components to their wave number[28]. This coupling results from the strong dependence on the local field magnitude of the ionization rate and results in the introduction of small transverse structure in the free electron density. This transverse structure in the free electron density enhances scattering of the laser pulse into the transverse modes and thus may lead to a parametric type instability.

The remainder of this chapter will present results of three-dimensional simulations that demonstrate the robustness of the model and numerical scheme, discussed in chapter 3, for laser pulse propagation in ionizing gas for a range of conditions. We start by describing the model for the laser and the matter dielectric response used in this investigation. Then we begin by examining laser pulse self-focusing and off-axis guiding and comparing to results of simulations using the two-dimensional simulation code WAKE[39]. We will then present simulation results for the ionization scattering instability and compare to previous two-dimensional results[28]. The three-dimensional structure of this instability will then be discussed

and compared to experimental results. Finally, we will conclude with a discussion of future work in studying the ionization scattering instability.

Model

The laser pulse is modeled in terms of Maxwell's equations for the electro-magnetic vector potential and is given by

$$\left(\frac{1}{c^2}\frac{\partial^2}{\partial t^2}-\nabla^2\right)\mathbf{A}_{\mathbf{laser}}=\frac{4\pi}{c}\mathbf{J}+\frac{4\pi}{c}\frac{\partial}{\partial t}\mathbf{P}, \tag{1}$$

where **J** is the free electron current density, **P** is the polarizability of the neutral gas and c is the speed of light in vacuum. We chose to work in the frame traveling with the laser pulse and define $\xi = v_f\tau - z$, $\tau = t$, where v_f is the frame velocity. If we assume the laser pulse can be represented as a plane wave with phase given by $k_0\xi = \omega_0 v_f t / c - k_0 z$ modified by a slowly varying envelope then the laser pulse is represented by $\mathbf{A}_{laser} = \hat{\mathbf{A}}_{laser}(\tau,\xi,x,y)\exp(ik_0\xi) + c.c.$ where $\hat{\mathbf{A}}_{laser}$ is a complex amplitude and is assumed to depend slowly on τ. Introducing a laser pulse envelope that is normalized according to $\hat{\mathbf{a}} = q\hat{\mathbf{A}}_{laser} / mc^2$ we can arrive at the following equation for the envelope of the laser pulse

$$\begin{aligned}&\frac{2}{c}\frac{\partial}{\partial\tau}\left(ik_0-\frac{\partial}{\partial\xi}\right)\hat{\mathbf{a}}+ik_0(\beta_1-\delta\varepsilon_0)\frac{\partial}{\partial\xi}\hat{\mathbf{a}}-\beta_2\frac{\partial^2}{\partial\xi^2}\hat{\mathbf{a}}+\nabla_\perp^2\hat{\mathbf{a}}\\&=-k_0^2\delta\varepsilon\hat{\mathbf{a}}.\end{aligned} \tag{2}$$

Here the second time derivative has been neglected under the assumption of a slowly varying envelope. The terms involving β_1 and β_2 account for the linear contribution in the dielectric function δε due to the polarizability of the neutral gas. We have

$\beta_1 - \delta\varepsilon_0 = 2(v_f - v_g)/c$,

$\beta_2 = v_f^2/c^2 - 1 + \delta\varepsilon_0 + 2\omega_0 \partial\delta\varepsilon_0/\partial\omega\big|_{\omega=\omega_0} - (1/2)\omega_0^2 \partial^2\delta\varepsilon_0/\partial\omega^2\big|_{\omega=\omega_0}$ and $\delta\varepsilon_0$ is the linear dielectric response. The non-linear effects in the dielectric due to neutral gas as well as the effects due to free electrons are contained in $\delta\varepsilon$. If we choose the simulation frame to correspond to the laser pulse group velocity given by $v_g = d\omega/dk$ then the term involving β_1 is zero identically.

The model of the dielectric response can be chosen based on the particular physics that needs to be simulated. For the current work, we chose the dielectric to include effects due to free electrons resulting from the ionization of neutral gas and self-focusing due to the electronic polarizability of the gas. Within this model we obtain

$$\delta\varepsilon = -\frac{k_p^2}{k_0^2}\frac{n_e}{n_0} + 2\frac{p_g}{760}n_2 I \,, \tag{3}$$

where p_g is the gas pressure in torr, $n_2 = 2.275x10^{-20} cm^2/W$ represents the instantaneous modification of the electronic response of the gas, Helium, to the applied laser intensity I(W/cm^2), the Kerr effect. The plasma term is $k_p^2 = 4\pi q^2 n_0/m_e c^2$ and n_e is given by ionization rate equations $\partial n_e/\partial\xi = \sum_i \nu_i(|a|) n_i$ and $\partial n_i/\partial\xi = \nu_{i-1}(|a|) n_{i-1} - \nu_i(|a|) n_i$, $\nu_i(|a|)$ are tunneling like ionization rates. We have neglected collisional ionization and recombination under the assumption that these processes occur on a much longer time scale then we are interested, e.g. 10^{-12} sec compared to 10^{-14} sec. The model for the ionization rate includes both multi-photon and tunneling ionization and is valid provided there are no resonant transitions

near the laser optical frequency, which is the case for the present calculations. Under these assumptions the ionization rate is given by

$$\nu(|a|) = \begin{cases} 0, |\varphi| < \varphi_{\min}, \\ \nu_{0i} |\varphi|^{\beta}, \varphi_{\min} < \varphi < \varphi_{tunnel}, \\ \nu_{0i} \exp(-1/\varphi), \varphi_{tunnel} < \varphi, \end{cases} \tag{4}$$

where $\beta = 7.5$ is the order of the process, $\varphi = \left(|a|^{3/2} / a_h^{3/2}\right)\left(13.6/\chi_i\right)^{3/2}$ and $\varphi_{\text{tunnel}} = 0.04209$ is chosen to smoothly transition from the multi-photon to the tunneling regime, $a_h = r_e \lambda / 4\pi a_0^2$ is the normalized vector potential for the hydrogen atom, and r_e and a_0 are the classical electron radius and Bohr radius respectively and χ_i is the binding energy for the i$^{\text{th}}$ electron. Further, the ionization rate coefficient is given by

$$\nu_{oi} = \sqrt{\frac{3}{\pi}} \frac{\alpha}{a_0} \left(n_g - n_i\right) \left(\frac{\chi_i}{13.6}\right)^{1/4} \left[2\left(\frac{\chi_i}{13.6}\right)^{3/2}\right]^{2n^* - 1} \left(\frac{a_h}{a}\right)^{2n^* - 1.5},$$

where $\alpha \approx 1/137$ is the fine structure constant n_g is the total number of electrons in the atomic shell of the atom, n_i is the total number of remaining electrons in the atomic shell and $n^* = n_i / \sqrt{\chi_i / 13.6}$.

Figure 1 shows a comparison for the ionization rate for helium between the fluid version of WAKE[27] and this code. The double step in the ionization process is clearly visible and the threshold for the ionization for each electron is identical in each code. This result is not surprising since the ionization models used in WAKE and this code are identical; however, it does provide an important benchmark for the results to be discussed in the remainder of this chapter.

Results

In this chapter we will investigate three specific physical phenomena and compare the results of the three-dimensional model with results from a two-dimensional code WAKE[27,39]. The phenomena are 1) off-axis guiding, 2) self-focusing and filamentation in ionizing gas, and 3) ionization scattering instability. The first and second phenomena occur at laser powers from $1x10^{11}$ - $2x10^{12}$ W but with peak intensities of less then $1x10^{15}$ W/cm^2. In this range, the laser pulse is above the critical power for self-focusing $P_{cr} = \lambda^2 / 2\pi n_0 n_2 \simeq 5x10^9$ for a gaussian pulse [27] and has an intensity high enough to cause ionization but not high enough that the ionization physics dominates over the laser pulse dynamics due to the dielectric response of the gas. These two phenomena that have been previously identified; however, we can use them to demonstrate capabilities of this new code for three-dimensional simulations.

Before we begin exploring the specific phenomena we will investigate a simplified situation in which we eliminate plasma generation due to ionization and explore the effect of self-focusing on the laser pulse with no additional material response. In this case, we have $\delta\varepsilon = 2(p_g / 760)n_2 I$. We chose our simulation pressure to be 141 torr He, which yields a critical power for self-focusing of $2.4x10^{11}$ W. We have turned the ionization processes off and use a laser spot size $r_0 = 27.6\mu m$, which gives a Rayleigh length of $Z_r = 2.99mm$. We will simulate two laser pulses with peak power $1.1x10^{12}$ W, slightly over $4P_{cr}$.

Figure 2a shows a two-dimensional slice of the laser pulse mid-plane at the start of the simulation. The simulation is initialized at the vacuum focus, so all-additional increase in the laser pulse magnitude is due to the non-linear Kerr self-focusing. Figure 2b shows a slice of the laser pulse transverse to the direction of propagation in the middle of the pulse after 180μm propagation distance. It is clear that the cylindrical symmetry is still maintained. However, the laser pulse peak magnitude is increasing, 0.018 compared to 0.011 initially. This increase is consistent with the expected self-focusing process. Figure 3 shows the same laser pulse conditions as Figure 2b, except that the laser pulse was initialized with noise equal to one percent of the main pulse magnitude in the direction transverse to propagation. Notice in this case that there are clearly three distinct filaments. This result implies that each filament contains slightly over the power necessary for self-focusing.

Now we turn to the phenomena, which include ionization physics. The first phenomena, identified by Wu[27], involves off-axis guiding which requires a balancing between the self-focusing due to the neutral gas and the linear refraction due to the free electron density. Off-axis guiding can lead to the propagation over long distances of a laser with significant field intensity off the optical axis. Figure 4 shows an example of this phenomena demonstrated using this code. This example is for a laser vacuum spot size of 0.178 mm and a laser peak power 4.5×10^{11} W, $\sim 2P_{cr}$. Figure 4a is the laser pulse at the start of the simulation and also at the location of the vacuum focal plane. This location should correspond to the location of peak intensity, after this point in vacuum the laser should diffract. Notice that in Figure 4b

there is a region at the front of the pulse that is focused onto the optical axis and this is where ionization occurs. Behind this region the laser intensity maximizes off the optical axis. Figure 4c shows the laser pulse after 10.5 cm propagation in 141 torr Helium, notice that only a single set of lobs exist off the optical axis. Figure 4d, shows the laser pulse after 16.5 cm. At this point the off-axis lobs are converging on the optical axis. At this point the off-axis guiding structure is vanishing.

In figure 5 we examine the laser and dielectric response for a laser pulse undergoing off-axis guiding. Figure 5b shows the dielectric response, $\delta\varepsilon$, for the material at the point in the simulation as figure 5a. Notice that there are several location of local minima in the dielectric function, which causes the laser pulse to be guided at several radial locations. However, if we include random noise in the direction transverse to the laser propagation direction the symmetry is broken. This effect is clearly visible in figures 5c and 5d. In Figure 5c, we see the mid-plane of the laser pulse after 2.7mm propagation distance. The laser pulse was identical to the one shown in figure 5a except that noise with magnitude one percent the main pulse magnitude was included. Figure 5d shows a plane cut transverse to the propagation direction at approximately 0.0115 cm in the laser pulse frame. There appears to be some cylindrical symmetry remaining; however, local regions of higher laser intensity have appeared.

At higher powers a second phenomena can occur which involves the production of electro-magnetic radiation propagating radially outward with a transverse wave number approximately equal to the plasma wave number. This transverse scattered light is different then that associated with the ionization

scattering instability to be discussed below and appears due the transmission of light from the plasma in the central region to the neutral gas. The frequency for the laser pulse prior to ionization is ω_0 with wave number $k_0 = \omega_0 / c$ however, after ionization, which occurs rapidly, the laser frequency is up-shifted to satisfy the local dispersion relation and we have $\omega' = \sqrt{c^2 k_0^2 + \omega_p^2}$. As the pulse diffracts out of the central region with the plasma the laser frequency and axial wave number do not change, however the pulse will acquire a transverse wave number to satisfy the new local dispersion relation, $c^2 k_\perp^2 = \omega'^2 - c^2 k_0^2 = \omega_p^2$. Figure 6 shows an example of this phenomenon for a laser peak power of $15P_{cr}$ propagating in 141 torr Helium.

One additional phenomenon we wish to investigate to test this new propagation code is the filamentation of the laser pulse due to self-focusing in an ionizing gas. Self-focused pulses are unstable to transverse perturbations of the field. These transverse perturbations lead to laser filamentation with each filament having approximately the critical power required to self-focus. Figure 7 shows the results for a simulation with initial peak power $5P_{cr} \simeq 1.2x10^{12} W$ in 141 torr uniform background Helium undergoing ionization. In figure 7a we have an initial rotationally symmetric laser pulse and the field maintains this rotational symmetry; however, in figure 7b we have imposed a transverse perturbation with one percent maximum amplitude onto the initial field. Notice the field no longer presents a transversely uniform structure, but rather has been disrupted into several distinct filaments. Figure 8 clearly shows the filamentation of the laser pulse into approximately 5 filaments at 0.0120 cm in the pulse frame after 3 cm of pulse propagation.

Finally, the third phenomenon we wish to explore involves laser intensities around $1\text{x}10^{16}$ W/cm^2. In this range the neutral gas is fully ionized and further, this ionization happens rapidly in the laser frame. This ionization can lead to unstable growth of scattered modes due to the coupling of the laser pulse and the scattered modes through the field dependent ionization rate[28]. This coupling can lead to transverse perturbations in the electron density that can enhance scattering of the main laser pulse resulting in parametric type instability.

Bian and Antonsen [28] derived a local dispersion relation for the growth of the scattered modes and found that the instability could be described by

$$D\left(k_z,k_\xi\right)=\frac{\bar{\nu}_0}{c}-ik_\xi+k_1k_p^2\times\left[\frac{1}{k_\perp^2+2k_z\left(k_\xi+k_0\right)}+\frac{1}{k_\perp^2+2k_z\left(k_\xi-k_0\right)}\right]$$

where, $\bar{\nu}_0$ is the cycle averaged ionization rate for the gas and $k_1=\left(\left|E_0\right|/2c\right)\left(1-n_0/n_g\right)\partial\bar{\nu}_0/\partial\left|E_0\right|$. Here E_0 is the electric field of the primary pulse and n_0 and n_g represent the electron density due to the pump laser and the gas density respectively. The quantities k_z and k_ξ represent the wave number in the propagation direction with respect to the lab (z) and pulse (ξ) coordinates and $k_\perp$ is the transverse wavenumber for the scattered mode. The wavenumber k_ξ gives the frequency shift of the scattered waves. If $k_\xi \ll k_0$ then this dispersion relation can be written in terms of a quadratic for the laser wavenumber k_z as $k_z=\pm\left(1/2k_0\right)\sqrt{k_\perp^4+2k_\perp^2k_1k_p^2/\left(\bar{\nu}_0/c-ik_\xi\right)}$. Unstable growth requires that $\text{Im}\left(k_z\right)<0$ which is only possible with $k_\xi\neq 0$ since $k_1>0$ if the ionization rate

increases with increased laser intensity. This instability can be characterized by two parameters, $k_\perp$ and k_ξ.

We begin the study of the ionization scattering instability by examining the propagation of a plane wave with peak intensity of $1x10^{16}$ W/cm^2 and pulse duration of 140 fs FWHM in helium gas with pressure 141 torr. This intensity was chosen to provide doubly ionized helium, which at this pressure will result in an electron density of $1x10^{19}$ cm^{-3}. In addition to the plane wave we include transverse modes in the range $0.2k_p$ to $4.7k_p$ with random amplitude around $1x10^{-5}$ of the plane wave and with random relative phase.

The transverse size of the simulation box was 45 μm, which is approximately 4.5 plasma wavelengths across, and has 128 grid points in each of the two transverse directions. The axial extent of the simulation box is 350 μm with 300 grid points. This grid and domain provides good resolution for all scattered modes that grow. The time step was chosen to be $4x10^{-15}$ sec to ensure that the growth time of the unstable modes was well resolved. Figure 9 shows a two-dimensional slice of the initial plane wave and the pulse after 1.9 mm of propagation. The unstable transverse modes have clearly grown in the front of the laser pulse, where the ionization process is happening. Figure 10 shows a line out for the laser pulse in figure 9 along with the electron density. The specific locations that correspond to unstable growth are clearly coincident with the regions of rapid ionization.

Figure 11a shows the Fourier space of the initial transverse seed of the simulation and figure 10b shows the maximum, in ξ, ratio, $\delta a_k / \delta a_{k,0}$, of the Fourier modes at the same propagation distance shown in figure 8b, 1.9 mm. We can clearly

see that the modes with small transverse mode do not grow, consistent with the local dispersion relation described in ref[28]. Notice also that the scattered modes with wavenumbers well above the plasma wave k_p do not have significant growth. This low growth can be understood since these modes will have a significant transverse wavenumber and thus will drift backward in the laser pulse frame out of the region of high ionization. Thus this instability is convective in the laser pulse frame, which suppresses growth for the larger wavenumber modes. The modes that correspond to the fastest growth have a transverse wave number approximately $1.5k_p$, which is slightly larger then previous results indicated[28].

We must also examine the frequency shift for the growing modes. Figure 12 shows the initial and final frequency spectrum for the plane wave propagating through 1.9 mm of 141 torr Helium gas. Notice for the transverse mode with the largest growth $k_\perp = 0.1x10^4\left(3\mathbf{e}_x + 7\mathbf{e}_y\right)\text{cm}^{-1}$, where $\mathbf{e_x}$ and $\mathbf{e}_y$ are unit vector in the x and y direction in Fourier space. The scattered light is blue shifted and the amount of blue shift corresponds the scale length of the steep part of the ionization curve shown in figure 10, $\sim 2\pi / \Delta\xi$. This result agrees well with the expected value based on the dispersion relation derived in ref[28].

We have also examined the propagation of a gaussian laser pulse into a gas jet target. We assume the laser vacuum spot size is 43 μm and the gas jet target will provide an electron density of $1x10^{19}$ cm^{-3} when fully ionized; 141 torr Helium. The mid-plane slice, for the initial laser pulse and after 3.5 mm of propagation, is shown in Fig. 13. We see in Fig. 13b, after propagating in the gas jet, that the front of the laser pulse is focused on the optical axis while the remainder of the pulse is refracted

and filamented. Figures 14 and 15 show the transverse structure for the laser pulse at the same location within the pulse for both the initial pulse and after 3.5 mm propagation. Figure 14 is the magnitude of the laser pulse in real space, while Fig. 15 is the transverse Fourier space at this same location within the pulse. In Fig. 14b, we see what appears to be off-axis guiding causing several rings in the laser pulse. In Fig. 15b, this ring structure persists in the Fourier space. The wavenumber of the Fourier modes is lower then what would be expected for doubly ionized Helium at this pressure, k_p=5945 cm^{-1}. This difference may be due to the fact that for a gaussian pulse the radially outer regions of the pulse do not get doubly ionized. If the instability grows in regions of singly ionized Helium at these conditions then the expected wavenumber would be 4200 cm^{-1}, which is closer to the location of the rings.

Figure 16 shows the plasma electron density left after the pulse has propagated through the gas jet. The pulse enters from the left in this figure and has the location of vacuum focus at z=0. Figure 16a shows the electron density for the pulse entering a gas jet at 141 torr Helium peak pressure, centered at the focal spot. Figure 16b is for the same laser pulse but focused into 282 torr Helium jet. Notice that a significant amount of ionization occurs in the outer radial location of the laser pulse resulting in lower electron density, thus it is not surprising that the transverse wave number is somewhat lower then would be expected for the doubly ionized case. Also notice that the amount of forward scattered energy, and thus electron density, is higher for the higher density case. This result is qualitatively similar with experimental results for this instability, shown in figure 17 [82]. Further analysis will

be necessary to fully characterize this instability in three-dimensions and to provide a complete analysis of the experimental data.

Conclusions

We have presented a series of simulations that demonstrate the capabilities of this new code to capture relevant physics and accurately model pulse propagation in a several different regimes. The results indicate good agreement with previous results in regions where the two-dimensional characteristics are valid. Further, these results indicate that many of the phenomena discussed have three-dimensional characteristics that must be included in order to accurately model experiments. In particular, the filamentation due to ionization scattering instability is not expected to be azimuthally symmetric however, side probe experiments used to diagnose this phenomena only provides a single orientation. Therefore, good agreement with simulation results requires the ability to account for the asymmetry in the process. This code will provide many new capabilities to extend our understanding and access to experimental validation in the future.

Figures

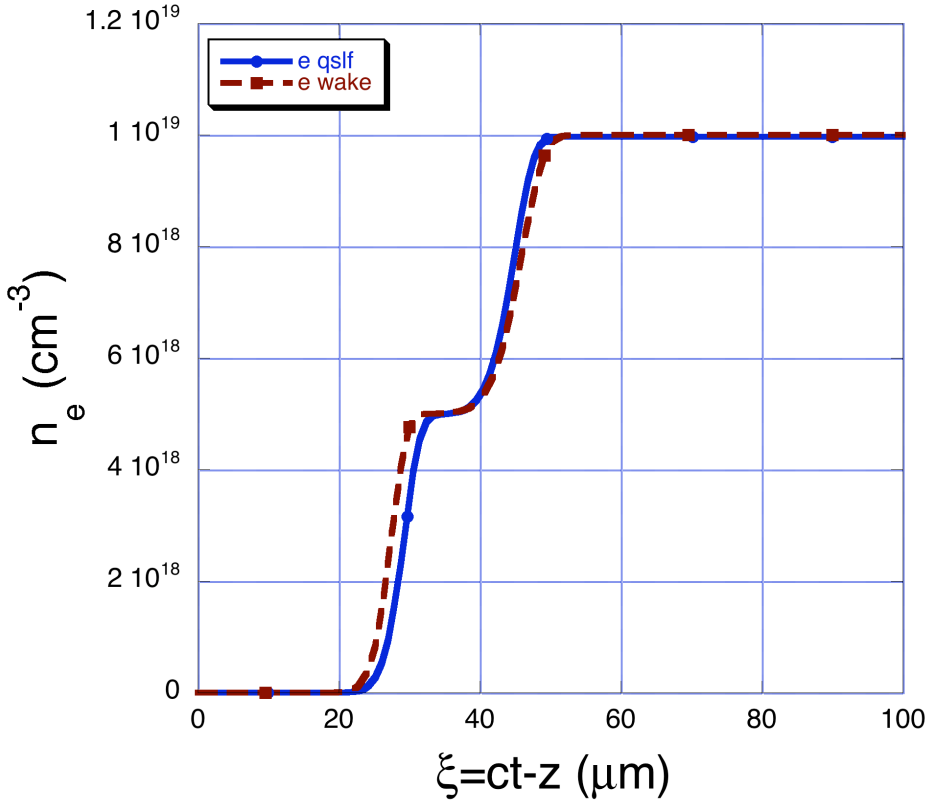

Figure 1. Comparison for on axis ionization rate for Hydrogen between WAKE and our new three-dimensional code. Notice the double stair-step structure characteristic of Helium ionization. These codes yield that same results for ionization, which is not surprising given they both use the same ionization model. However, this confirmation lends support to the results in the remainder of this chapter.

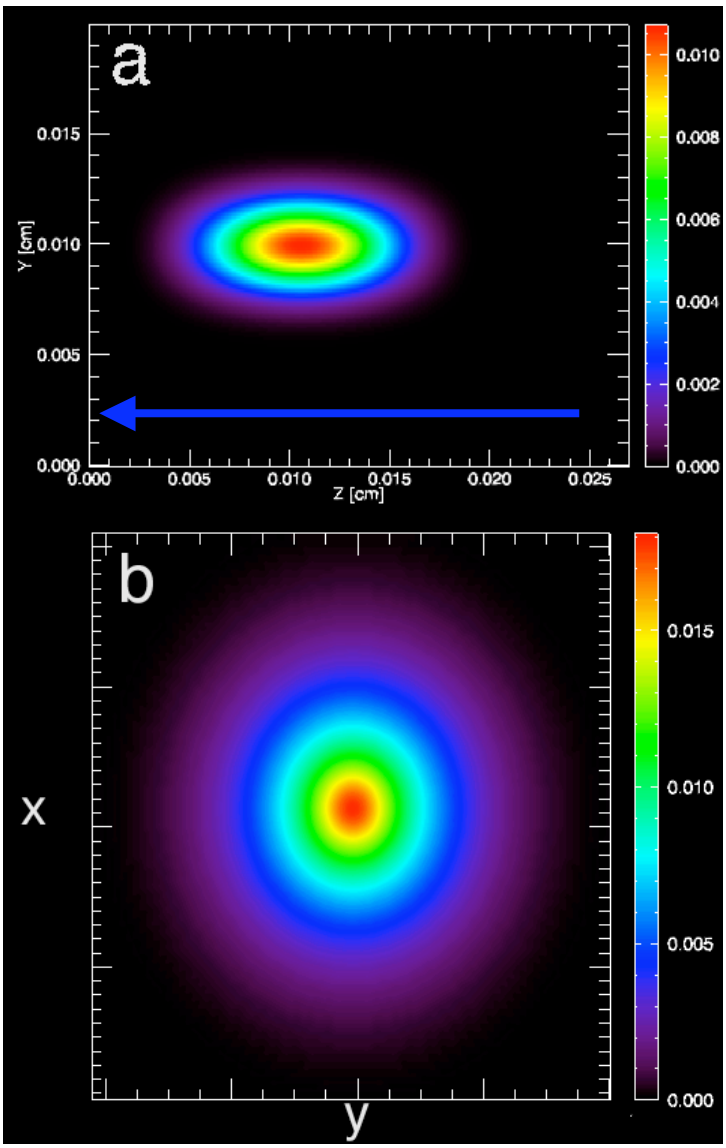

Figure 2. a) mid-plane slice of laser pulse at start of the simulation. The simulation was started at the vacuum focus. Notice the peak pulse magnitude is slightly over 0.010. b) Slice of the laser pulse transverse to the propagation direction after 180mm propagation. Notice that the cylindrical symmetry is still maintained. However, the peak pulse magnitude is nearly 0.020, larger then the magnitude at the vacuum focus. This is consistent with a laser pulse undergoing self-focusing.

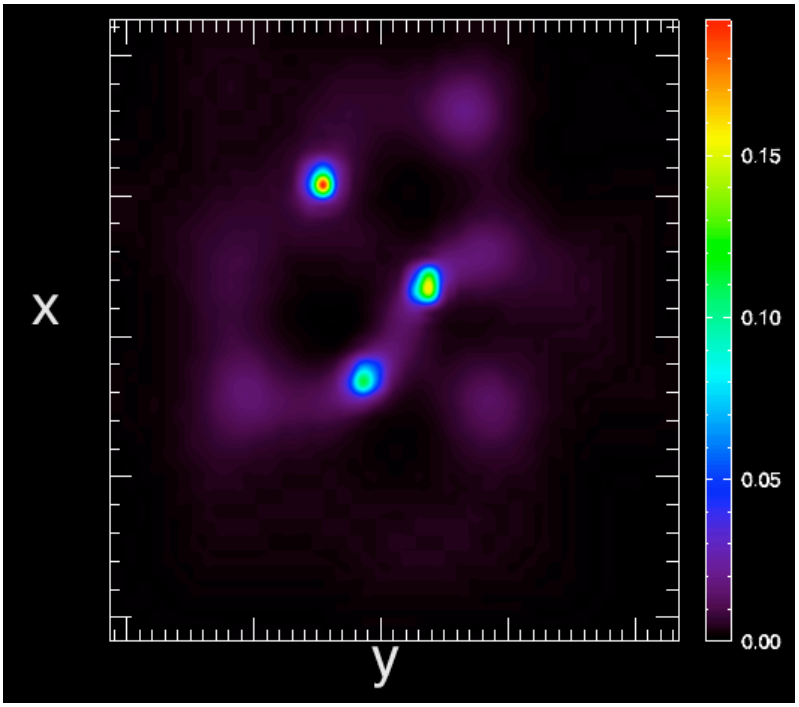

Figure 3 Slice of the laser pulse transverse to the propagation direction after 180μm propagation. This laser pulse is identical to the one shown in Figure 2, except that the pulse was initialized with noise with magnitude equal to one percent of the main pulse magnitude in the direction transverse to the propagation direction. Notice that the cylindrical symmetry is broken and three filaments have formed. This laser pulse had an initial power that was slightly above $4P_{cr}$.

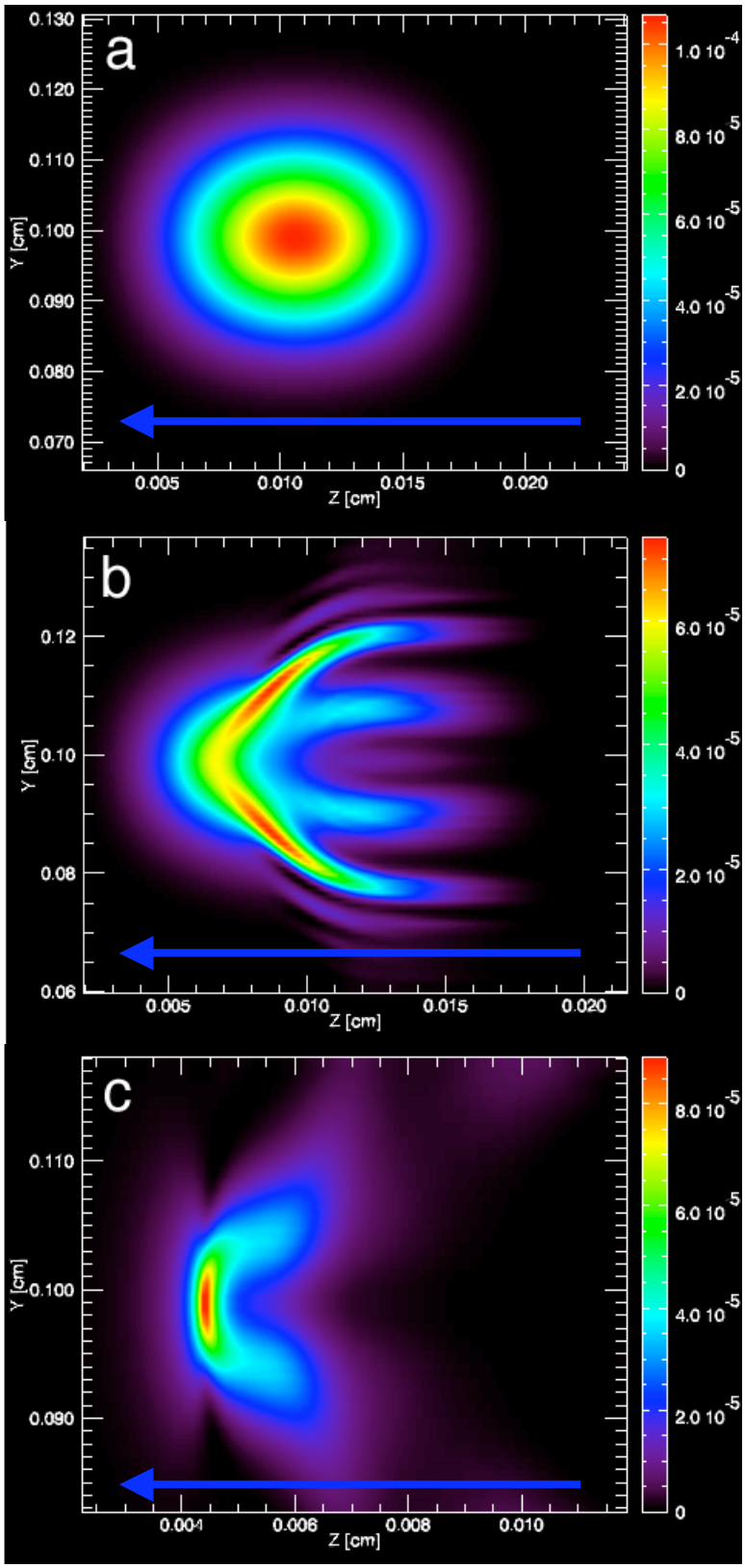
a
0.130
0.120
0.110
0.100
0.090
0.080
0.070
Y [cm]
0.005
0.010
0.015
0.020
Z [cm]
1.0 10^-4
8.0 10^-5
6.0 10^-5
4.0 10^-5
2.0 10^-5
0
b
0.12
0.10
0.08
0.06
Y [cm]
0.005
0.010
0.015
0.020
Z [cm]
6.0 10^-5
4.0 10^-5
2.0 10^-5
0
c
0.110
0.100
0.090
Y [cm]
0.004
0.006
0.008
0.010
Z [cm]
8.0 10^-5
6.0 10^-5
4.0 10^-5
2.0 10^-5
0

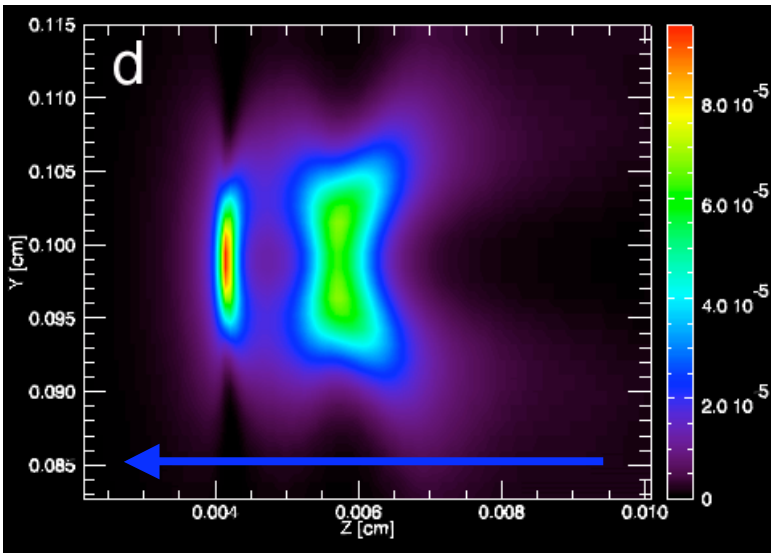

Figure 4. Simulation of a laser pulse with vacuum spot size 0.178 mm and power 4.5×10^{11} W, ~$2P_{cr}$. a) The initial pulse at the vacuum focal plane for the pulse. b) The laser pulse after ~1.5 cm propagation in 141 torr Helium. c) Laser pulse after 10.5 cm propagation., d) Laser pulse after 16.5 cm propagation. In vacuum the maximum intensity of the pulse should occur in figure a) and the laser pulse diffract from this point. Notice in figure c) that the highest intensity point is earlier in the laser pulse, 0.005 cm vice 0.01 cm, and this is where the ionization occurs. This ionization causes plasma, which leads to refraction of the later part of the laser pulse.

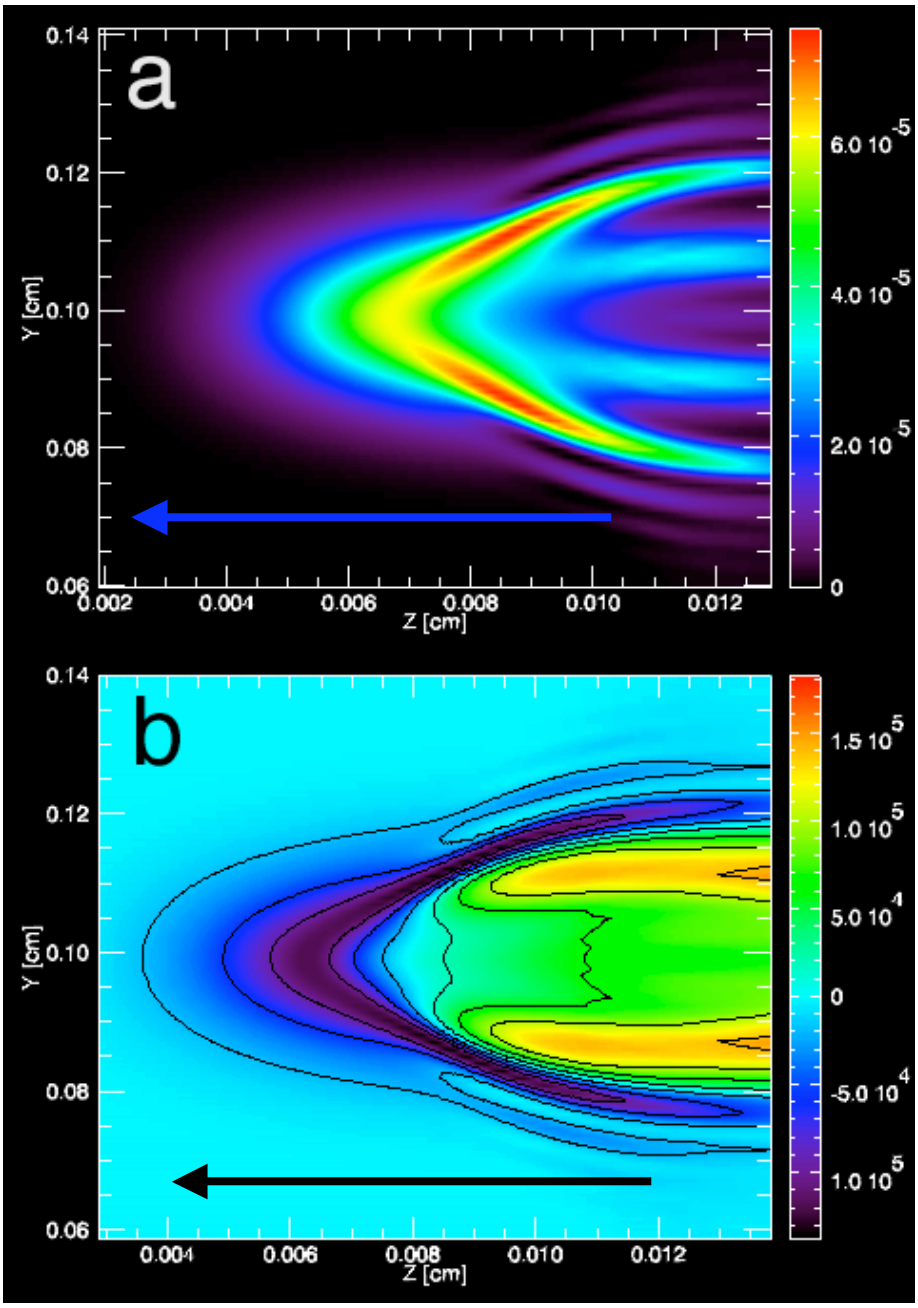
a
0.14
0.12
0.10
0.08
0.06
Y [cm]
0.002
0.004
0.006
0.008
0.010
0.012
Z [cm]
6.0 10^-5
4.0 10^-5
2.0 10^-5
0
b
0.14
0.12
0.10
0.08
0.06
Y [cm]
0.004
0.006
0.008
0.010
0.012
Z [cm]
1.5 10^5
1.0 10^5
5.0 10^4
0
-5.0 10^4
1.0 10^5

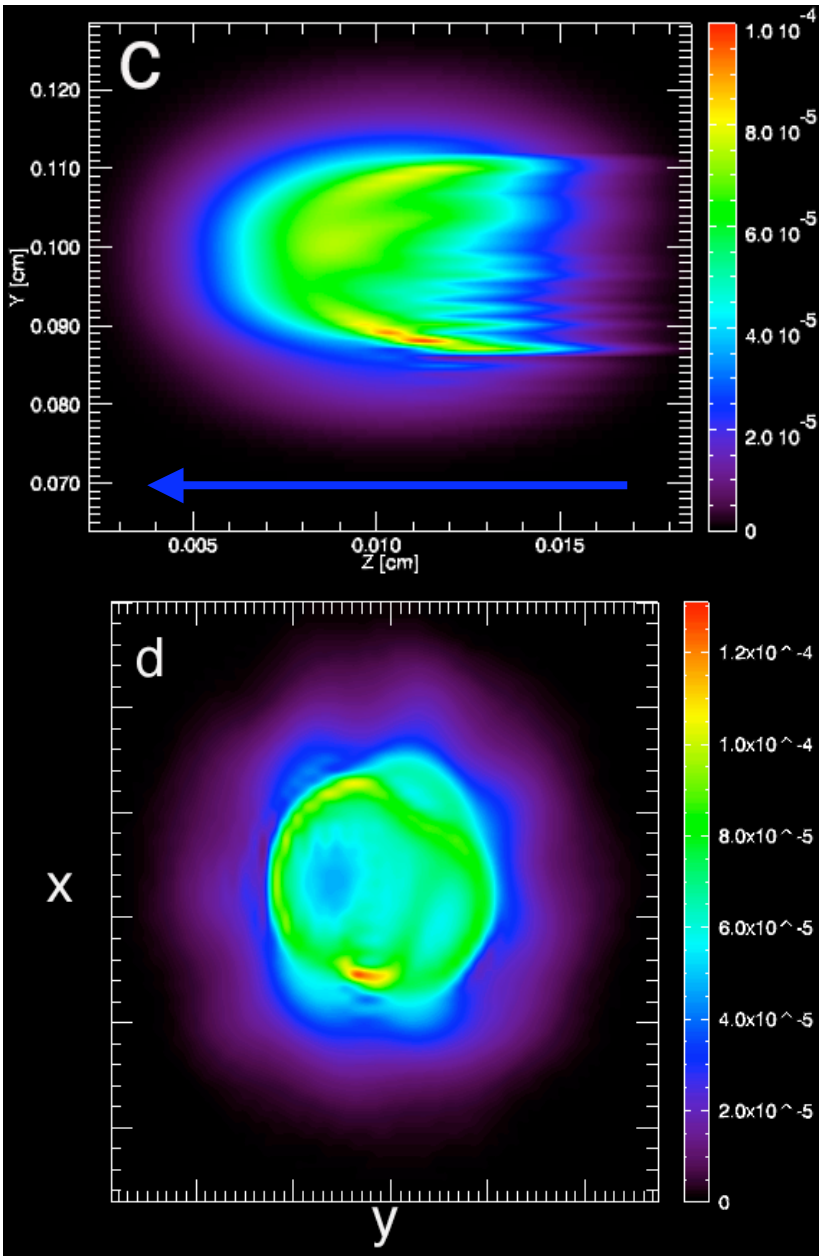

Figure 5. Mid-plane for smooth gaussian pulse at $2P_{cr} \simeq 0.5x10^{12}W$ for a) laser pulse after propagating 1.5 cm in 141 torr Helium gas jet and b) δε for ionization and Kerr self-focusing at 1.5 cm propagation distance. Notice that figure a) has the front of the pulse focused on axis but the mid-section of the pulse is refracted and propagates off the optical axis. We see in Figure b) that there is a local minimum in the dielectric response at the location of laser pulse guiding in figure a). Figure c) shows the mid-plane of the laser pulse for identical conditions as a); however, in c) and d) the pulse was initialized with random noise in the direction transverse to the laser pulse with magnitude one percent the main pulse magnitude. Figure c) shows the laser pulse after 2.7mm propagation distance. Notice that the cylindrical symmetry exhibited in a) is no longer present. Figure d) shows a plane cut transverse to the propagation direction at approximately .0115 cm in the laser frame.

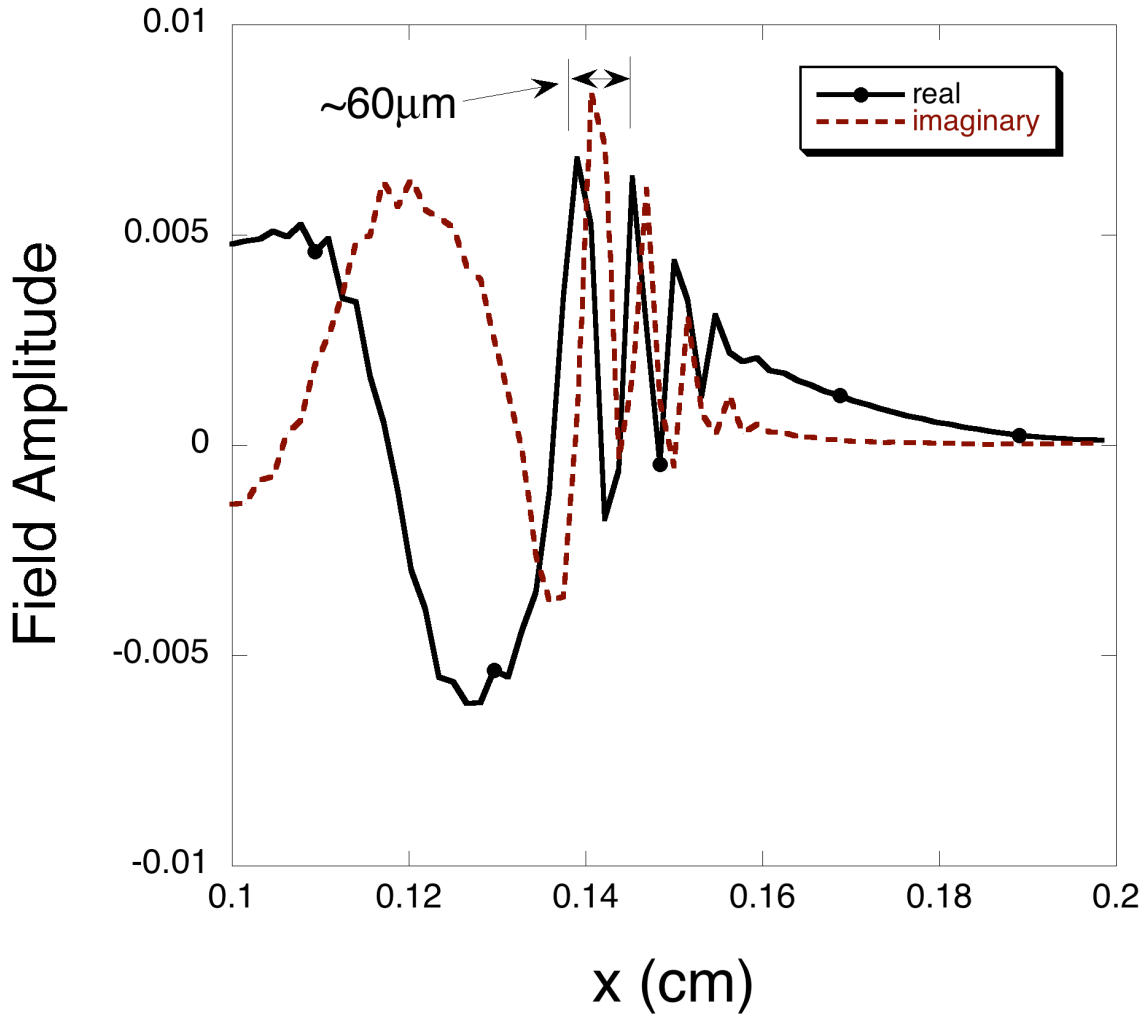

Figure 6. Real and Imaginary field amplitude for half the simulation domain. Notice that the field is an outward propagating wave with a transverse wavenumber that corresponds to a density of $n_e \simeq 5x10^{17}\,cm^{-3}$ which is less then the expected value of $n_e \simeq 1x10^{19}\,cm^{-3}$ for fully ionized gas. However, the laser pulse did not achieve maximum focus and the electron density reached a maximum value of about $n_e \simeq 5x10^{17}\,cm^{-3}$ so the result is consistent.

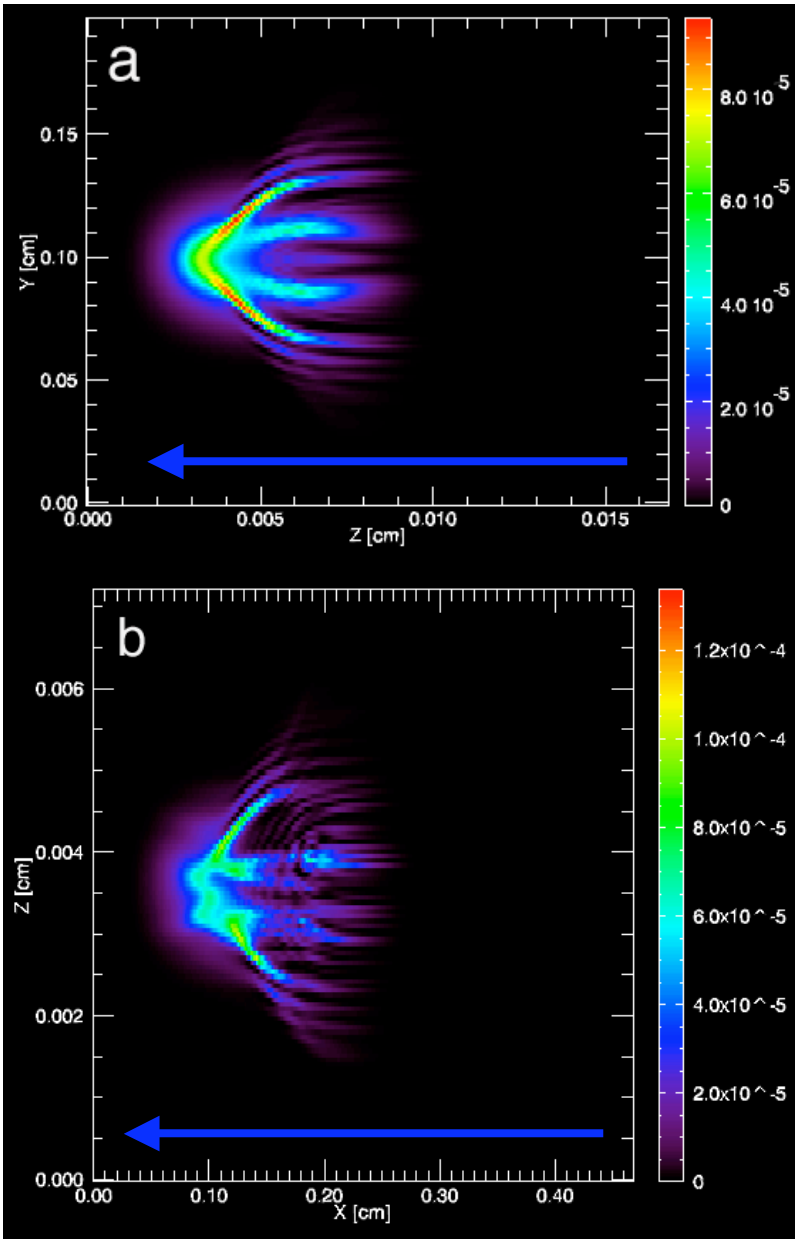

Figure 7. Mid-plane of gaussian pulse at $5P_{cr} \simeq 1.2x10^{12}W$ for after 3 cm propagation in 141 torr Helium for a pulse that a) has no initial transverse structure and b) has a one percent random transverse noise initially. Notice that in the case of no initial noise the pulse has symmetric rotational structure, for the case with noise the symmetry is broken.

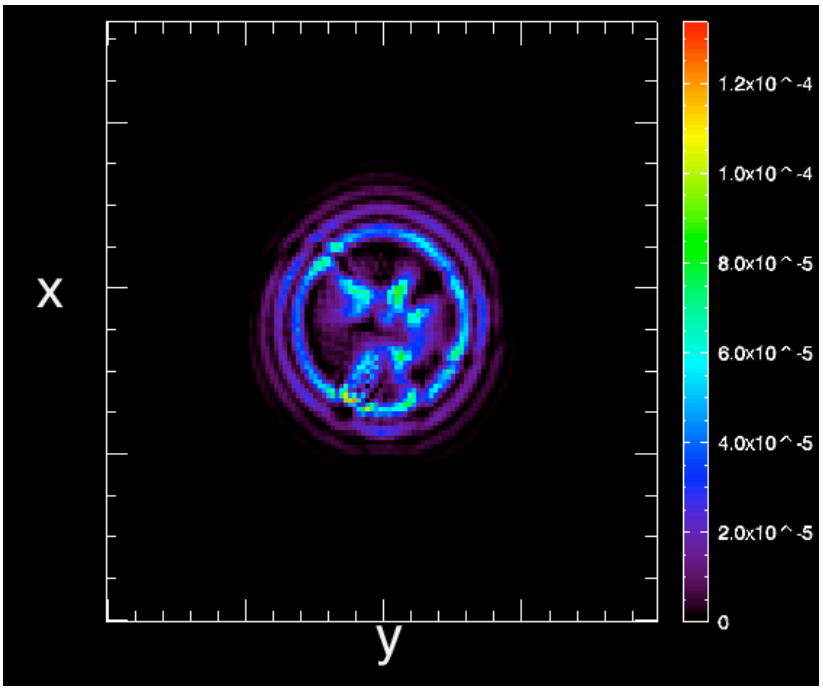

Figure 8. Slice of laser pulse transverse to the propagation direction for laser pulse with $5P_{cr} \simeq 1.2x10^{12}W$ with one percent transverse noise initially at 0.012 cm back in the pulse frame. Notice that there are approximately five filaments in this transverse slice.

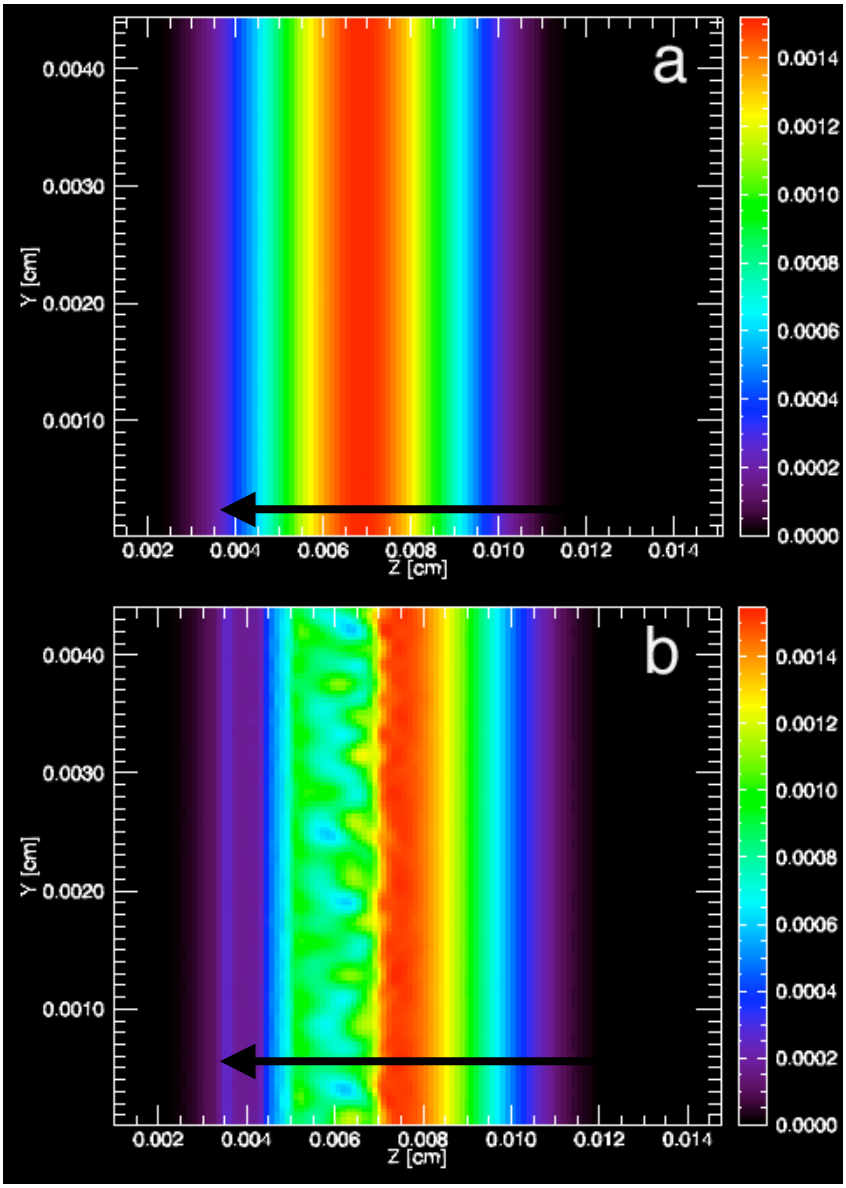

Figure 9. a) Initial mid-plane section for simulation with peak intensity $1x10^{16}$ W/cm^2 with random transverse perturbations at $1x10^{-5}$. b) Laser pulse mid-plane after 1.9 mm propagation distance in 141 torr He gas. Notice the transverse structure in the front region of the pulse due to the ionization scattering instability.

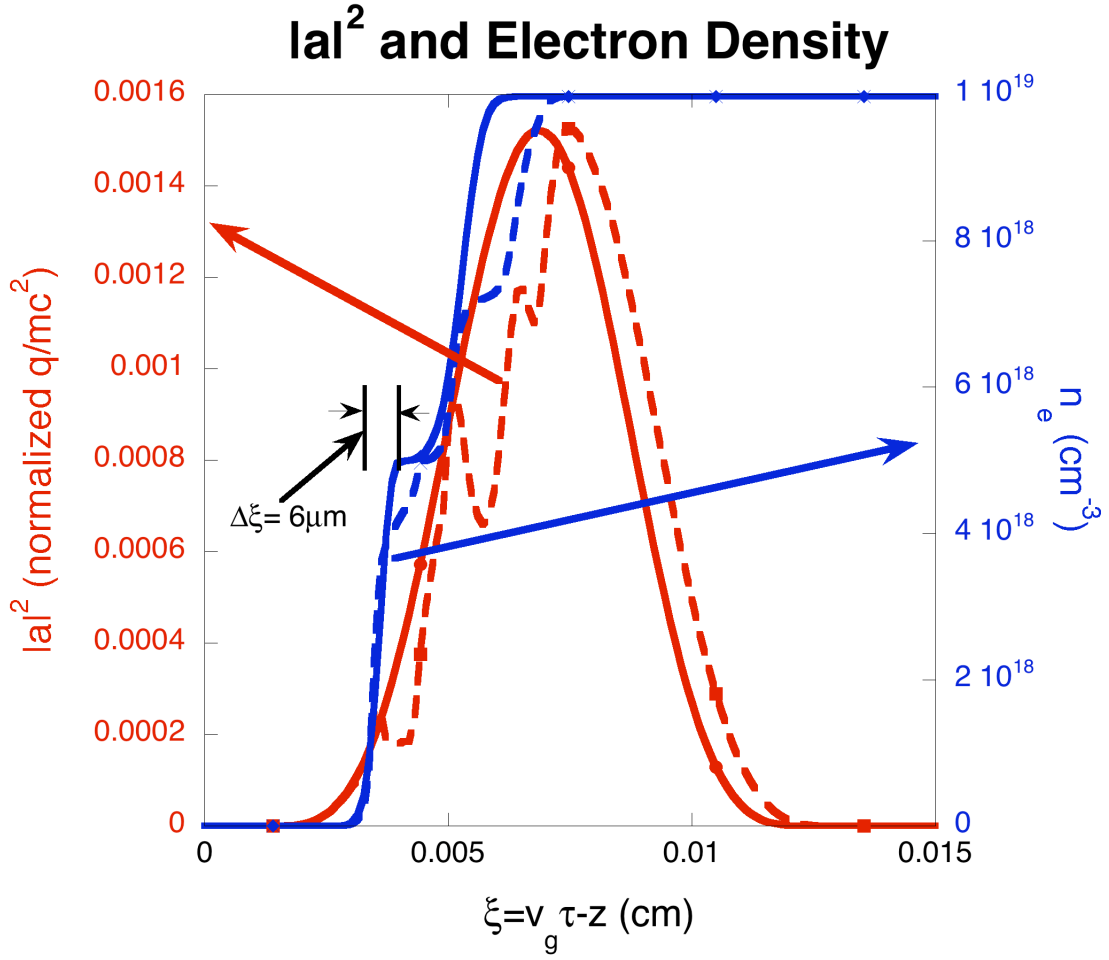

Figure 10. Lineout of the initial(solid) and final(dashed) laser pulse magnitude and electron density for the plane wave simulation in figure 5. Notice the filaments grow in regions undergoing rapid ionization.

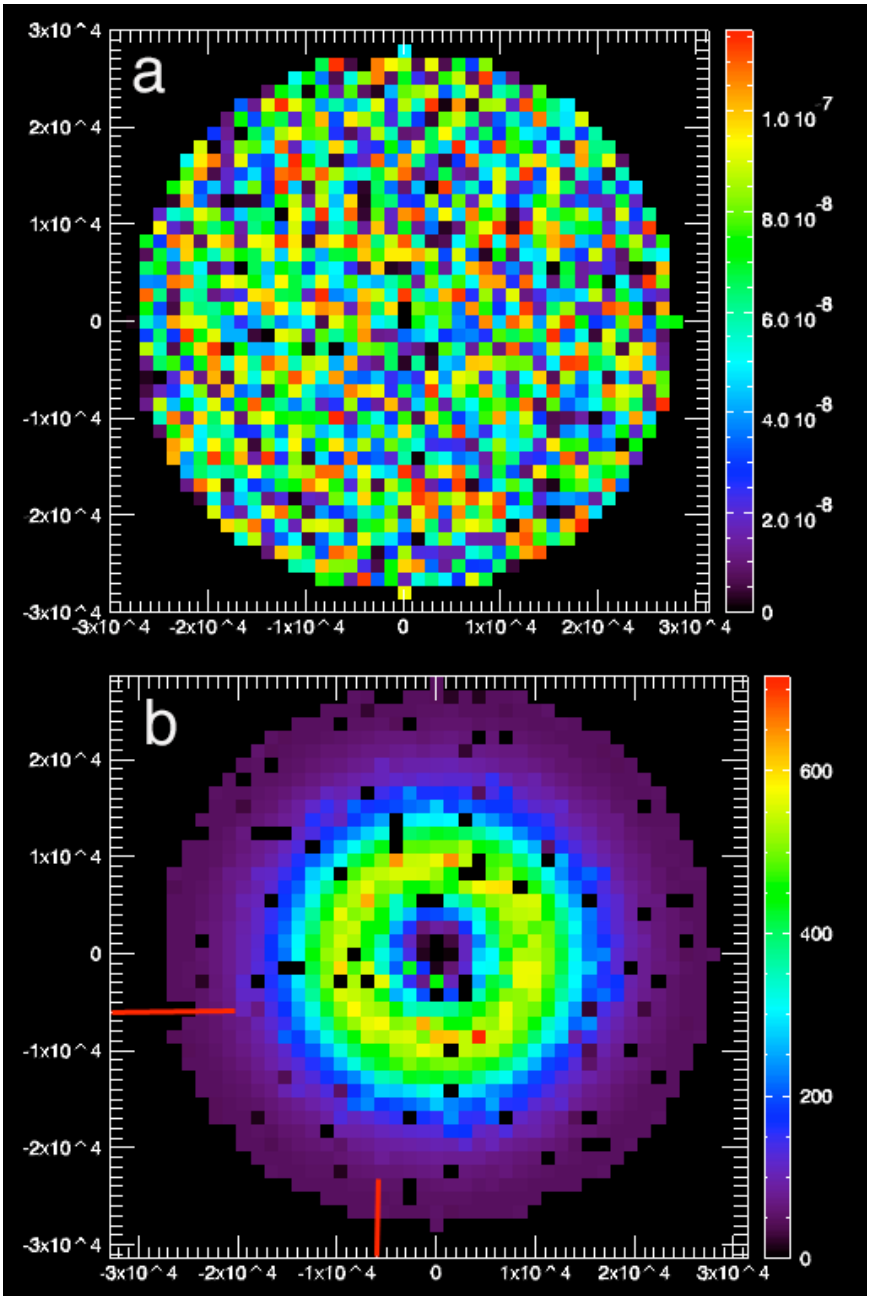

Figure 11. a) Initial seed for transverse modes in figure 5. b) Growth in transverse mode $\delta a_k / a_{k,0}$. The plasma wave number, $k_p = \omega_p / c = 0.5945 x 10^4$ cm^{-1}, is identified with solid lines on both axis. The maximally growing modes occur around $1.5 k_p$ consistent with this instability being convective in nature.

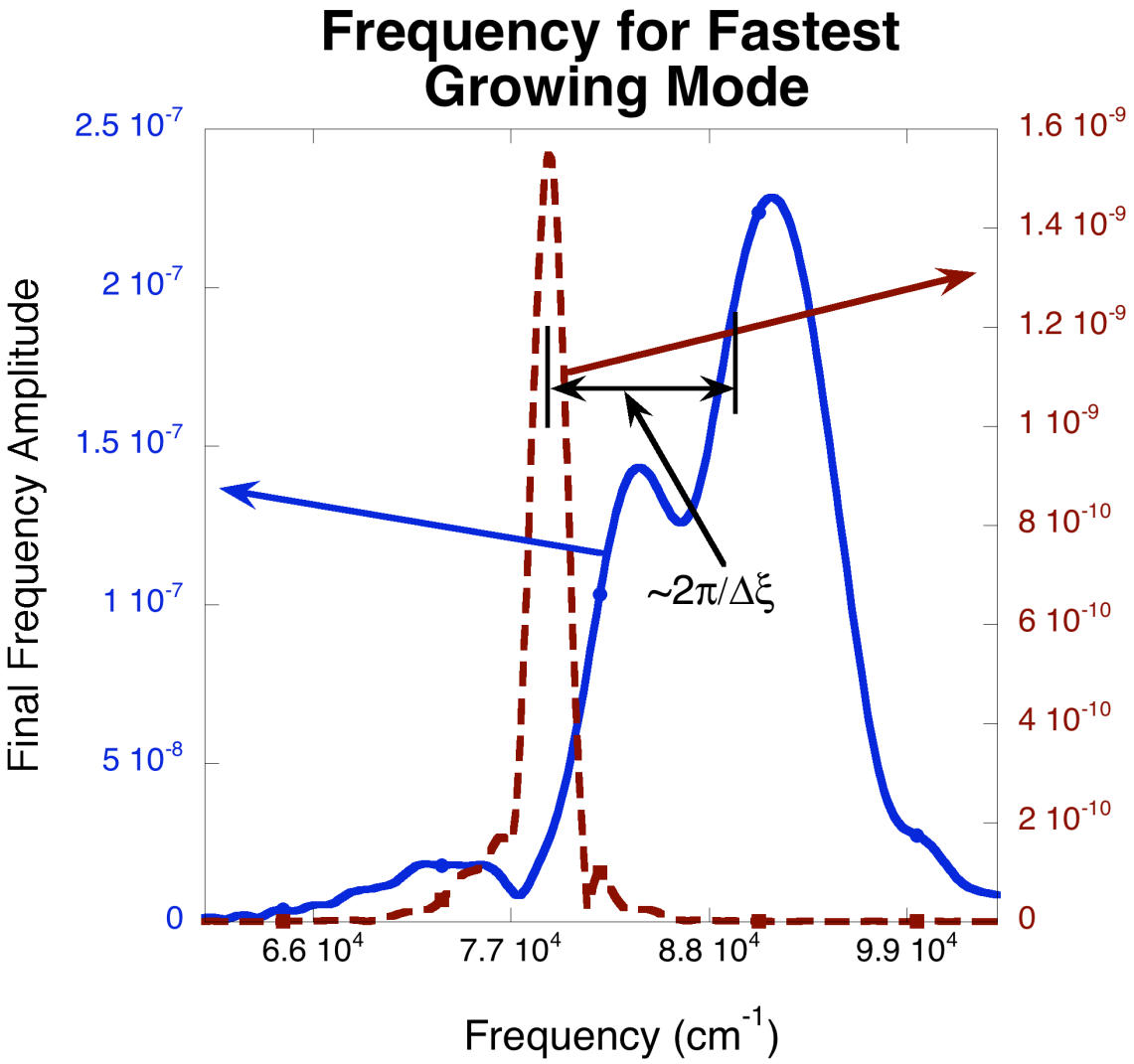

Figure 12. Wavenumber for the fastest growing transverse mode for initial (dashed) and after 1.9 mm of propagation (solid) in 141 torr Helium gas. Notice that the frequency is blue shifted by an amount that scales like the steep ionization front shown in figure 6.

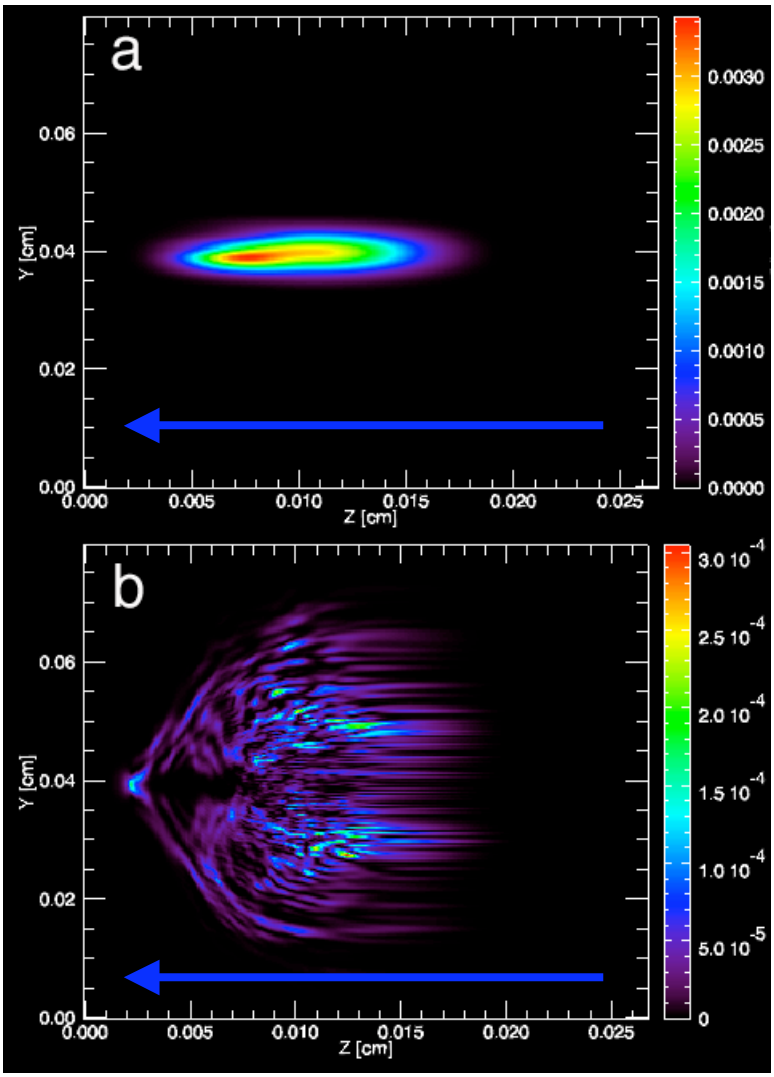

Figure 13. Mid-plane of gaussian laser pulse for a) initial pulse entering a 141 torr Helium gas jet and b) the laser pulse after 3.5 mm propagation in the gas jet. Notice in figure b that the front of the pulse is still tightly focused while the trailing part or the laser pulse has been both refracted off the optical axis and has undergone filamentation.

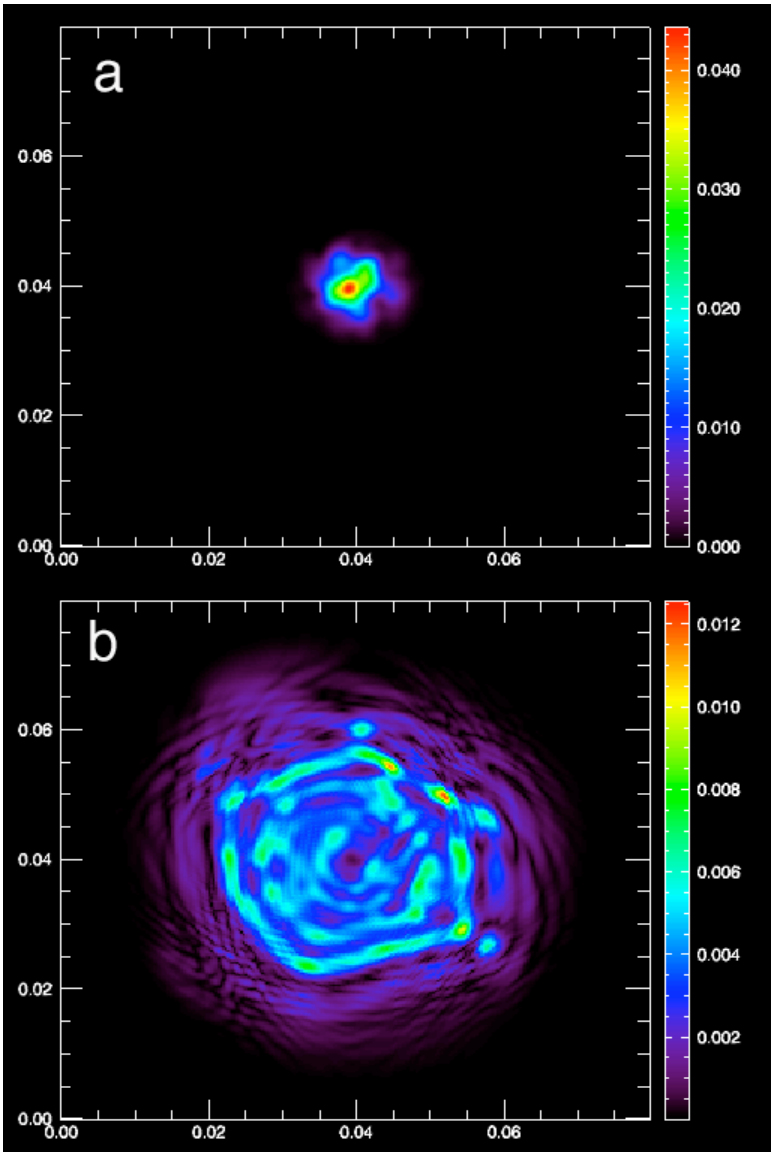

Figure 14. Transverse slice of gaussian laser pulse at approximately .005 cm in the laser pulse frame for a) initial pulse entering 141 torr He gas jet and b) pulse after propagating for 3.5 mm in gas jet. Transverse slices are at the same location in the pulse. Notice the ring structure in (b) due to the refraction from the plasma - off-axis guiding.

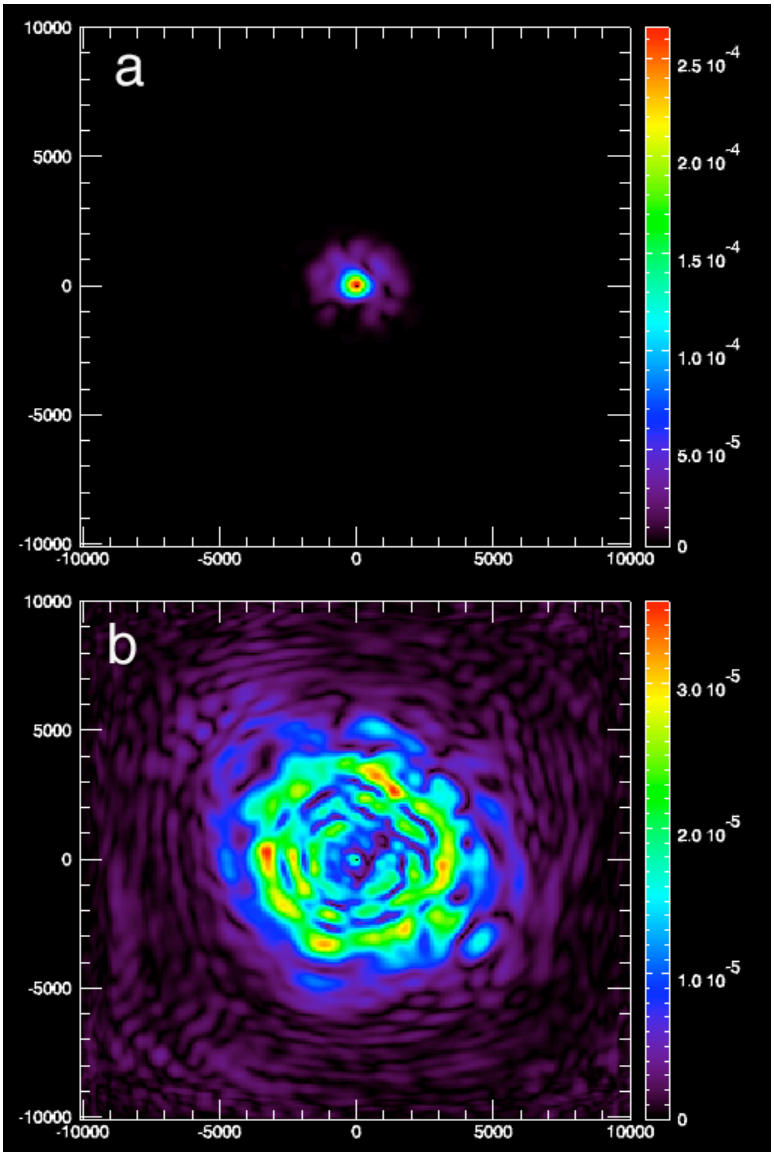

Figure 15. Transverse FFT for a) initial gaussian laser pulse entering 141 torr He gas jet and b) Transverse FFT after pulse has propagated 3.5 mm through jet. Transverse slices are at the same axial location in the laser pulse. The plasma wavenumber for these conditions for full-ionized helium is 5945 cm^{-1}.

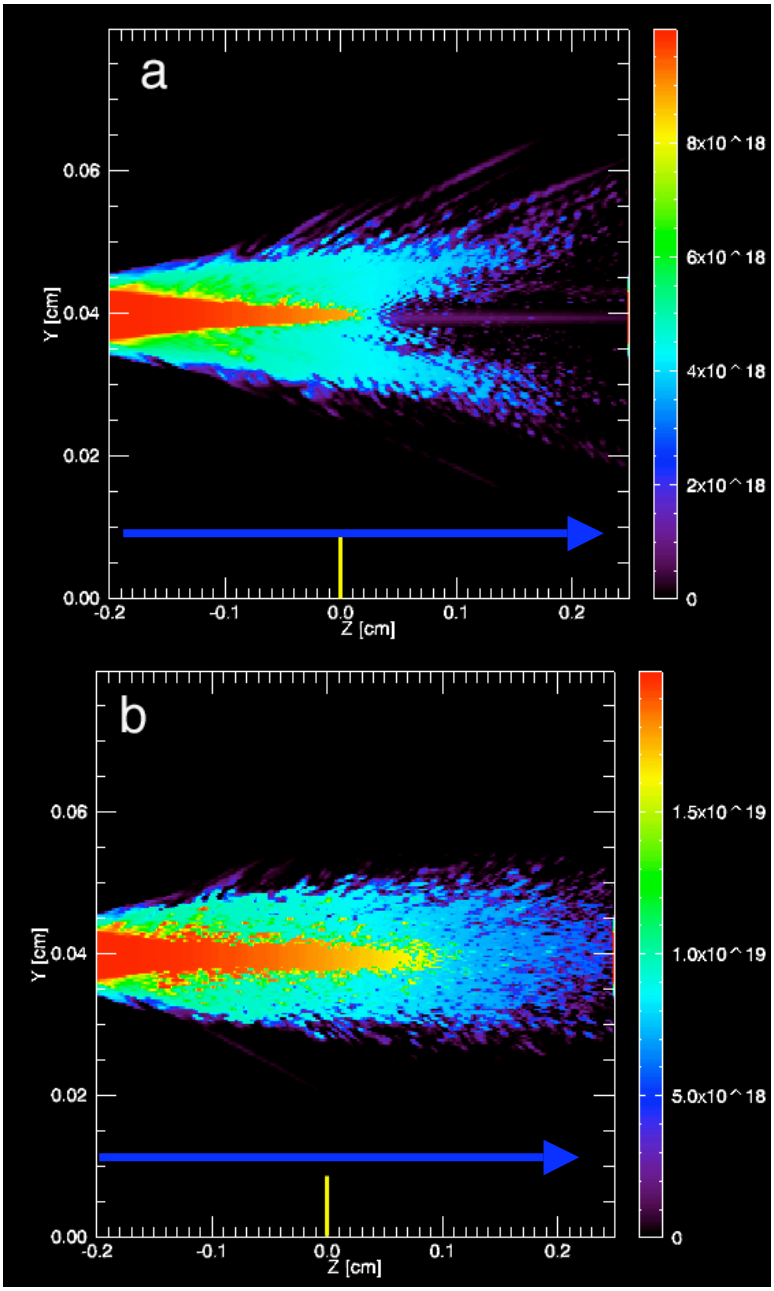

Figure 16. Electron Density at mid-plane of laser pulse propagation after laser has past, z=0 is the location of optical focus, for a) laser pulse propagating through 141 torr He gas jet and b) laser pulse propagating through 242 torr He gas jet. Notice the increase in forward directed ionization in the higher density case.

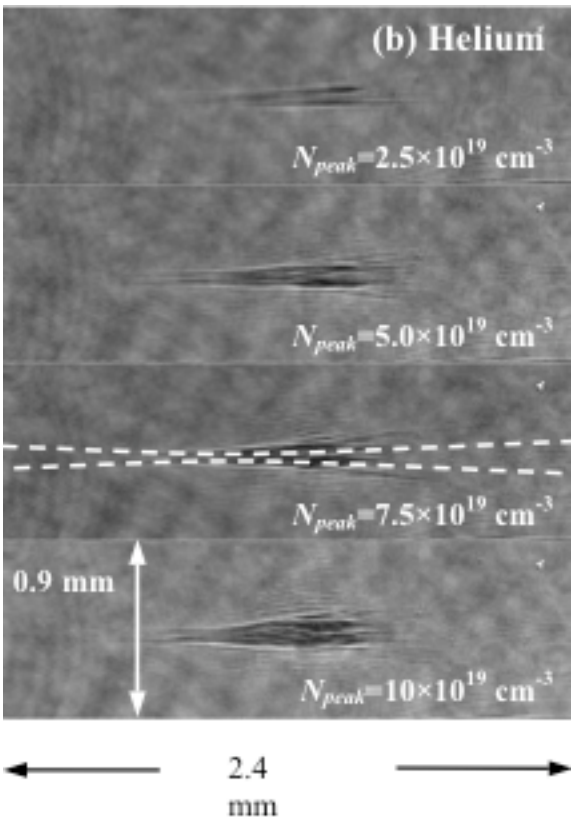

Figure 17. Experimental shadow grams [82] for plasma created in Helium gas jets at different valve backing pressures. Images taken 10 ps after the laser pulse, peak power ~ 2.8x10^{12} W, enters from the left. Estimated peak neutral density on each slide. The white dashed line indicates the laser pulse envelope in vacuum.

Chapter 5: Effective Electron Beam Injection with Broad Energy Initial Beam

Introduction

Laser Wakefield accelerators (LWFA)[1] have the potential for providing high-energy electron beams at a fraction of the current cost for a standard linear accelerator. Several potential schemes for LWFA have been proposed and studied. These include resonant LWFA, in which a single laser pulse that is resonant with the plasma wave ($\omega_p \tau_{laser} \cong \pi$, and $\omega_p = 4\pi q^2 n_e / m_e$ is the plasma frequency) excites an accelerating plasma structure, beat-wave (BW) LWFA[1,10,11], in which two long laser pulses beat providing an amplitude modulation at the period of a plasma wave, and self-modulated (SM) LWFA[11], in which a single long laser pulse undergoes forward Raman scattering and acquires amplitude modulations at the plasma period. It is believed that the scheme with the best potential to provide high quality final electron distributions is likely to be the resonant LWFA. This is because it involves the shortest laser pulse and consequently the pulse evolution is least affected by interaction with the plasma.

The resonant LWFA typically operates in the linear plasma wave regime and can produce a stable and controllable accelerating structure. Development of optical guiding schemes, such as plasma channels formed either by capillary discharge[17] or line discharge through use of an axicon lens[15,67,68], have demonstrated guiding of very high laser intensities over many characteristic propagation lengths, $z_r = k_0 r_0^2 / 2$, where r_0 is the laser vacuum focal spot size and k_0 is the carrier wave number for the

laser. The final element required to demonstrate LWFA in the resonant case is an initial electron beam to inject into the plasma wakefield.

Ideally, the injected electrons will be produced in such a way that they are mono-energetic and placed in the accelerating phase of the plasma wave. One difficulty in providing these electrons is the need for precise timing between the electron bunch and the laser pulse used to provide the plasma wave wake. Since the plasma wakefield period is typically about 100 fs, for $n_e \cong 1\times10^{18}$ cm^{-3} proper phase injection requires timing much better then this period e.g., 30 fs. This timing requirement suggests use of an all-optical injection scheme to provide the electrons.

Several methods for creating this electron bunch have been proposed. These include Laser Ionization and Ponderomotive Acceleration (LIPA)[80], use of wire targets[81], use of SM-LWFA[69], Laser Injection Laser Acceleration[70] (LiLAc), and colliding pulse injection[71] (CPI). Each of these methods has characteristic electron distribution in both energy and bunch duration. For instance, in LIPA an intense laser is used to ionize an electron from an inner atomic shell. When the electron is first ionized it is exposed to a high laser electromagnetic field, which quickly propagates away. This electric field imparts residual energy to the electron leaving it with a relativistic momentum, e.g., some electrons have energy greater then 1x10^6 electron volts (eV). However, one common trait for most of these methods is a broad electron energy spectrum when the method is used at a high intensity and a high density, which is necessary to provide a significant numbers of electrons needed for any practical accelerator.

In this chapter, we examine the properties of the acceleration process for an electron distribution that initially has a broad energy spectrum and demonstrate that it is possible to utilize these electrons and still produce an adequate accelerated electron bunch. The remainder of the chapter is outlined as follows. In section 2, we discuss the one-dimensional Hamiltonian[72] and resulting electron equations of motion and we utilize this system to gain insight into the phase space evolution of the electrons. We then perform two-dimensional test particle simulations, using WAKE[39], to compare with the results of the Hamiltonian analysis. These simulation results are presented in section 3 along with results from a series of two-dimensional simulations, performed using TurboWave[76] that include fully self-consistent fields from the electrons. In section 4, we discuss the implications of these results for planned and future resonant LWFA schemes. Finally, we conclude with a discussion of unresolved questions and provide an outline of future plans.

Hamiltonian Formalism

Detailed discussion of the one-dimensional Hamiltonian formalism are presented elsewhere[72]. Therefore, the current discussion will be limited to specific results necessary for understanding the current analysis. In particular, in one-dimension, the Hamiltonian function given by

$$H(\gamma,\psi) = \gamma\left(1-\beta_g\beta\right)m_e c^2 + q\phi\sin\psi \qquad (1)$$

is constant for an electron in the frame of the pulse propagation, $\xi = z/v_g - t$. Here $\phi = q\Phi/m_e c^2$ is the normalized plasma wake-field electrostatic potential, $\psi = \omega_p\xi$, $\omega_p = 4\pi q^2 n_e/m_e$ is the plasma frequency and m_e and q are the mass and charge for

an electron. The quantity γ is the electron Lorentz factor and is related to $\beta = v_e / c$ by $\gamma = 1/\sqrt{1-\beta^2}$. Finally, $\beta_g = 1 - \lambda^2/2\lambda_p^2 - \lambda^2/2\pi^2 r_o^2$ characterizes the laser pulse group velocity and includes the effects due to finite laser spot size [73], $\lambda_p = 2\pi c/\omega_p$ is the plasma wave wavelength and $v_g = c\beta_g$. The Hamiltonian is a periodic function of phase with period 2π. Within the interval -π/2 to 3π/2 acceleration occurs for phases from 0 to π/2.

This Hamiltonian function neglects the transverse wake field affects that contribute a radial force to the dynamics of the electrons. In uniform plasma, this radial force is out of phase with the accelerating force in the wake by π/2. We can include these radial effects in the current case by assuming that only electrons that remain in the region of phase with a focusing electric field gradient in the radial direction will remain in the accelerating wake. Based on this assumption of radial force, only phases from 0 to π need be examined in detail. Within this region the Hamiltonian function has a single stationary point with $\gamma_g = 1/\sqrt{1-\beta_g^2}$ at $\psi = \pi/2$.

With this Hamiltonian, we can obtain the equations of motion for the normalized momentum, $\tilde{\mathbf{p}} = \mathbf{p}/mc$, and phase, ψ, in the laboratory frame coordinate, z. These equations are

$$\frac{d\tilde{\mathbf{p}}}{dz} = -q\phi_0 \frac{\omega_p}{c\beta_g}\left(1 + \frac{1}{\tilde{\mathbf{p}}^2}\right)^{1/2} \cos\psi\,, \tag{2a}$$

and

$$\frac{d\psi}{dz} = \omega_p\left[\frac{1}{v_g} - \frac{1}{c}\left(1 + \frac{1}{\tilde{\mathbf{p}}^2}\right)^{1/2}\right]. \tag{2b}$$

Figure 1 shows the phase space trajectories of several particles with initial normalized momentum around four and initial phase from $\pi/2$ to π integrated according to Eqs. 2. The conditions for the wake amplitude correspond approximately to the plasma wake stimulated by a 10×10^{12} W laser focused to a vacuum spot size of 30 μm, ϕ=0.1, in a plasma density 5×10^{17} cm^{-3}. The solid line represents the orbit that encompasses the maximum region of phase space that remains in a focusing electric field. The electron that follows this trajectory has a phase of $\pi/2$ and normalized momentum of 4.3. This electron represents the lowest initial momentum that can be trapped by the plasma wakefield.

Two-dimensional Simulation Results

We have performed a number of two-dimensional simulations using the code WAKE[39] with a test particle electron bunch. These simulations correspond to parameters, which were identified as interesting based on the above analysis and based on projected experiments to be performed at the Naval Research Laboratory (NRL) in the near future. Figure 2a shows the on-axis initial laser intensity and normalized wakefield for the case that corresponds to a laser pulse peak power of approximately 10 10^{12} W and laser spot size of 30 μm, peak intensity approximately 7.1×10^{17} W/cm^2. Figure 2b shows the accelerating field and the radial focusing field for a location off the optical axis. Notice that the total phase that is both accelerating and focusing is larger then the previous Hamiltonian analysis assumes, $-\pi/6 < \psi_{useful} < \pi/2$. This increase in useful phase allows electrons with lower energy to be trapped and accelerated in a plasma channel as well as leading to

increased total energy gain. This effect was first identified by Andreev[40]. Additional details of these results and the impact on trapping non-ideal electron bunches will be discussed in future work.

The above laser pulse simulation was allowed to propagate for 6.4 cm, which corresponds roughly to the classical de-phasing length, which is defined as the maximum length z that an electron injected at the minimum momentum can be accelerated before it reaches the decelerating phase. This length is given by $L_d = \lambda_p / 4(1-\beta_g)$. Figure 3 shows the phase-space for the injected electrons. Figure 4a shows the initial bunch distribution. Additionally, for reference Fig. 3a includes both the trajectory that corresponds to the minimum-trapping orbit for the one-dimensional Hamiltonian discussed above and the Hamiltonian separatrix, which defines the largest closed orbit for the Hamiltonian. Figure 3b shows the phase space evolution during the initial acceleration process, the first 3.5 mm, while Fig. 3c shows the phase space trajectories for the initial and five evenly spaced intervals during the acceleration process, approximately every 1.3 cm.

Figure 4 shows results for integrating Eqs. 2 for six test particles that bound the initial region of phase space for the injected electrons in the above simulation shown in Fig. 3. The solid line in the relative momentum spread and the dashed line is the mean momentum of the bunch. Notice that the relative momentum spread initially decreases until about 3.5 cm propagation length. The mean energy for the electrons at this time is approximately 550. After this acceleration length the relative momentum spread increases rapidly. This is a common characteristic of this type of initial beam and is due to the fact that electrons with higher initial momentum or

lower phase will advance in the accelerating field more rapidly then the lower momentum electrons. These electrons will thus be exposed to less overall acceleration since they reach their de-phasing length more rapidly. The electrons that barely remain in the focusing region will experience the most total acceleration and thus have higher total energy gain.

This result is consistent with the simulation presented above. In particular they indicate that the relative momentum spread and maximum momentum gain are not independent and that the optimal beam quality will require a trade-off with total energy gain. This result is most clearly seen in Figure 4c which shows that a high quality electron bunch is present at half the acceleration length approximately 3.8 cm. The normalized momentum is over 600 while the relative momentum spread is 2.1%. As the electron bunch continues to accelerate the rear of electron bunch can be seen to gain energy relative to the head of the bunch, thus increasing the relative spread in momentum.

One additional consequence of these interesting dynamics is that the optimal warm bunch for injection is dependent on the accelerator design parameters and peak wakefield amplitude. Figure 5a shows that phase-space evolution for an injection beam that is identical to the one presented in Fig. 3 but injected into a wake that is driven to an amplitude $\phi = 0.4$. In this case you can see that the energy spread rapidly increases. This phenomenon is the result of the increased wakefield amplitude trapping a large initial volume of phase space. Figure 5b shows the phase-space for a beam with lower initial momentum spread, p_{init}=0.4. This electron bunch evolves into a beam with significantly lower spread in momentum then in the case of

Fig. 5a. Additionally, this beam results in much higher energy gain then the case in Fig. 3.

The final issue that we explore in two-dimensions is the maximum charge that can be trapped from an electron beam with a large energy spread. There are two issues involved in this beam-loading problem. The first involves the depletion of the wakefield amplitude as the plasma wave energy is converted into energy in the accelerated electrons. This problem has been described in detail [42,75]. The beam-loading issue that is of concern for the present work is associated with the effect of the electrons that have energy too low to be trapped, yet can disrupt the plasma wakefield initially such that the trapping and acceleration of higher energy electrons is reduced.

To explore this issue in two-dimensions we utilize the code TurboWave[76] in two-dimensional slab geometry. We treat the laser field in the ponderomotive limit and neglect the laser oscillation period. We have performed a series of simulations with self-consistent beam-loading effects. Figure 6 presents the charge in the accelerated bunch as a function of the total charge in the thermal beam for several values of total charge. The electron bunch was initially phased with a drift momentum of 0.1 and momentum spread of 1. The laser pulse was chosen to provide a normalized wakefield amplitude of 0.1, with a laser spot size 30μm consistent with the early results from WAKE.

We see in Figure 6 that approximately one percent of the electrons are trapped and accelerated up to a total charge of approximately $1x10^{11}$ electrons at which time the plasma wake is disrupted by the large electron charge present at the start of the

simulations. This disruption leads to a maximum total trapped charge of approximately 1.7×10^{9} electrons for a total charge of 1.2×10^{11} electrons. Further increasing the total charge disrupts the trapping process and leads to a decrease in total captured charge.

Implications and Conclusions

Based on the results of the above analysis and simulations, electron bunches with broad energy spread can be used for injection into resonant LWFA. However, it is not sufficient to specify the maximum energy gain for an accelerator system, rather one must determine the proposed application for the accelerated electron bunch and thus define the optimal final parameters. For instance, if maximum total energy gain is important and energy spread of the electron bunch is not important, then the LWFA length should correspond to the de-phasing length of the plasma wave. However, if the energy spread is critical then a reduced accelerator length and thus energy gain should be used.

It is also important to understand the characteristics of the LWFA in order to determine the parameters for the electron bunch used for injections. If the laser pulse peak intensity is low and thus the wakefield amplitude is around 0.1, then the electron distribution must have a higher effective temperature then for the high intensity and large wakefield amplitude. Failure to consider accelerator design features may lead to poor electron beam characteristics.

These results indicate that the need for a high quality cold, mono-energetic electron bunch is not necessary for the injection phase of a resonant LWFA. This suggests that electron beam injection should not hinder near-term efforts to construct

a multi-stage resonant LWFA and emphasis should be placed on producing and diagnosing a high-quality plasma wave in a plasma channel. Generating the optimal injection bunch will require knowledge of the details of this plasma channel.

We have presented a model that describes the initial electron bunch distribution in terms of an "effective temperature" for non-ideal electron distributions and have demonstrated the production of reasonable quality final electron beams with significant energy gain and minimal energy spread. The results of this analysis are strongly dependant on the overall accelerating system design and provide a useful means of choosing injections schemes from a multitude of possibilities. LWFA parameters must then be varied to optimize the final electron distribution, as required, once the accelerator characteristics are known. Further work is needed to examine effects of beam loading on trapping and accelerating process. In particular, the effect of the large electron charge, with energy just below the minimum trapping energy, on the plasma wakefield and subsequent trapping and acceleration of the electrons need to be examined with a self-consistent simulation. Continuations of this effort will be the subject of future work.

Figures

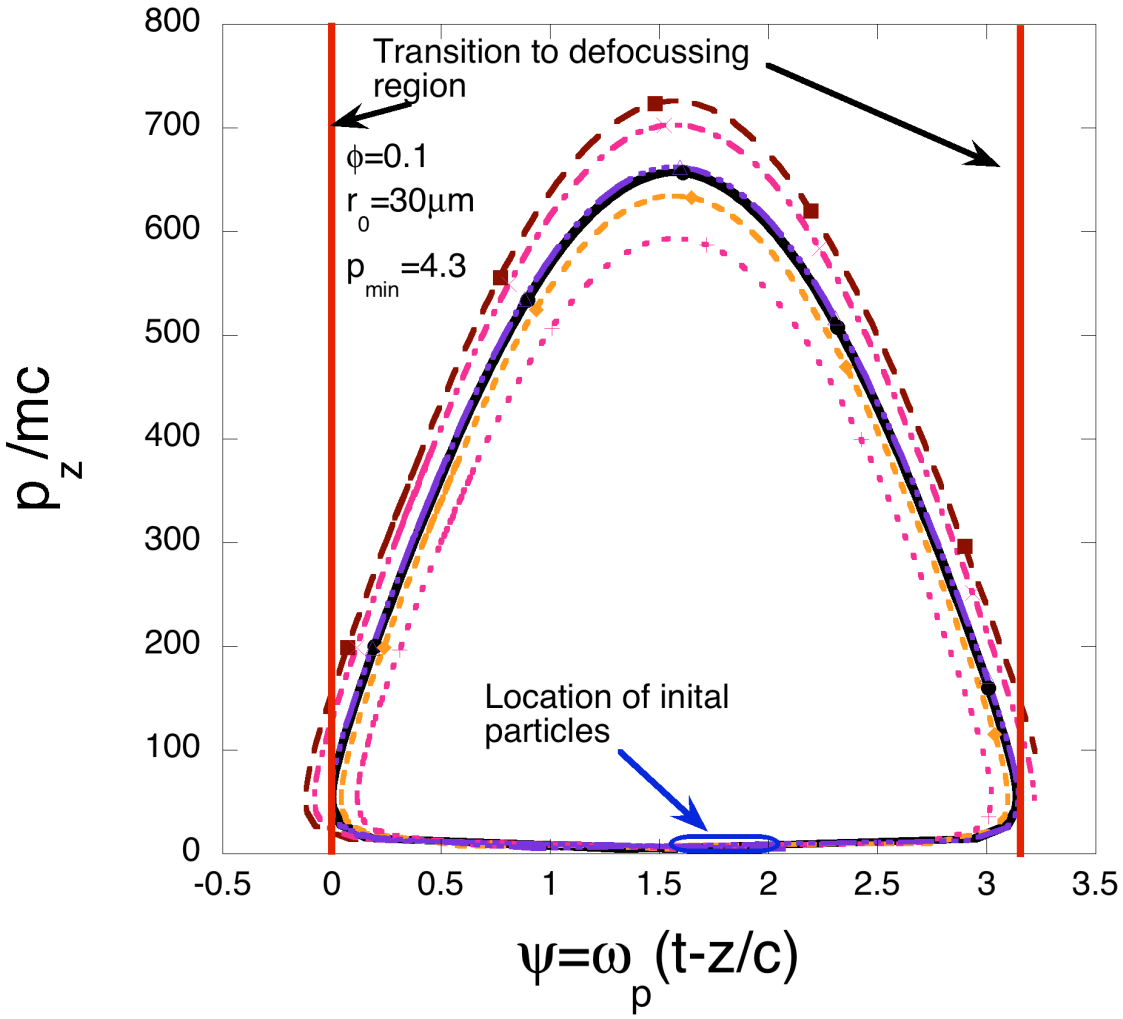

Figure 1. Phase space trajectories for particles evolved according to Eqs. 2 with initial conditions located as marked. The solid lines at y=0 and y=p demark the transition into de-focusing regions where electrons would be expected to be lost due to radial de-focusing.

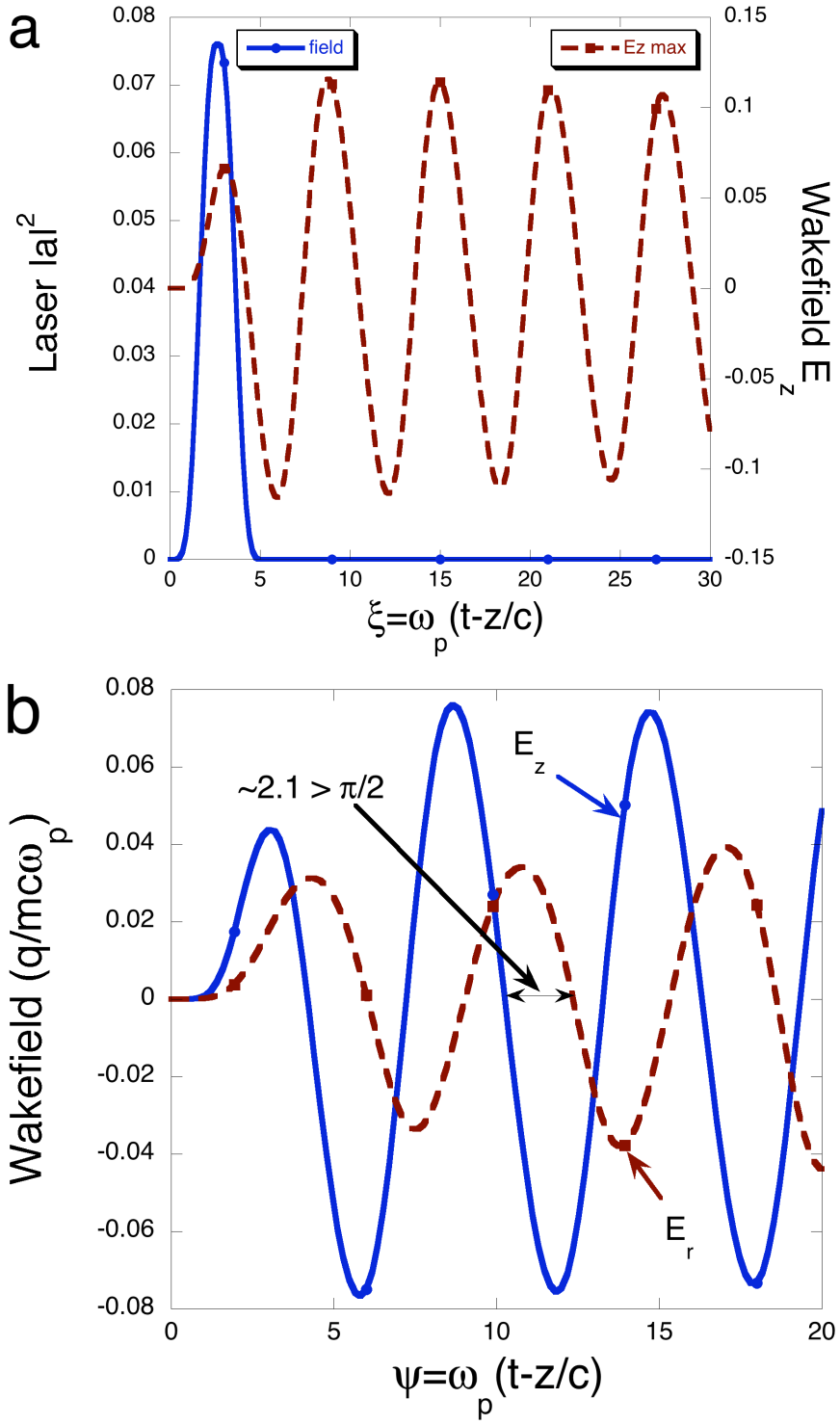

Figure 2. a) Initial laser pulse and accelerating wakefield on the optical axis. The peak-accelerating field corresponds to $\phi = 0.1$. b) Accelerating field and radial wakefield off the optical axis. Notice the overlap in phase between focusing and accelerating is greater then $\pi / 2$.

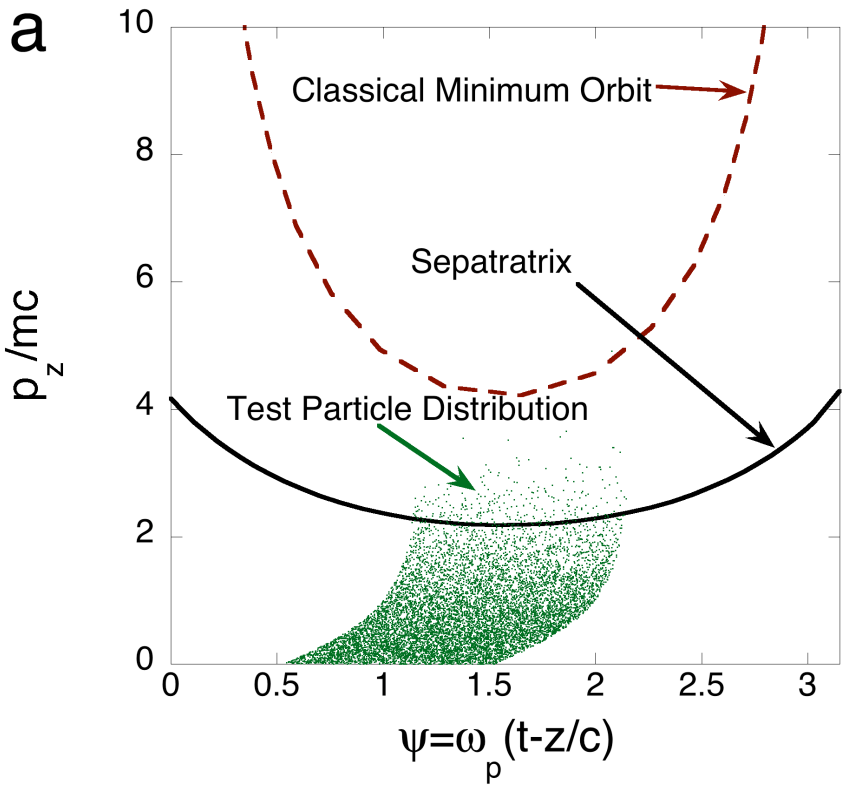
a
Classical Minimum Orbit
Sepatratrix
Test Particle Distribution
p_z/mc
ψ=ω_p(t-z/c)
0
2
4
6
8
10
0
0.5
1
1.5
2
2.5
3

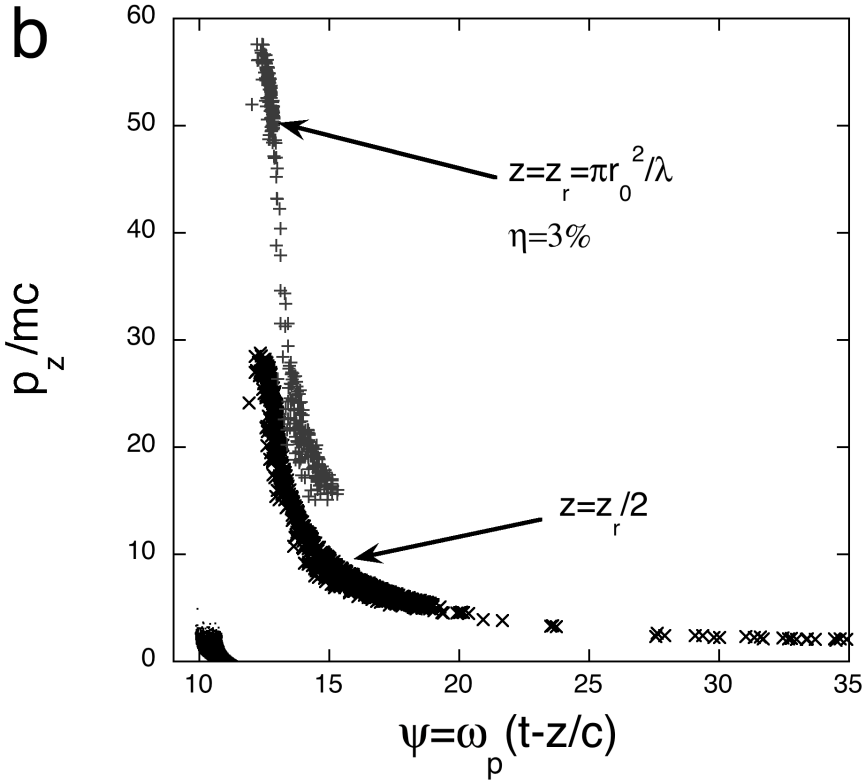
b
z=z_r=πr_0^2/λ
η=3%
z=z_r/2
p_z/mc
ψ=ω_p(t-z/c)
0
10
20
30
40
50
60
10
15
20
25
30
35

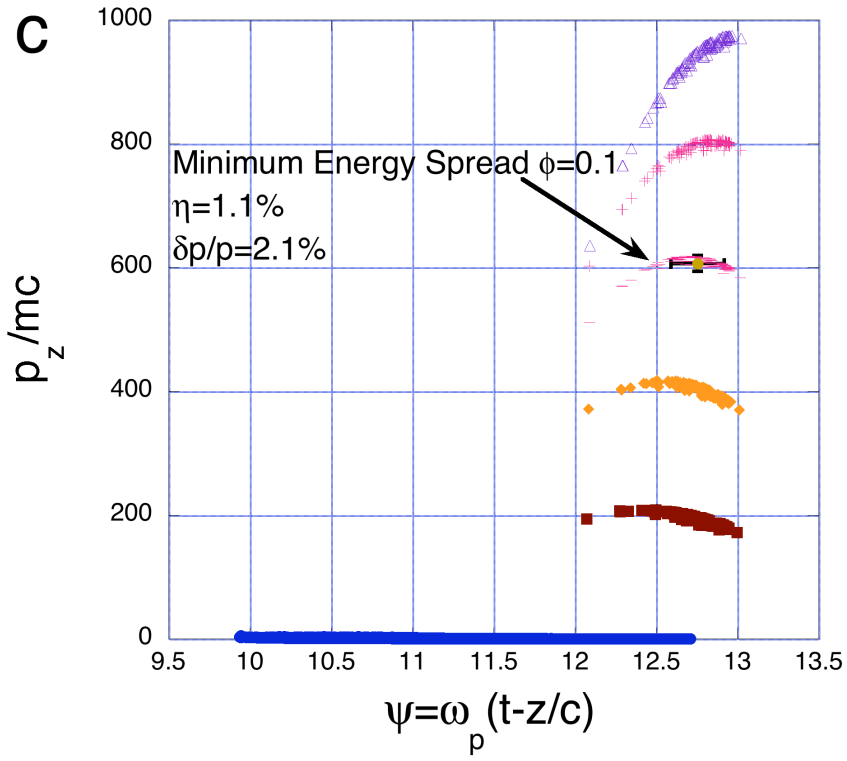

Figure 3. a) Initial particle distribution for this simulation. Also included are both the Hamiltonian orbit that corresponds to the minimum momentum for trapping in uniform plasma and the separatrix, the largest closed orbit for the Hamiltonian. Notice that none of the initial particles should be captured according to one-dimensional theory. b) Phase-space plot during the first 3.5 mm of acceleration for the test particles in the simulation. c) Phase-space plot for the entire simulation. Notice that after more then 6 cm of propagation about 1% of the test-particles are trapped and accelerated. Also notice that the minimum energy spread, ~2%, occurs after approximately 3.8 cm of acceleration but only results in momentum gains of 600, e.g. 300MeV electrons.

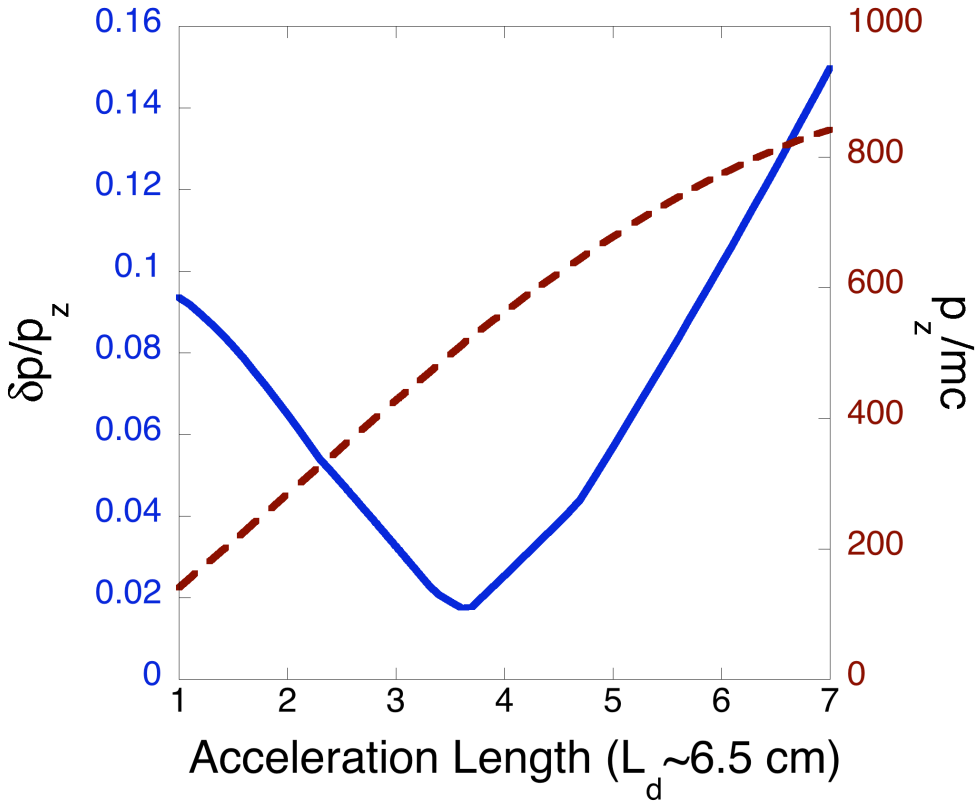

Figure 4. Plot of the Relative momentum spread (solid) and mean normalized momentum (dashed) as the electron bunch is integrated according to Eqs. 2. The initial particles were chosen to correspond to a six-point distribution containing the lowest energy electrons that will be trapped in the wakefield based on the WAKE simulation results. Notice that the minimum spread in momentum does not correspond to the maximum energy gain for the accelerator.

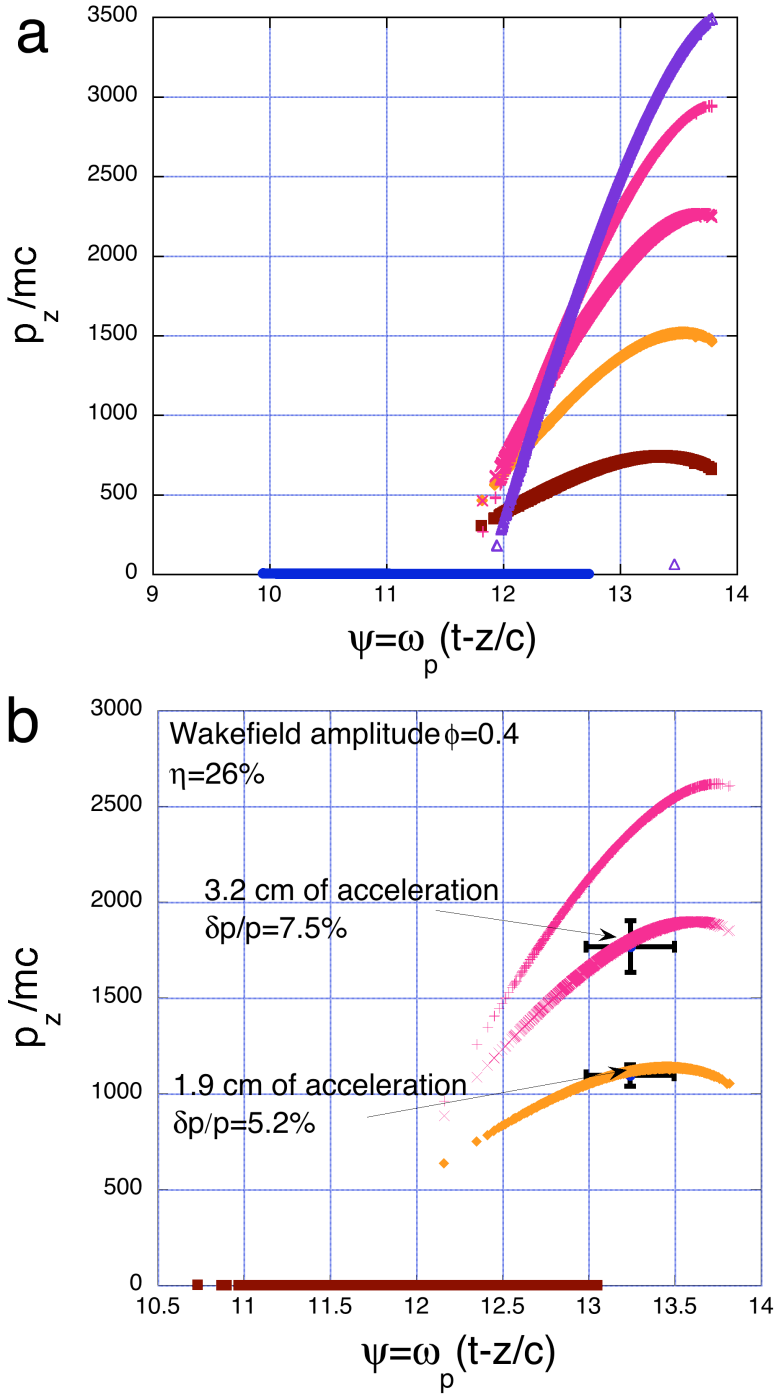

Figure 5. Phase-space plots for an accelerator with a wakefield amplitude $\phi = 0.4$. a) Initial electrons have Boltzmann distribution with temperature p=1.0. b) Initial electrons have Boltzmann momentum p=0.4. Notice that in (a) the quality of the electron beam is poor for all times. In (b), a reasonable quality beam can be extracted for the shorter acceleration lengths; however, the beam quality is very dependant on the initial Boltzmann distribution and injection phase.

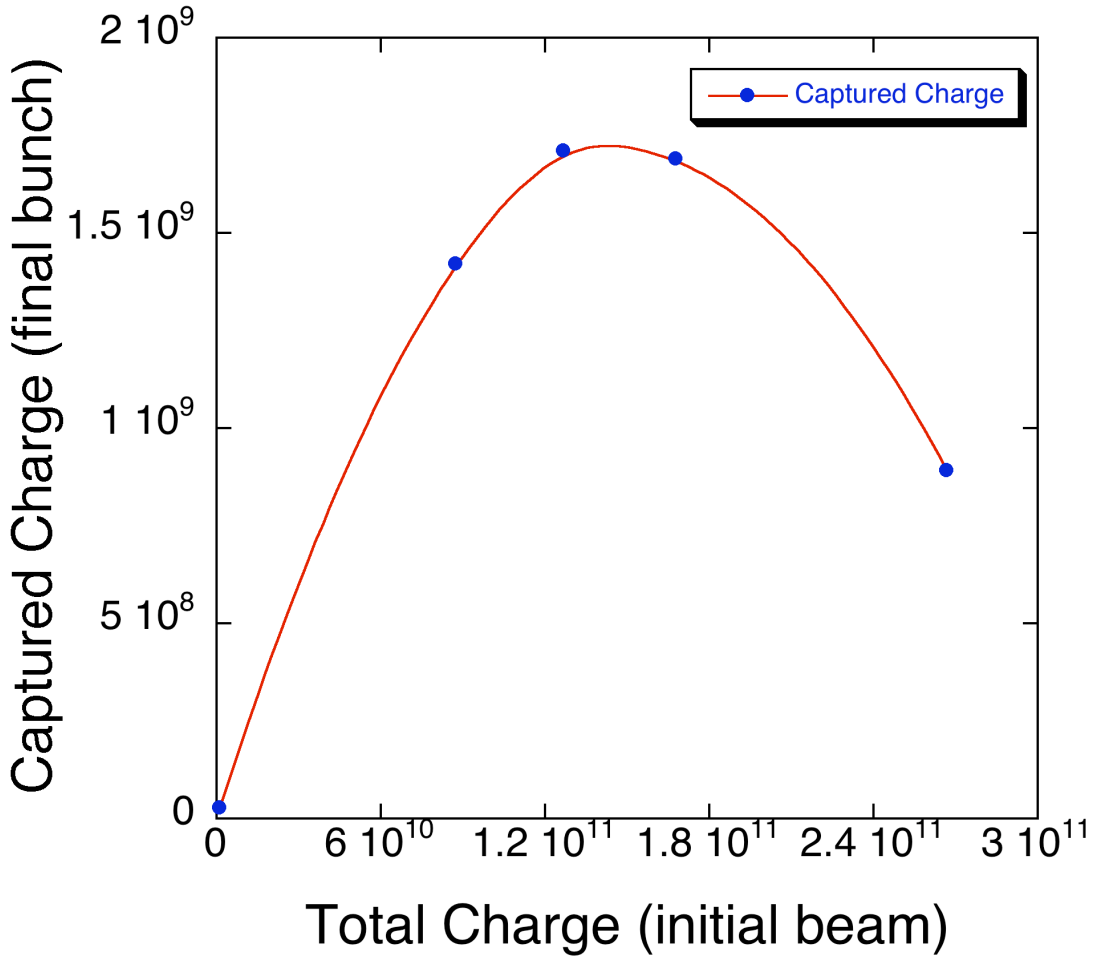

Figure 6. This figure shows the effect of beam loading on the trapping and acceleration process for initially thermal electron bunches. Notice that the charge of trapped electrons is linear in terms of total charge in the bunch up to a total charge of approximately $1x10^{11}$ electrons. At this point the efficiency of trapping electrons by the plasma wake decreases until at $1.2x10^{11}$ electrons the total trapped and accelerated electrons reaches a maximum and further increasing the total charge is disruptive to the trapping process.

Chapter 6: Conclusion

Summary

In this thesis, a model for the coupling between an incident laser pulse, a scattered mode and an evolving plasma channel was presented. Detailed examination of the time dependent solutions to these model equations were discussed and a new kind of parametric instability in the formation of plasma channels has been discovered. The coupling of the incident and scattered pulse with the perturbations in the plasma channel parameters can lead to unstable growth of the scattered channel modes and the associated variation in these evolving plasma channel parameters. Analytic and numerical solutions to these model equations were presented and compared to experimental results. The model we presented demonstrates good agreement with the modulation period and scaling with background gas pressure as well as the onset of the instability at pressures above the pressure for resonant coupling[51]. This instability will likely preclude use of axicon generated plasma channels to produced channels with on-axis electron densities above 2×10^{19} cm^{-3}.

A model for the three-dimensional evolution of a laser pulse propagating in tenuous gas and plasmas was presented. Both model equations for the laser pulse and the numerical schemes used to implement this model on massively parallel computer systems were discussed. Benchmarks and methods used to validate the numerical calculations were presented and demonstrated that this model and implementation agrees with relevant analytic results and other codes in relevant limits.

This new code was used to examine the three-dimensional structure of the ionization process and in particular the instability associated with transverse

scattering during ionization. Simulations of a plane-wave laser pulse with small amplitude transverse scattered modes were presented and shown to agree with the previous results for the relevant frequency up-shift of the scattered light. The transverse scale has the same limits as the previous results for large and small transverse wave number; however the wave number that maximizes unstable growth was shown to be slightly larger. The results of simulations with gaussian laser pulses propagating into gas jets was also discussed and compared to experimental results and demonstrated qualitative agreement. Future work will involve providing a quantitative comparison between the three-dimensional simulations and experiment.

Finally, injection of electron beams with large energy spread into resonant laser-wakefield accelerators was also discussed. A one-dimensional Hamiltonian analysis was presented and used to demonstrate that an electron bunch with an initially large energy spread could be used to produce a reasonable quality beam. Two-dimensional simulations using the code WAKE with test particles were performed and shown to agree with the Hamiltonian analysis. The test-particle simulations demonstrated an increased region in phase where electrons could be effectively captured and trapped in the accelerating phase. This effect was in agreement with previous analysis in plasma channels [40] and enhances the trapping efficiency of these electron beams with initially broad energy spread. Effects of beam loading on the initial trapping and acceleration of electrons in two-dimensions were presented and showed a maximum initial charge above 1.2×10^{11} electrons would lead to deterioration of the final accelerated charge.

A kinetic plasma response for the new simulation code was then discussed. Results were presented of three-dimensional simulations of the trapping and acceleration of broad-energy electron beams. These results included the effect of beam loading.

Future efforts will be focused on further investigation of the design of full-scale accelerators. These investigations will include other electron injections schemes as well as better quantification of the trade-offs in beam quality and acceleration for future accelerator designs.

BIBLIOGRAPHY

1. Tajima, T. and J.M. Dawson, *Laser Electron-Accelerator.* Physical Review Letters, 1979. **43**(4): p. 267-270.
2. Milchberg, H.M., et al., *Development and applications of a plasma waveguide for intense laser pulses.* Physics of Plasmas, 1996. **3**(5): p. 2149-2155.
3. Parra, E., et al., *X-ray and extreme ultraviolet emission induced by variable pulse-width irradiation of Ar and Kr clusters and droplets.* Physical Review E, 2000. **62**(5): p. R5931-R5934.
4. Nuckolls, J., J. Emmett, and L. Wood, *Laser-Induced Thermonuclear Fusion.* Physics Today, 1973. **26**(8): p. 46-53.
5. Nuckolls, J., et al., *Laser Compression of Matter to Super-High Densities - Thermonuclear (Ctr) Applications.* Nature, 1972. **239**(5368).
6. Mourou, G. and D. Umstadter, *Development and Applications of Compact High-Intensity Lasers.* Physics of Fluids B-Plasma Physics, 1992. **4**(7): p. 2315-2325.
7. Mourou, G., *The ultrahigh-peak-power laser: Present and future.* Applied Physics B-Lasers and Optics, 1997. **65**(2): p. 205-211.
8. Sprangle, P., et al., *Laser Wakefield Acceleration and Relativistic Optical Guiding.* Applied Physics Letters, 1988. **53**(22): p. 2146-2148.
9. Joshi, C., et al., *Ultrahigh Gradient Particle-Acceleration by Intense Laser-Driven Plasma-Density Waves.* Nature, 1984. **311**(5986): p. 525-529.

10. Tajima, T. and J.M. Dawson, *Laser Beat Accelerator.* Bulletin of the American Physical Society, 1981. **26**(2): p. 164-164.

11. Esarey, E., et al., *Overview of plasma-based accelerator concepts.* Ieee Transactions on Plasma Science, 1996. **24**(2): p. 252-288.

12. Parra, E., et al., *Pump-probe studies of EUV and X-ray emission dynamics of laser-irradiated noble gas droplets.* Applied Physics a-Materials Science & Processing, 2003. **77**(2): p. 317-323.

13. Esarey, E., et al., *Nonlinear-Analysis of Relativistic Harmonic-Generation by Intense Lasers in Plasmas.* Ieee Transactions on Plasma Science, 1993. **21**(1): p. 95-104.

14. Sprangle, P., J.R. Penano, and B. Hafizi, *Propagation of intense short laser pulses in the atmosphere.* Physical Review E, 2002. **66**(4).

15. Durfee, C.G., J. Lynch, and H.M. Milchberg, *Development of a Plasma Wave-Guide for High-Intensity Laser-Pulses.* Physical Review E, 1995. **51**(3): p. 2368-2389.

16. Durfee, C.G., F. Lynch, and H.M. Milchberg, *Mode Properties of a Plasma Wave-Guide for Intense Laser-Pulses (Vol 19, Pg 1937, 1994).* Optics Letters, 1995. **20**(8): p. 946-946.

17. Zigler, A., et al., *Optical guiding of high-intensity laser pulses in a long plasma channel formed by a slow capillary discharge.* Journal of the Optical Society of America B-Optical Physics, 1996. **13**(1): p. 68-71.

18. Mori, W.B., et al., *Raman Forward Scattering of Short-Pulse High-Intensity Lasers.* Physical Review Letters, 1994. **72**(10): p. 1482-1485.

19. Gordon, D.F., et al., *Asymmetric self-phase modulation and compression of short laser pulses in plasma channels.* Physical Review Letters, 2003. **90**(21).

20. Penano, J.R., et al., *Raman forward scattering and self-modulation of laser pulses in tapered plasma channels.* Physical Review E, 2002. **66**(3).

21. Sprangle, P., E. Esarey, and A. Ting, *Nonlinear-Interaction of Intense Laser-Pulses in Plasmas.* Physical Review A, 1990. **41**(8): p. 4463-4467.

22. Sprangle, P., E. Esarey, and A. Ting, *Nonlinear-Theory of Intense Laser-Plasma Interactions.* Physical Review Letters, 1990. **64**(17): p. 2011-2014.

23. Antonsen, T.M. and P. Mora, *Self-Focusing and Raman-Scattering of Laser-Pulses in Tenuous Plasmas.* Physical Review Letters, 1992. **69**(15): p. 2204-2207.

24. Esarey, E., et al., *Self-focusing and guiding of short laser pulses in ionizing gases and plasmas.* Ieee Journal of Quantum Electronics, 1997. **33**(11): p. 1879-1914.

25. Penano, J.R., et al., *Stimulated Raman scattering of intense laser pulses in air.* Physical Review E, 2003. **68**(5)

26. Shen, Y.R., *The principles of nonlinear optics*. 1984, New York: J. Wiley. xii, 563 p.

27. Wu, J.Z. and T.M. Antonsen, *Laser pulse splitting and trapping in tenuous gases.* Physics of Plasmas, 2003. **10**(6): p. 2254-2266.

28. Bian, Z.G. and T.M. Antonsen, *Ionization instabilities of an electromagnetic wave propagating in a tenuous gas.* Physics of Plasmas, 2001. **8**(7): p. 3183-3194.

29. Galeev, A. and R.N. Sudan, *Basic plasma physics*. Handbook of plasma physics ; v. 1-2. 1983, Amsterdam ; New York, New York, N.Y.: North-Holland Pub. ; Sole distributors for the U.S.A. and Canada, Elsevier Science Pub.

30. Donnelly, T.D., et al., *High-order harmonic generation in atom clusters.* Physical Review Letters, 1996. **76**(14): p. 2472-2475.

31. Ditmire, T., et al., *Interaction of intense laser pulses with atomic clusters.* Physical Review A, 1996. **53**(5): p. 3379-3402.

32. Tisch, J.W.G., et al., *High-harmonic generation from xenon atom clusters.* Multiphoton Processes 1996, 1997(154): p. 177-185.

33. Drake, J.F., et al., *Parametric-Instabilities of Electromagnetic-Waves in Plasmas.* Physics of Fluids, 1974. **17**(4): p. 778-785.

34. Max, C.E., J. Arons, and A.B. Langdon, *Self-Modulation and Self-Focusing of Electromagnetic-Waves in Plasmas.* Physical Review Letters, 1974. **33**(4): p. 209-212.

35. Max, C.E. and A.B. Langdon, *Filamentation of Laser Light in Uniform Plasmas.* Bulletin of the American Physical Society, 1973. **18**(10): p. 1359-1359.

36. Clark, T.R. and H.M. Milchberg, *Time- and space-resolved density evolution of the plasma waveguide.* Physical Review Letters, 1997. **78**(12): p. 2373-2376.

37. Fan, J., E. Parra, and H.M. Milchberg, *Resonant self-trapping and absorption of intense Bessel beams.* Physical Review Letters, 2000. **84**(14): p. 3085-3088.

38. Fan, J., et al., *Resonant self-trapping of high intensity Bessel beams in underdense plasmas.* Physical Review E, 2002. **65**(5).

39. Mora, P. and T.M. Antonsen, *Kinetic modeling of intense, short laser pulses propagating in tenuous plasmas.* Physics of Plasmas, 1997. **4**(1): p. 217-229.

40. Andreev, N.E., L.M. Gorbunov, and A.A. Frolov, *Structure of the wakefield driven by a laser pulse in a narrow plasma channel.* Plasma Physics Reports, 1998. **24**(10): p. 825-831.

41. Clayton, C.E., P. Muggli, and United States. Dept. of Energy., *Advanced accelerator concepts : tenth workshop, Mandalay Beach, California, 22-28 June 2002*. 2002, Melville, N.Y.: American Insititute of Physics. xv, 925 p.

42. Wilks, S., et al., *Beam Loading in Plasma-Waves.* Ieee Transactions on Plasma Science, 1987. **15**(2): p. 210-217.

43. H. M. Milchberg, C. G. Durfee, and T. J. McIlrath, Phys. Rev. Lett. **75**, 2494 (1995); H. M. Milchberg, C. G. Durfee, and J. Lynch, J. Opt. Soc. Am. B **12**, 731 (1995).

44. P. Sprangle, B. Hafizi, J.R. Penano, R.F. Hubbard, A. Ting, A. Zigler, and T.M. Antonsen, Phys. Rev. Lett. **85**, 5110 (2000); H. M. Milchberg, T. R. Clark, C. G. Durfee, T.M. Antonsen, and P. Mora, Phys Plasmas **3**, 2149 (1996).

45. C. G. Durfee and H. M. Milchberg, Phys. Rev. Lett. **71**, 2409 (1993); C. G. Durfee, J. Lynch, and H. M. Milchberg, Phys. Rev. E **51**, 2368 (1995).

46. P. Volfbeyn, E. Esarey, and W. P. Leemans, Phys Plasmas **6**, 2269 (1999).

47. E. W. Gaul, S. P. Le Blanc, A. R. Rundquist, R. Zgadzaj, H. Langhoff, and M. C. Downer, Appl. Phys. Lett. **77**, 4112 (2000)

48. A. Zigler, Y. Ehrlich, C. Cohen, J. Krall, P. Sprangle, J. Opt Soc Am B, **13**, 68 (1996).

49. T. R. Clark and H. M. Milchberg, Phys. Rev. Lett. **81**, 357 (1998); T. R. Clark and H.M. Milchberg, Phys. Rev. E **61**, 1954 (2000).

50. J. Fan, E. Parra, and H. Milchberg, Phys. Rev. Lett. **84**, 3085 (2000); J. Fan, E. Parra, K.Y. Kim, I. Alexeev, H.M. Milchberg, J. Cooley, and T. M. Antonsen, Phys. Rev. E **65**(5), 056408 (2002)

51. S S Bychkov, S V Gorlov, A V Makarov, L Ya Margolin, L N Pyatnitskii, and A D Tal'virskii, Quantum Electronics **29** (3) 243-245 (1999)

52. L. Ya. Margolin, Quantum Electronics, **29** (3) 246-248 (1999)

53. L.N. Pyatnitskii, Plasma Physics Reports **27**, 799 (2001); Y. Ping, I. Geltner, and S. Suckewer, Phys. Plasmas **8** (9), 4174-4179 (2001).

54. R. W. P. McWhirter, in *Plasma Diagnostic Techniques*, edited by R. H. Huddlestone and S. L. Leonard (Academic Press, New York, 1965)

55. D. Pesme, W. Rozmus, V. T. Tikhonchuk, A. Maximov, I. Ourdev, and C. H. Still, Phys Rev. Lett. **84**, 278 (2000).

56. *Basic Plasma Physics I*, editors A.A Galeev and R. N. Sudan, North-Holland Publishing Company, ch. 3.2 A. Bers, page 452

57. M. D. Perry and G. Mourou, Science **264** 917, 1994

58. A. McPherson, T. S. Luk, B. D. Thompson, A. B. Borisov, O. B. Shiryaev, X. Chen, K. Boyer, and C. K. Rhodes, Phys. Rev. Lett. **72**, 1810(1994)

59. G. D. Kubiak, L. J. Bernarez, K. D. Krenz, D. J. O'Connel, R. Gutowski, and A. M. M. Todd, in OSA *Trends in Optics and Photonics* Vol. 4, edited by G. D. Kubiak and D. R. Kania (Optical Society of America, Washington, DC, 1996) page 66-71

60. J. W. G. Tisch, Phys. Rev. A **62**, R41802 (2000); T. Tajima, Y. Kishimoto, and M. C. Downer, Phys. Plasmas **6**, page 3759 (1999)

61. T. R. Clark and H. M. Milchberg, Phys. Rev. E **57**(3) page 3417 , March 1998

62. C. D. Decker, W. B. Mori, K. C. Tzeng, and T. Katsouleas, Phys Plasmas **3**(5) page 2047 May, 1996; Fonseca, R. A., et al, *OSIRIS: A three-dimensional, fully relativistic particle-in-cell code for modeling plasma based accelerators*, Computational Science-Iccs 2002, Pt. Iii, Proceedings, 2002, **2331**: p. 342-351

63. C. K. Birdsall and A. B. Langdon, *Plasma Physics via Computer Simulations* (McGraw-Hill, New York, 1985)

64. C. Huang, V. Decyk, S. Wang, E. Dodd, C. Ren, W. Mori, T. Katsouleas, J. Cooley, and T. M. Antonsen, Jr., Proceedings, 18th Annual Review of Progress in Computational Electromagnetics, page 557, 2002

65. R. D. Richtmeyer and K. W. Morton, in *Interscience Tracts in Pure and Applied Mathematics*, edited by L. Bers, R. Courant, and J. J. Stoker, *Number 4-Difference Methods for Initial-Value Problems* (Wiley, New York, 1967)

66. W. H. Press, S. A. Teukolsky, W. T. Vetterling, and B. P. Flannery, *Numerical Recipes in Fortran 77, the Art of Scientific Computing, Second Edition*, Chapter 16, (Cambridge University Press, 1997)

67. Durfee, C.G. and H.M. Milchberg, *Light Pipe for High-Intensity Laser-Pulses.* Physical Review Letters, 1993. **71**(15): p. 2409-2412.

68. Clark, T.R. and H.M. Milchberg, *Optical mode structure of the plasma waveguide.* Physical Review E, 2000. **61**(2): p. 1954-1965.

69. Krall, J., et al., *Enhanced Acceleration in a Self-Modulated-Laser Wake-Field Accelerator.* Physical Review E, 1993. **48**(3): p. 2157-2161.

70. Umstadter, D., J. K. Kim, and E. Dodd, *Laser injection of ultrashort electron pulses into wakefield plasma waves*, Phys. Rev. Lett, 1996, **76**(12): p.2073-2076

71. Esarey, E., et al., *Laser-induced electron trapping in plasma-based accelerators.* Physics of Plasmas, 1999. **6**(5): p. 2262-2268.

72. Esarey, E. and M. Pilloff, *Trapping and Acceleration in Nonlinear Plasma-Waves.* Physics of Plasmas, 1995. **2**(5): p. 1432-1436.

73. Hubbard, R.F., et al., *Simulation and design of stable channel-guided laser wakefield accelerators.* Physical Review E, 2001. **6303**(3).

74. Andreev, N.E., L.M. Gorbunov, and A.A. Frolov, *Structure of the wakefield driven by a laser pulse in a narrow plasma channel.* Plasma Physics Reports, 1998. **24**(10): p. 825-831.

75. Katsouleas, T., Wilks, S., Chen, P., Dawson, J. M., Su, J. J., *Beam Loading in Plasma Accelerators*, Particle Accelerators **22**, 1987: p. 81-99

76. Gordon, D. F., Mori, W. B., Antonsen, Jr., T. M., *A Ponderomotive Guiding Center Particle-in-Cell Code for Efficient Modeling of Laser-Plasma*

Interactions, IEEE Transactions on Plasma Science, 28(4), August 2000: p. 1224-1232

77. C. Huang, V. K. Deyck, C. Ren, W. B. Mori, J. H. Cooley, T. M. Antonsen Jr., and T. Katsouleas, to be submitted to Journal of Computational Physics.\

78. B. Quesnel and P. Mora, Phys. Rev. E **58**(3) page 3719, September 1998

79. G. Schmidt and W. Horton, Comments Plasma Phys. Controlled Fusion **9**, 85 (1985)

80. Moore, C. I., Ting, A., McNaught, S. J., Qiu, J., Burris, H. R., and Sprangle, P., *A Laser-Accelerator Injector Based on Laser Ionization and Ponderomotive Acceleration of Electrons*, Phys. Rev. Lett. **82**(8), 1999: p. 1688-1691; Moore, C. I., Ting, A., Jones, T., Briscoe, E., Hafizi, B., Hubbard, R. F., Sprangle, P., Measurements of energetic electrons from the high-intensity laser ionization of gases, Physics of Plasmas, 8(5), 2001: p. 2481-2487

81. Eisemann, S. et al, *All optical injector using an intense ultrashort pulse laser and solid wire target*, (submitted to Physics of Plasmas), 2004

82. Alexeev, I. S., *Interation of Intense Laser Pulses with Gaseous Media: Several Exotic Propagation Effects in the Femtosecond Regime*, UMD 2003